



8-2016

Lignin-based Li-Ion Anode Materials Synthesized from Low-Cost Renewable Resources

Nicholas William McNutt

University of Tennessee, Knoxville, nmcnutt@vols.utk.edu

Follow this and additional works at: https://trace.tennessee.edu/utk_graddiss

 Part of the [Nanoscience and Nanotechnology Commons](#), [Other Materials Science and Engineering Commons](#), and the [Sustainability Commons](#)

Recommended Citation

McNutt, Nicholas William, "Lignin-based Li-Ion Anode Materials Synthesized from Low-Cost Renewable Resources. " PhD diss., University of Tennessee, 2016.
https://trace.tennessee.edu/utk_graddiss/3947

This Dissertation is brought to you for free and open access by the Graduate School at TRACE: Tennessee Research and Creative Exchange. It has been accepted for inclusion in Doctoral Dissertations by an authorized administrator of TRACE: Tennessee Research and Creative Exchange. For more information, please contact trace@utk.edu.

To the Graduate Council:

I am submitting herewith a dissertation written by Nicholas William McNutt entitled "Lignin-based Li-Ion Anode Materials Synthesized from Low-Cost Renewable Resources." I have examined the final electronic copy of this dissertation for form and content and recommend that it be accepted in partial fulfillment of the requirements for the degree of Doctor of Philosophy, with a major in Chemical Engineering.

David J. Keffer, Major Professor

We have read this dissertation and recommend its acceptance:

Orlando Rios, Steven Abel, Kenneth Read

Accepted for the Council:

Carolyn R. Hodges

Vice Provost and Dean of the Graduate School

(Original signatures are on file with official student records.)

Lignin-based Li-Ion Anode Materials Synthesized from Low-Cost
Renewable Resources

A Dissertation Presented for the

Doctor of Philosophy

Degree

The University of Tennessee, Knoxville

Nicholas William McNutt

August 2016

DEDICATION

This dissertation is dedicated to my parents, Chris and Susan McNutt, who have always been my heroes, inspiration, and role models; to Emily McGhee, for being the best sister a brother could hope for; and to my best friend Jennifer Wilson, for her continual love, encouragement, and exceptional kindness.

ACKNOWLEDGMENTS

I wish to thank my advisor, Dr. David Keffer, for his support, kindness, and guidance. His mentorship has been invaluable to my work and to my development as a researcher. I am fortunate to have had such a caring advisor, and am grateful for all of the time and consideration he has devoted to helping me succeed.

I would like to thank Dr. Orlando Rios for the wonderful collaboration we have had working on this project, and for his insight, advice, and contributions. This work would not have been possible without him.

A deep expression of gratitude is owed to Dr. Steve Abel and Dr. Kenneth Read for serving on my dissertation committee, and for their thoughtful analysis of my work and insightful suggestions. I also extend this gratitude to Dr. Vasileios Maroulas for his valuable suggestions and collaboration.

I would like to thank Marshall McDonnell for his research contributions and for his friendship, and Chris Ostrouchov for his friendship as well. Special thanks is given to Dr. Mikhail Feygenson and Dr. Joerg C. Neufeind for their contributions and for their guidance with the NOMAD beamline at the Spallation Neutron Source at Oak Ridge National Laboratory.

I am grateful to the Department of Chemical Engineering for their instruction and support, and would particularly like to thank the organizations that sponsored my research: the Oak Ridge Associated Universities High Performance Computing Program, the Sustainable Energy Education and Research Center of the University of Tennessee, the National Science Foundation, the Department of Energy, and the STAIR program at the University of Tennessee.

Furthermore, I am greatly appreciative of the assistance I received from Dr. Adri van Duin and Dr. Muralikrishna Raju for providing and assisting with the ReaxFF potential for which the major findings of this research were made possible.

Lastly, I would like to thank Rita Gray for all of her support and kindness over the past four years.

ABSTRACT

In today's world, the demand for novel methods of energy storage is increasing rapidly, particularly with the rise of portable electronic devices, electric vehicles, and the personal consumption and storage of solar energy. While other technologies have arguably improved at a rate that is exponential in accordance with Moore's law, battery technology has lagged behind largely due to the difficulty in devising new electric storage systems that are simultaneously high performing, inexpensive, and safe.

In order to tackle these challenges, novel Li-ion battery anodes have been developed at Oak Ridge National Laboratory that are made from lignin, a low-cost, renewable resource that is obtained from an abundant supply of biomass. The anodes that result from the lignin manufacturing process exhibit performance comparable to that of conventional graphitic anodes for a fraction of the cost. However, these materials are unusual in that they consist solely of a mixture of amorphous and crystalline carbon, and this complex, hierarchical material is not well understood. This thesis reveals the mechanism behind the structural composition and the performance of these carbon composite anodes.

The anodes are investigated using two distinct approaches: 1) a computational approach, whereby atomistic models of the composite systems are created and simulated using reactive molecular dynamics, and 2) an experimental approach, whereby the small scale structure of the material is elucidated using neutron diffraction.

The computational approach reveals deep insight into the nature of Li-ion localization, and a novel technique (that is highly generalizable) has been developed to understand the local atomic environment that surrounds Li-ions at various binding energies. The experimental approach is used in conjunction with the simulation results to understand the structure of the carbon composites, and how unique structural properties vary as a function of the parameters that are controlled in the manufacturing process. This insight leads to the revelation that a large interfacial surface area between amorphous and crystalline carbon domains is paramount for high-capacity storage of Li-ions.

TABLE OF CONTENTS

1	Introduction	1
1.1	Background	2
1.2	Motivation and Objectives	4
1.3	Per Chapter Summary	5
1.3.1	Entropy-driven Structure and Dynamics in Carbon Nanocrystallites	5
1.3.2	Structural Analysis of Lignin-derived Carbon Composite Anodes	5
1.3.3	Interfacial Li-ion Localization in Hierarchical Carbon Anodes	5
1.3.4	Li-ion Localization and Energetics as a Function of Anode Structure	6
2	Entropy-driven Structure and Dynamics in Carbon Nanocrystallites.....	7
2.1	Introduction	8
2.2	Simulation Methods	10
2.3	Results and Discussion	12
2.3.1	Thermodynamic Properties	12
2.3.2	Structural Properties	17
2.3.3	Dynamical Properties	24
2.4	Conclusions	27
2.5	Acknowledgments.....	28
3	Structural Analysis of Lignin-derived Carbon Composite Anodes.....	29
3.1	Introduction	30
3.2	Methods for Simulation and Experiment	32
3.2.1	Synthesis.....	32
3.2.2	Structural Characterization	32
3.2.3	Neutron Scattering	32
3.2.4	Simulation.....	33
3.3	Results and Discussion	34
3.3.1	Direct Measurement of d-spacing.....	36
3.3.2	Pair Distribution Functions	39
3.4	Conclusions	58

3.5	Acknowledgments	61
4	Interfacial Li-ion Localization in Hierarchical Carbon Anodes	62
4.1	Introduction	63
4.2	Methods.....	64
4.3	Results	66
4.4	Conclusions	76
4.5	Acknowledgments.....	76
5	Li-ion Localization and Energetics as a Function of Anode Structure.....	77
5.1	Introduction	78
5.2	Methods.....	79
5.2.1	Synthesis.....	79
5.2.2	Structural Characterization	80
5.2.3	Neutron Scattering	80
5.2.4	Simulation.....	80
5.3	Results	83
5.3.1	Pair Distribution Functions	83
5.3.2	Energetics and Charge	100
5.4	Conclusions	108
5.5	Acknowledgments.....	108
6	Conclusions	109
6.1	Per Chapter Conclusions	110
6.1.1	Entropy-driven Structure and Dynamics in Carbon Nanocrystallites	110
6.1.2	Structural Analysis of Lignin-derived Carbon Composite Anodes	110
6.1.3	Interfacial Li-ion Localization in Hierarchical Carbon Anodes	111
6.1.4	Li-ion Localization and Energetics as a Function of Anode Structure.....	111
6.2	Impact and Significance	112
6.3	Future Work.....	112
	References	113
	Vita	120

LIST OF TABLES

TABLE 2.1. COMPARISON OF MEASURES OF INTERPLANAR SPACING (BREATHING AND COM DISTANCES) FOR THE THREE CARBON NANOCRYSTALLITES AROUND 291 K (R = 5 Å: 293 K; R = 7 Å: 280 K; R = 17 Å: 278 K, EXPERIMENT DATA IS TAKEN AT 291 K [15]).....	23
TABLE 3.1. THE UPPER LIMIT OF THE VOLUME FRACTION VARIED, SINCE IT IS NOT POSSIBLE TO SIMULTANEOUSLY OBTAIN A SPECIFIED LOW COMPOSITE DENSITY AND HIGH CRYSTALLINE VOLUME FRACTION. AN ASTERISK DENOTES EXPERIMENTALLY SYNTHESIZED MATERIALS.	35
TABLE 3.2. EFFECT OF CHANGING ONE PROPERTY OF A COMPOSITE MATERIAL ON D-SPACING (TWO TYPES: BREATHING DISTANCE AND CENTER-OF-MASS DISTANCE).	38
TABLE 3.3. DESCRIPTION OF COMPONENT FUNCTIONS FOR PAIR DISTRIBUTION FUNCTIONS.....	41
TABLE 3.4. LISTING OF FIRST PEAK POSITIONS IN EXPERIMENTAL AND SIMULATED PDFs.	54
TABLE 3.5. SUMMARY OF EFFECTS OF DIFFERENT PROPERTIES ON THE PDFs.	60
TABLE 5.1. COLLECTIONS OF SYSTEMS WITH ONE PROPERTY CHANGED.....	82
TABLE 5.2. DESCRIPTION OF COMPONENT FUNCTIONS FOR PAIR DISTRIBUTION FUNCTIONS.....	87

LIST OF FIGURES

FIGURE 1.1. (A) CHARGE STORAGE CAPACITY OF LIGNIN CARBON FIBERS CARBONIZED AT 1000 °C (RED), 1500 °C (GREEN), AND 2000 °C (BLUE) AS A FUNCTION OF CURRENT IN SLURRY-COATED ELECTRODES. (B) CHARGE CAPACITIES AS A FUNCTION OF CYCLING AND CARBONIZATION TEMPERATURES IN SLURRY-COATED ELECTRODE. FIGURES AND CAPTIONS FROM [3].....	2
FIGURE 1.2. (A) MOLECULAR STRUCTURE OF POLYACRYLONITRILE (PAN) EXHIBITS ANISOTROPY IN THE ARRANGEMENT OF CARBON SHEETS. FIGURE FROM [7]. (B) MOLECULAR STRUCTURE OF LIGNIN-BASED CARBON FIBER (LCF). THE LCF EXHIBITS NEAR PERFECT TURBOSTRATIC DISORDER. FIGURE FROM [8].....	3
FIGURE 1.3. (A) SCANNING ELECTRON IMAGES OF LCFs GROUND FOR PARTICLE SIZE REDUCTION AND COATED ONTO COPPER CURRENT COLLECTORS BY SLURRY COATING. (B) HIGH RESOLUTION TRANSITION ELECTRON MICROSCOPY IMAGES AT A PYROLYSIS TEMPERATURE OF 2000 °C. THE INSET IMAGES ARE SELECTIVE AREA PATTERNS ON THE SAME MATERIALS. FIGURES AND CAPTIONS FROM [3].....	4
FIGURE 2.1. MOLECULAR REPRESENTATIONS OF THREE CARBON NANOCRYSTALLITES: (A): $R = 5 \text{ \AA}$, AT 0 K; (B): $R = 7 \text{ \AA}$, AT 0 K; (C): $R = 17 \text{ \AA}$, AT 0 K; (D): $R = 5 \text{ \AA}$, AT 300 K; (E): $R = 7 \text{ \AA}$, AT 300 K AND (F): $R = 17 \text{ \AA}$, AT 300 K. THE SCALE IS DIFFERENT FOR EACH CRYSTALLITE.	11
FIGURE 2.2. INDIVIDUAL POTENTIAL ENERGY AS A FUNCTION OF TEMPERATURE FOR THE THREE CARBON NANOCRYSTALLITES. (ENERGY IS ON A PER ATOM BASIS.)	14
FIGURE 2.3. HEAT CAPACITY (A) AND ENTROPY CHANGE (B) AS A FUNCTION OF TEMPERATURE FOR THE THREE CARBON NANOCRYSTALLITES.	16
FIGURE 2.4. SCHEMES OF DEFINITIONS OF DIFFERENT GEOMETRICAL CHARACTERIZATIONS (COM 1: CENTER OF MASS POSITIONS OF LAYER 1; COM 2: CENTER OF MASS POSITIONS OF LAYER 2; NORM 1: NORM VECTOR OF LAYER 1; NORM 2: NORM VECTOR OF LAYER 2).....	18
FIGURE 2.5. THE STANDARD DEVIATION OF THE CARBON DISTANCE FROM THE PLANE AS A FUNCTION OF TEMPERATURE.	19
FIGURE 2.6. STRUCTURES AS A FUNCTION OF TEMPERATURE FOR THE THREE CARBON NANOCRYSTALLITES (D-SLIDING: HORIZONTAL SEPARATION OF TWO ADJACENT LAYERS; D-BREATHING: VERTICAL SEPARATION OF TWO ADJACENT LAYERS; ROCKING-ANGLE: ANGLE OF TWO NORMAL VECTORS OF TWO ADJACENT LAYERS; D-COM: CENTER OF MASS SEPARATION OF TWO ADJACENT LAYERS).	21
FIGURE 2.7. STRUCTURES AS A FUNCTION OF TIME FOR THE NANOCRYSTALLITE WITH $R = 5 \text{ \AA}$ AT 266 K. (D-SLIDING: HORIZONTAL SEPARATION OF TWO ADJACENT LAYERS; D-BREATHING: VERTICAL SEPARATION OF TWO ADJACENT LAYERS; ROCKING-ANGLE: ANGLE OF TWO NORMAL VECTORS OF TWO ADJACENT LAYERS; D-COM: CENTER OF MASS SEPARATION OF TWO ADJACENT LAYERS).	25
FIGURE 2.8. CALCULATED FOURIER TRANSFORMS OF (A): HORIZONTAL SEPARATION (D-SLIDING), (B): VERTICAL SEPARATION (D-BREATHING), (C): ANGLE ROCKING AND (D) CENTER OF MASS SEPARATION (D-COM) FOR THE TOP TWO LAYERS OF THE	

NANOCRYSTALLITE WITH $R = 5 \text{ \AA}$ AT DIFFERENT TEMPERATURES (FROM BOTTOM TO TOP: 67 K, 141 K, 216 K, 293 K, 366 K).....	26
FIGURE 3.1. MOLECULAR REPRESENTATION OF THREE COMPOSITE SYSTEMS BEFORE EQUILIBRATION (TOP ROW) AND AFTER (BOTTOM ROW): (A) & (D) $R = 5 \text{ \AA}$, $\rho = 1.94 \text{ g/cm}^3$, $\Phi_c = 0.9$; (B) & (E) $R = 7 \text{ \AA}$, $\rho = 1.51 \text{ g/cm}^3$, $\Phi_c = 0.5$; (C) & (F) $R = 17 \text{ \AA}$, $\rho = 1.38 \text{ g/cm}^3$, $\Phi_c = 0.1$	37
FIGURE 3.2. SIMULATED PDFs ($R = 7 \text{ \AA}$, $\rho = 1.51 \text{ g/cm}^3$, $\Phi_c = 0.5$) IN THREE FORMATS: (A) $G(R)$ TO REVEAL SHORT-RANGE FEATURES, (B) DECOMPOSITION OF $G(R)$ INTO COMPONENT FUNCTIONS, (C) $G(R)$ TO REVEAL LONG-RANGE FEATURES.....	42
FIGURE 3.3. SIMULATED PDFs ($R = 17 \text{ \AA}$, $\rho = 1.38 \text{ g/cm}^3$, $\Phi_c = 0.5$) SHOWING THE D-SPACING REGION FOR THE INITIAL COMPOSITE SYSTEM (A) AND THE EQUILIBRATED COMPOSITE SYSTEM (B).	44
FIGURE 3.4. SIMULATED PDFs WITH DECOMPOSITION FOR TWO MATERIALS WITH COMMON DENSITY AND CRYSTALLINE VOLUME FRACTION. ($\rho = 1.38 \text{ g/cm}^3$, $\Phi_c = 0.5$). (A) SMALLER CRYSTALLITES ($R = 7 \text{ \AA}$) AND (B) LARGER CRYSTALLITES ($R = 17 \text{ \AA}$). .	45
FIGURE 3.5. SIMULATED DDCFs FOR TWO MATERIALS WITH COMMON DENSITY AND CRYSTALLINE VOLUME FRACTION ($\rho = 1.38 \text{ g/cm}^3$, $\Phi_c = 0.5$) AND VARYING CRYSTALLITE SIZE.	47
FIGURE 3.6. SIMULATED DDCFs FOR MATERIALS WITH COMMON DENSITY ($\rho = 1.38 \text{ g/cm}^3$) AT TWO CRYSTALLITE RADII AND THREE CRYSTALLINE VOLUME FRACTIONS: (A) LOW $\Phi_c = 0.1$, (B) MEDIUM $\Phi_c = 0.5$, (C) HIGH $\Phi_c = 0.7/0.6$	48
FIGURE 3.7. SIMULATED DDCFs WITH DECOMPOSITION FOR TWO MATERIALS WITH COMMON DENSITY AND HIGH CRYSTALLINE VOLUME FRACTION ($\rho = 1.38 \text{ g/cm}^3$, $\Phi_c = 0.7/0.6$). (A) SMALLER CRYSTALLITES ($R = 7 \text{ \AA}$) AND (B) LARGER CRYSTALLITES ($R = 17 \text{ \AA}$).	50
FIGURE 3.8. SIMULATED SHORT-RANGE PDFs FOR MATERIALS WITH COMMON CRYSTALLITE SIZE AND CRYSTALLINE VOLUME FRACTION ($R = 7 \text{ \AA}$, $\Phi_c = 0.1$) AND VARYING DENSITY.	51
FIGURE 3.9. SIMULATED LONG-RANGE DDCFs FOR MATERIALS WITH COMMON CRYSTALLITE SIZE AND CRYSTALLINE VOLUME FRACTION ($R = 7 \text{ \AA}$, $\Phi_c = 0.1$) AND VARYING DENSITY.	51
FIGURE 3.10. (A) PLOTS OF SIMULATED COMPOSITE SYSTEMS AND (B) THE CORRESPONDING EXPERIMENTAL SYSTEMS SCALED SUCH THAT THE FIRST PEAK INTEGRAL EQUALS THAT OF SIMULATION.	53
FIGURE 3.11. PLOTS OF $G(R)$ FOR (A) SIMULATED COMPOSITE SYSTEMS, AND (B) THE CORRESPONDING EXPERIMENTAL SYSTEMS ($Q_{\text{MAX}} = 30 \text{ \AA}^{-1}$) SCALED SUCH THAT THE FIRST PEAK INTEGRAL EQUALS THAT OF SIMULATION.	56
FIGURE 3.12. SIMULATED SHORT-RANGE PDFs FOR MATERIALS WITH COMMON CRYSTALLITE SIZE AND COMPOSITE DENSITY ($R = 17 \text{ \AA}$, $\rho = 1.38 \text{ g/cm}^3$) AND VARYING CRYSTALLINE VOLUME FRACTION.	57
FIGURE 3.13. THE LONG-RANGE EFFECT OF CRYSTALLINE VOLUME FRACTION ON THE DDCF OF A REPRESENTATIVE MATERIAL ($\rho = 1.38 \text{ g/cm}^3$, $R = 17 \text{ \AA}$).	59
FIGURE 4.1. THE HIERARCHICAL CARBON ANODE MODEL AFTER EQUILIBRATION. ATOMS ARE COLORED BY TYPE: AMORPHOUS CARBON IS BLUE, CRYSTALLINE CARBON IS GREEN, HYDROGEN ATOMS ARE WHITE, AND LITHIUM IONS ARE YELLOW. THIS SIMULATION CORRESPONDS TO A LOADING OF 147.8 mAh g^{-1} AND AN INITIAL CONDITION IN WHICH ALL ATOMS WERE INITIALLY INTERCALATED WITHIN THE CRYSTALLINE DOMAIN.	67

FIGURE 4.2. A SMALL COMPOSITE SYSTEM WITH LI-IONS INTERCALATED IN THE CRYSTALLINE DOMAIN (A) PRE-EQUILIBRATION AND (B) POST-EQUILIBRATION. FOR CLARITY, THE AMORPHOUS CARBON MATRIX AND HYDROGEN ATOMS SURROUNDING THE CARBON NANOCRYSTALLITE ARE RENDERED INVISIBLE.	68
FIGURE 4.3. PROBABILITY DENSITY FUNCTIONS OF THE DISTRIBUTION OF LI-ION BINDING ENERGIES IN THE EQUILIBRATED LARGE COMPOSITE ANODE SYSTEM FOR (A) HIGH AMORPHOUS LOADING, (B) HIGH CRYSTALLINE LOADING, (C) LOW AMORPHOUS LOADING, AND (D) LOW CRYSTALLINE LOADING.	69
FIGURE 4.4. PDFs FOR (A) LI-LI, (B) LI-H, AND (C) LI-C PAIRS OF ATOMS.	71
FIGURE 4.5. 3D DENSITY DISTRIBUTIONS OF LI (GREEN) AND H (WHITE) FOR (A) STRONG LI-ION BINDING ENERGIES, (B) MODERATE LI-ION BINDING ENERGIES, AND (C) WEAK LI-ION BINDING ENERGIES. EACH DISTRIBUTION IS CENTERED AROUND A LI ION, WHICH IS NOT SHOWN.	72
FIGURE 4.6. LI-ION PARTIAL CHARGE AS A FUNCTION OF ION ENERGY.	74
FIGURE 4.7. COMPARISON OF THE CARBON (C-C) PDFs FOR (A) THE UNCHARGED MATERIALS AND (B) THE LITHIATED MATERIALS.	75
FIGURE 5.1. THE MODEL COMPOSITE SYSTEMS WITH PROPERTIES SPECIFIED. CRYSTALLINE CARBON IS GRAY; AMORPHOUS CARBON IS BLUE; HYDROGEN IS WHITE. THE MODEL SYSTEMS THAT CORRESPOND TO THE EXPERIMENTAL SYSTEMS ARE LABELED ON THE BASIS OF PYROLYSIS TEMPERATURE: (A) 1000 °C, (B) 1500 °C, AND (C) 2000 °C.	81
FIGURE 5.2. SNAPSHOTS OF THE THREE MODEL SYSTEMS THAT CORRESPOND TO THE THREE EXPERIMENTAL SYSTEMS AFTER LITHIATION AND EQUILIBRATION: (A) $R = 5 \text{ \AA}$, $P = 1.94 \text{ g/cm}^3$, $\Phi_c = 0.9$, AND $Q = 126.1 \text{ MAH G}^{-1}$; (B) $R = 7 \text{ \AA}$, $P = 1.51 \text{ g/cm}^3$, $\Phi_c = 0.5$, AND $Q = 147.8 \text{ MAH G}^{-1}$; (C) $R = 17 \text{ \AA}$, $P = 1.38 \text{ g/cm}^3$, $\Phi_c = 0.1$, AND $Q = 349.8 \text{ MAH G}^{-1}$. AMORPHOUS CARBON IS BLUE, CRYSTALLINE CARBON IS GRAY, AND LI-IONS ARE YELLOW.	84
FIGURE 5.3. EXPERIMENTALLY OBTAINED PDFs OF (A) THE UNCHARGED SYSTEMS AND (B) THE CHARGED SYSTEMS FOR THREE TEMPERATURES EACH.	85
FIGURE 5.4. PDFs OF THE SIMULATED MODELS CORRESPONDING TO THE EXPERIMENTAL SYSTEMS IN (A) THE UNCHARGED STATE AND (B) THE CHARGED STATE.	86
FIGURE 5.5. CARBON PDF DECOMPOSITIONS OF A REPRESENTATIVE UNCHARGED SYSTEM (A) AND THE CHARGED SYSTEM (B). THE COMPOSITE PARAMETERS ARE $R = 7 \text{ \AA}$, $P = 1.51 \text{ g/cm}^3$, $\Phi_c = 0.5$, AND $Q = 147.8 \text{ MAH G}^{-1}$	88
FIGURE 5.6. A CLOSE UP VIEW OF THE INTER-CARBON PDF COMPONENT FUNCTIONS IN FIGURE 5.5 OF (A) THE UNCHARGED COMPOSITE AND (B) THE CHARGED COMPOSITE.	89
FIGURE 5.7. FOR THE MODEL OF THE 1000 °C EXPERIMENTAL SYSTEM, THE 3D DENSITY DISTRIBUTIONS OF LI (GREEN) AND H (WHITE) FOR (A) STRONG LI-ION BINDING ENERGIES, (B) MODERATE LI-ION BINDING ENERGIES, AND (C) WEAK LI-ION BINDING ENERGIES. EACH DISTRIBUTION IS CENTERED AROUND A LI ION, WHICH IS NOT SHOWN.	91
FIGURE 5.8. FOR THE MODEL OF THE 1500 °C EXPERIMENTAL SYSTEM, THE 3D DENSITY DISTRIBUTIONS OF LI (GREEN) AND H (WHITE) FOR (A) STRONG LI-ION BINDING ENERGIES, (B) MODERATE LI-ION BINDING ENERGIES, AND (C) WEAK LI-ION BINDING ENERGIES. EACH DISTRIBUTION IS CENTERED AROUND A LI ION, WHICH IS NOT SHOWN.	91

FIGURE 5.9. FOR THE MODEL OF THE 2000 °C EXPERIMENTAL SYSTEM, THE 3D DENSITY DISTRIBUTIONS OF LI (GREEN) AND H (WHITE) FOR (A) STRONG LI-ION BINDING ENERGIES, (B) MODERATE LI-ION BINDING ENERGIES, AND (C) WEAK LI-ION BINDING ENERGIES. EACH DISTRIBUTION IS CENTERED AROUND A LI ION, WHICH IS NOT SHOWN.	91
FIGURE 5.10. FOR THE MODEL OF THE 1000 °C EXPERIMENTAL SYSTEM, THE 3D DENSITY DISTRIBUTION OF LI (GREEN), H (WHITE), CRYSTALLINE C (BLUE), AND AMORPHOUS C (YELLOW) FOR (A) STRONG LI-ION BINDING ENERGIES, (B) MODERATE LI-ION BINDING ENERGIES, AND (C) WEAK LI-ION BINDING ENERGIES.	92
FIGURE 5.11. FOR THE MODEL OF THE 1500 °C EXPERIMENTAL SYSTEM, THE 3D DENSITY DISTRIBUTION OF LI (GREEN), H (WHITE), CRYSTALLINE C (BLUE), AND AMORPHOUS C (YELLOW) FOR (A) STRONG LI-ION BINDING ENERGIES, (B) MODERATE LI-ION BINDING ENERGIES, AND (C) WEAK LI-ION BINDING ENERGIES.	92
FIGURE 5.12. FOR THE MODEL OF THE 2000 °C EXPERIMENTAL SYSTEM, THE 3D DENSITY DISTRIBUTION OF LI (GREEN), H (WHITE), CRYSTALLINE C (BLUE), AND AMORPHOUS C (YELLOW) FOR (A) STRONG LI-ION BINDING ENERGIES, (B) MODERATE LI-ION BINDING ENERGIES, AND (C) WEAK LI-ION BINDING ENERGIES.	92
FIGURE 5.13. PDFs FOR (A) LI-C, (B) LI-A, (C) LI-H, AND (D) LI-LI. DENSITY VARIES ACROSS THE THREE SYSTEMS, WHILE CRYSTALLITE RADIUS ($R = 7 \text{ \AA}$), CRYSTALLINE VOLUME FRACTION ($\Phi_c = 0.5$), AND CHARGE ($Q = 147.8 \text{ MAH G}^{-1}$) ARE HELD CONSTANT. .	93
FIGURE 5.14. 3D DENSITY DISTRIBUTIONS FOR COMPOSITE DENSITIES OF (A) $P = 1.38 \text{ G/CM}^3$, (B) $P = 1.51 \text{ G/CM}^3$, AND (C) $P = 1.94 \text{ G/CM}^3$. CRYSTALLITE RADIUS ($R = 7 \text{ \AA}$), CRYSTALLINE VOLUME FRACTION ($\Phi_c = 0.5$), AND CHARGE ($Q = 147.8 \text{ MAH G}^{-1}$) ARE HELD CONSTANT. LI IONS ARE GREEN AND H ATOMS ARE WHITE. EACH DISTRIBUTION IS CENTERED AROUND A LI ION, WHICH IS NOT SHOWN.	95
FIGURE 5.15. 3D DENSITY DISTRIBUTIONS FOR COMPOSITE DENSITIES OF (A) $P = 1.38 \text{ G/CM}^3$, (B) $P = 1.51 \text{ G/CM}^3$, AND (C) $P = 1.94 \text{ G/CM}^3$. CRYSTALLITE RADIUS ($R = 7 \text{ \AA}$), CRYSTALLINE VOLUME FRACTION ($\Phi_c = 0.5$), AND CHARGE ($Q = 147.8 \text{ MAH G}^{-1}$) ARE HELD CONSTANT. LI IONS ARE GREEN, H ATOMS ARE WHITE, C ATOMS ARE BLUE, AND A ATOMS ARE YELLOW. EACH DISTRIBUTION IS CENTERED AROUND A LI ION, WHICH IS NOT SHOWN.	95
FIGURE 5.16. PDFs FOR (A) LI-C, (B) LI-A, (C) LI-H, AND (D) LI-LI. CRYSTALLITE RADIUS VARIES ACROSS THE TWO SYSTEMS, WHILE DENSITY ($P = 1.94 \text{ G/CM}^3$), CRYSTALLINE VOLUME FRACTION ($\Phi_c = 0.5$), AND CHARGE ($Q = 147.8 \text{ MAH G}^{-1}$) ARE HELD CONSTANT.....	96
FIGURE 5.17. PDFs FOR (A) LI-C, (B) LI-A, (C) LI-H, AND (D) LI-LI. CRYSTALLITE RADIUS VARIES ACROSS THE TWO SYSTEMS, WHILE DENSITY ($P = 1.38 \text{ G/CM}^3$), CRYSTALLINE VOLUME FRACTION ($\Phi_c = 0.5$), AND CHARGE ($Q = 147.8 \text{ MAH G}^{-1}$) ARE HELD CONSTANT.....	97
FIGURE 5.18. 3D DENSITY DISTRIBUTIONS FOR CRYSTALLITE RADII OF (A) $R = 7 \text{ \AA}$ AND (B) $R = 17 \text{ \AA}$. COMPOSITE DENSITY ($P = 1.38 \text{ G/CM}^3$), CRYSTALLINE VOLUME FRACTION ($\Phi_c = 0.5$), AND CHARGE ($Q = 147.8 \text{ MAH G}^{-1}$) ARE HELD CONSTANT. LI IONS ARE GREEN AND H ATOMS ARE WHITE. EACH DISTRIBUTION IS CENTERED AROUND A LI ION, WHICH IS NOT SHOWN.....	98
FIGURE 5.19. 3D DENSITY DISTRIBUTIONS FOR CRYSTALLITE RADII OF (A) $R = 7 \text{ \AA}$ AND (B) $R = 17 \text{ \AA}$. COMPOSITE DENSITY ($P = 1.38 \text{ G/CM}^3$), CRYSTALLINE VOLUME FRACTION ($\Phi_c = 0.5$), AND CHARGE ($Q = 147.8 \text{ MAH G}^{-1}$) ARE HELD CONSTANT. LI IONS ARE GREEN, H ATOMS ARE WHITE, C ATOMS ARE BLUE, AND A ATOMS ARE YELLOW. EACH DISTRIBUTION IS CENTERED AROUND A LI ION, WHICH IS NOT SHOWN.	98

FIGURE 5.20. PDFs FOR (A) LI-C, (B) LI-A, (C) LI-H, AND (D) LI-LI. CRYSTALLINE VOLUME FRACTION VARIES ACROSS THE THREE SYSTEMS, WHILE DENSITY ($P = 1.51 \text{ G/CM}^3$), CRYSTALLITE RADIUS ($R = 7 \text{ \AA}$), AND CHARGE ($Q = 147.8 \text{ MAH G}^{-1}$) ARE HELD CONSTANT.

.....99

FIGURE 5.21. 3D DENSITY DISTRIBUTIONS FOR CRYSTALLINE VOLUME FRACTIONS OF (A) $\Phi_c = 0.1$, (B) $\Phi_c = 0.5$, AND (C) $\Phi_c = 0.75$. CRYSTALLITE RADIUS ($R = 7 \text{ \AA}$), COMPOSITE DENSITY ($P = 1.51 \text{ G/CM}^3$), AND CHARGE ($Q = 147.8 \text{ MAH G}^{-1}$) ARE HELD CONSTANT. LI IONS ARE GREEN AND H ATOMS ARE WHITE. EACH DISTRIBUTION IS CENTERED AROUND A LI ION, WHICH IS NOT SHOWN.101

FIGURE 5.22. 3D DENSITY DISTRIBUTIONS FOR CRYSTALLINE VOLUME FRACTIONS OF (A) $\Phi_c = 0.1$, (B) $\Phi_c = 0.5$, AND (C) $\Phi_c = 0.75$. CRYSTALLITE RADIUS ($R = 7 \text{ \AA}$), COMPOSITE DENSITY ($P = 1.51 \text{ G/CM}^3$), AND CHARGE ($Q = 147.8 \text{ MAH G}^{-1}$) ARE HELD CONSTANT. LI IONS ARE GREEN, H ATOMS ARE WHITE, C ATOMS ARE BLUE, AND A ATOMS ARE YELLOW. EACH DISTRIBUTION IS CENTERED AROUND A LI ION, WHICH IS NOT SHOWN.101

FIGURE 5.23. PDFs FOR (A) LI-C, (B) LI-A, (C) LI-H, AND (D) LI-LI. SPECIFIC CHARGE CAPACITY VARIES ACROSS THE THREE SYSTEMS, WHILE DENSITY ($P = 1.51 \text{ G/CM}^3$), CRYSTALLINE VOLUME FRACTION ($\Phi_c = 0.5$), AND CRYSTALLITE RADIUS ($R = 7 \text{ \AA}$) ARE HELD CONSTANT.....102

FIGURE 5.24. 3D DENSITY DISTRIBUTIONS FOR SPECIFIC CHARGE CAPACITIES OF (A) $Q = 126.1 \text{ MAH/G}$, (B) $Q = 147.8 \text{ MAH/G}$, AND (C) $Q = 349.8 \text{ MAH/G}$. CRYSTALLITE RADIUS ($R = 7 \text{ \AA}$), COMPOSITE DENSITY ($P = 1.51 \text{ G/CM}^3$), AND CRYSTALLINE VOLUME FRACTION ($\Phi_c = 0.5$) ARE HELD CONSTANT. LI IONS ARE GREEN AND H ATOMS ARE WHITE. EACH DISTRIBUTION IS CENTERED AROUND A LI ION, WHICH IS NOT SHOWN.103

FIGURE 5.25. 3D DENSITY DISTRIBUTIONS FOR SPECIFIC CHARGE CAPACITIES OF (A) $Q = 126.1 \text{ MAH/G}$, (B) $Q = 147.8 \text{ MAH/G}$, AND (C) $Q = 349.8 \text{ MAH/G}$. CRYSTALLITE RADIUS ($R = 7 \text{ \AA}$), COMPOSITE DENSITY ($P = 1.51 \text{ G/CM}^3$), AND CRYSTALLINE VOLUME FRACTION ($\Phi_c = 0.5$) ARE HELD CONSTANT. LI IONS ARE GREEN, H ATOMS ARE WHITE, C ATOMS ARE BLUE, AND A ATOMS ARE YELLOW. EACH DISTRIBUTION IS CENTERED AROUND A LI ION, WHICH IS NOT SHOWN.103

FIGURE 5.26. THE ENERGY DISTRIBUTION (A) AND CHARGE DISTRIBUTION (B) OF THREE SYSTEMS. DENSITY VARIES ACROSS THE SYSTEMS, WHILE CRYSTALLITE RADIUS ($R = 7 \text{ \AA}$), CRYSTALLINE VOLUME FRACTION ($\Phi_c = 0.5$), AND CHARGE ($Q = 147.8 \text{ MAH G}^{-1}$) ARE HELD CONSTANT.105

FIGURE 5.27. THE ENERGY DISTRIBUTION (A) AND CHARGE DISTRIBUTION (B) OF TWO SYSTEMS. CRYSTALLITE RADIUS VARIES ACROSS THE TWO SYSTEMS, WHILE DENSITY ($P = 1.94 \text{ G/CM}^3$), CRYSTALLINE VOLUME FRACTION ($\Phi_c = 0.5$), AND CHARGE ($Q = 147.8 \text{ MAH G}^{-1}$) ARE HELD CONSTANT.....105

FIGURE 5.28. THE ENERGY DISTRIBUTION (A) AND CHARGE DISTRIBUTION (B) OF TWO SYSTEMS. CRYSTALLITE RADIUS VARIES ACROSS THE TWO SYSTEMS, WHILE DENSITY ($P = 1.38 \text{ G/CM}^3$), CRYSTALLINE VOLUME FRACTION ($\Phi_c = 0.5$), AND CHARGE ($Q = 147.8 \text{ MAH G}^{-1}$) ARE HELD CONSTANT.....106

FIGURE 5.29. THE ENERGY DISTRIBUTION (A) AND CHARGE DISTRIBUTION (B) OF THREE SYSTEMS. CRYSTALLINE VOLUME FRACTION VARIES ACROSS THE THREE SYSTEMS, WHILE DENSITY ($P = 1.51 \text{ G/CM}^3$), CRYSTALLITE RADIUS ($R = 7 \text{ \AA}$), AND CHARGE ($Q = 147.8 \text{ MAH G}^{-1}$) ARE HELD CONSTANT.....106

FIGURE 5.30. THE ENERGY DISTRIBUTION (A) AND CHARGE DISTRIBUTION (B) OF THREE SYSTEMS. SPECIFIC CHARGE CAPACITY VARIES
ACROSS THE THREE SYSTEMS, WHILE DENSITY ($\rho = 1.51 \text{ G/CM}^3$), CRYSTALLINE VOLUME FRACTION ($\Phi_c = 0.5$), AND
CRYSTALLITE RADIUS ($r = 7 \text{ \AA}$) ARE HELD CONSTANT.107

1 INTRODUCTION

1.1 BACKGROUND

Low-cost, high-quality lithium batteries are a desirable product in a market that is moving towards cleaner, less expensive, and more efficient energy. The development of these batteries occurs with a trade-off between cost and effectiveness. High-performance batteries are often accompanied by a difficult manufacturing process or a steep financial penalty [1]. On the other hand, batteries developed from low-cost materials are produced at a charge capacity, cycling capability, or safety penalty [1]. Recently however, materials derived from abundant, low-cost lignin sources show promise in achieving a good balance in both financial and performance aspects. Novel processes for the development of this raw material using advanced carbon fiber technologies at Oak Ridge National Laboratory (ORNL) yield superior anode materials in the form of all-carbon composites composed of nanoscale crystalline domains dispersed within an amorphous matrix [1]. Carbon-carbon composite materials have advantages including high reversible capacity, low irreversible capacity loss (shown in **Figure 1.1**), high cycle life due to strong mechanical integrity, and enhanced safety because of a lack of substrate dissolution during overcharge [2].

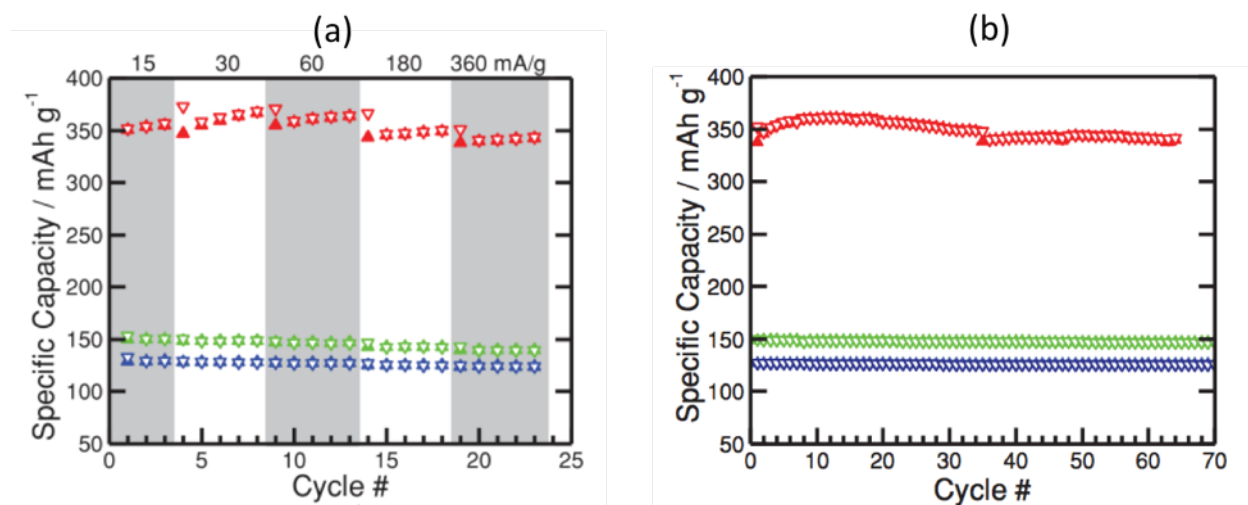


Figure 1.1. (a) Charge storage capacity of lignin carbon fibers carbonized at 1000 °C (red), 1500 °C (green), and 2000 °C (blue) as a function of current in slurry-coated electrodes. (b) Charge capacities as a function of cycling and carbonization temperatures in slurry-coated electrode. Figures and captions from [3].

On the molecular scale, lignin is a complex mix of branched polyaromatic macromolecules containing a large fraction of aromatic rings resulting in a high char yield (over 40 wt. %) after pyrolysis [4, 5]. The difference between lignin-based carbon fiber (LCF) and the more traditional anode material based off of polyacrylonitrile (PAN) is illustrated in **Figure 1.2**. A key step in the manufacturing process is the pyrolyzation and subsequent thermal annealing of lignin fiber. The resulting structural properties of the composite materials are an incompletely understood function of the specific pyrolysis temperature and thermal history. However, as each pyrolysis temperature corresponds to a unique set of experimentally measurable parameters (composite density, crystalline volume fraction, and size of the crystalline nanoparticles), a structure-property relationship can be developed. For these materials, one of these properties is intracrystallite d-spacing. As used here, “d-spacing” refers to the distance between two parallel, or almost parallel, layers of graphene. The motivation for understanding d-spacing is due to the fact that this distance has a direct inverse relationship with the capacity of electric charge accumulation [6], and so is a critical factor in anode performance.

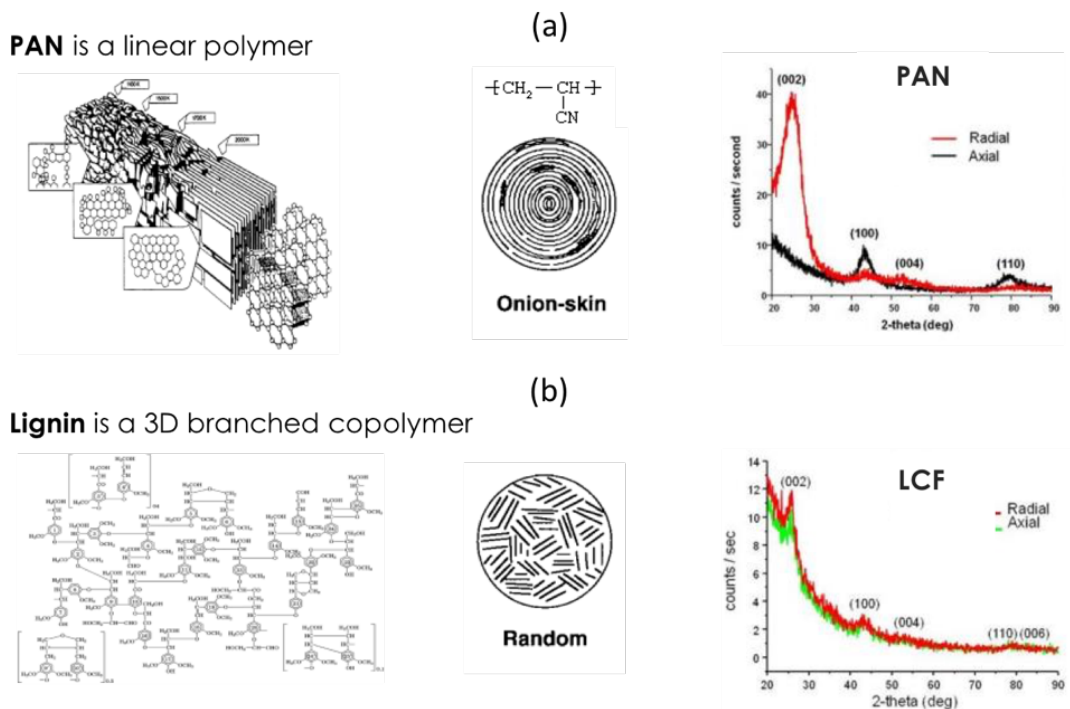


Figure 1.2. (a) Molecular structure of polyacrylonitrile (PAN) exhibits anisotropy in the arrangement of carbon sheets. Figure from [7]. (b) Molecular structure of lignin-based carbon fiber (LCF). The LCF exhibits near perfect turbostratic disorder. Figure from [8].

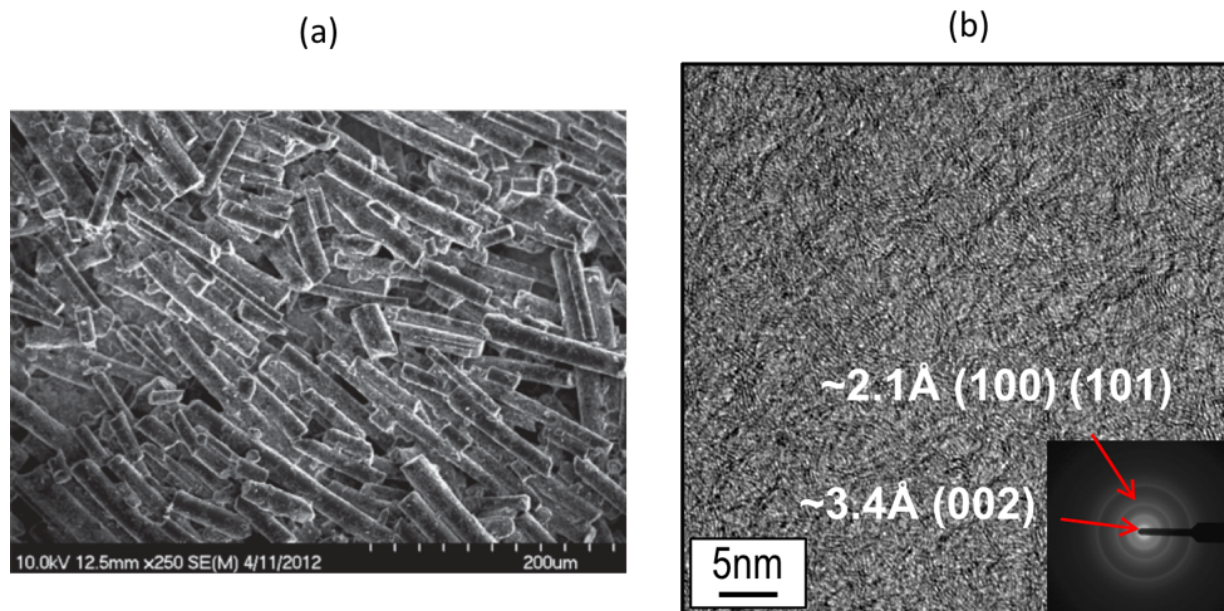


Figure 1.3. (a) Scanning electron images of LCFs ground for particle size reduction and coated onto copper current collectors by slurry coating. (b) High resolution transmission electron microscopy images at a pyrolysis temperature of 2000 °C. The inset images are selective area patterns on the same materials. Figures and captions from [3].

1.2 MOTIVATION AND OBJECTIVES

The objective of this work is develop a computational model to better understand the structure-property relationships of lignin-derived carbon composite anodes developed at Oak Ridge National Laboratory. With a sound theoretical understanding of these relationships, the ultimate goal is to predict the properties of an ideal carbon composite that would lead to novel, high-performing Li-ion battery anodes.

In this research, an atomistic model is developed and studied through the use of molecular dynamics (MD). This procedure simulates the atomic interactions among the crystalline and amorphous domains of the composite systems and reveals both nanoscale and mesoscale phenomena. The properties of interest in these carbon composite systems are those that cannot be easily obtained through experiment, but whose understanding will lead to the development of better anode materials. These properties include the d-spacing between carbon layers (graphene) within the nanocrystallites, the nature of how these nanocrystallites distribute and deform with the amorphous carbon matrix, and the nature of Li-ion storage/transport within this anode material.

1.3 PER CHAPTER SUMMARY

1.3.1 ENTROPY-DRIVEN STRUCTURE AND DYNAMICS IN CARBON NANOCRYSTALLITES

New carbon composite materials are being developed that contain carbon nanocrystallites in the range of 5 Å to 17 Å in radius dispersed within an amorphous carbon matrix. Evaluating the applicability of these materials for use in battery electrodes requires a molecular-level understanding of the thermodynamic, structural, and dynamic properties of the nanocrystallites. Herein, molecular dynamics simulations reveal the molecular-level mechanisms for such experimental observations as the increased spacing between carbon planes in nanocrystallites as a function of decreasing crystallite size. As the width of this spacing impacts Li ion capacity, an explanation of the origin of this distance is relevant to understanding anode performance. It is thus shown that the structural configuration of these crystallites is a function of entropy. The magnitude of out-of-plane ripples, binding energy between layers, and frequency of characteristic planar modes are reported over a range of nanocrystallite sizes and temperatures. This fundamental information for layered carbon nanocrystallites may be used to explain enhanced lithium ion diffusion within the carbon composites.

1.3.2 STRUCTURAL ANALYSIS OF LIGNIN-DERIVED CARBON COMPOSITE ANODES

Lignin-based carbon composite anodes consisting of nanocrystalline and amorphous domains are studied to develop a relationship of structural properties such as crystallite size, intracrystallite d-spacing, crystalline volume fraction, and composite density with their pair distribution functions (PDF), as obtained from both molecular dynamics simulation and neutron scattering.

1.3.3 INTERFACIAL LI-ION LOCALIZATION IN HIERARCHICAL CARBON ANODES

In this work, we study the properties of novel low-cost lignin-based carbon composite anodes for use in Li-ion batteries. The anodes consist of carbon nanocrystallites distributed within an amorphous carbon matrix. We perform a computational study using molecular dynamics simulations of an experimentally validated model of the anode to elucidate the nature of Li-ion storage. We report the discovery of a novel mechanism of Li-ion storage, one in which Li^+ is not intercalated between layers of carbon (as is the case in graphitic anodes), but rather is localized at the interface of crystalline carbon domains. In particular, the effects of Li-ion binding energy on the Li-Li, Li-H, and Li-C pair distribution functions are revealed, along with the effect on charge distribution. Lastly, the atomic environments surrounding the Li-ions are

grouped on the basis of ion energy and then convolved into archetypal structural motifs that reveal deep insight into the geometry of ion localization in disordered systems.

1.3.4 LI-ION LOCALIZATION AND ENERGETICS AS A FUNCTION OF ANODE STRUCTURE

In this work, we study the effect of carbon anode structure on the localization and energetics of Li-ions. A computational molecular dynamics study is combined with experimental results from neutron scattering experiments to understand the effect of composite density, crystallite size, volume fraction of crystalline carbon, and ion loading on the nature of ion storage in novel, lignin-derived composite materials. The effect that lithiation has upon the anode structure is revealed via the pair distribution functions of both the computational models and the experimental materials. The effect of other properties is evaluated using a suite of pair distribution functions corresponding to lithium-carbon, lithium-hydrogen, and lithium-lithium atom pairs. In addition to the pair distribution functions, we use an original technique to extract archetypal structures from the computational models that represent the local atomic environment surrounding Li-ions of different energies. These representations take the form of three-dimensional atomic density distributions. Lastly, the energetics of the Li-ions are understood by relating changes in the energy and charge distributions to changes in structural properties.

2 ENTROPY-DRIVEN STRUCTURE AND DYNAMICS IN CARBON NANOCRYSTALLITES

This chapter is a slightly revised version of a paper by the same title published in the *Journal of Nanoparticle Research* in 2014 by Nicholas McNutt, Qifei Wang, Orlando Rios, and David Keffer:

N. W. McNutt, Q. Wang, O. Rios, and D. J. Keffer, "Entropy-driven structure and dynamics in carbon nanocrystallites", *J. Nanopart. Res.* **16**, 2365 (2014).

The use of "we" in this part refers to the co-authors and the author of this dissertation. My primary contributions to this paper include (1) development of the problem into a work relevant to the study of isolated carbon nanocrystallites, (2) implementation of the simulation methodology, (3) all of the simulation work, and (4) most of the analysis and writing.

Reproduced with permission from Springer, *J. Nanopart. Res.* © 2014 Springer Science+Business Media Dordrecht.

2.1 INTRODUCTION

Nano-carbon materials are of interest due to a variety of novel properties, including enhanced thermal conductivity [9], electronic conductivity [10], and high surface area (over 2600 m²/g) [11], making them of potential interest in energy storage applications. Properties of both graphene and graphite are well known, yet the studies of an intermediate form, layered carbon nanocrystallites, are not as numerous. Recent experimental synthesis and characterization of carbon composites, containing carbon nanocrystallites dispersed within and stabilized by an amorphous carbon matrix, provide practical motivation for the evaluation of carbon nanocrystallites [3]

This paper seeks to clarify the thermodynamics, the structure, and the dynamics of carbon nanocrystallites, with an emphasis on application to energy storage. The significance of this work can be seen through the analogy of the structure and properties of Pt nanoparticles. Molecular Dynamics (MD) simulations have provided an understanding of how the unit cell lattice parameters change as a function of the size of the Pt nanoparticle [12]. This understanding provides insights into their functioning as catalysts [13]. Similarly, the purpose of this contribution is to provide systematic information regarding the structure of carbon nanocrystallites as a function of crystallite size.

Materials composed of carbon fibers can consist of crystalline, layered carbon nanocrystallites of various sizes dispersed within an amorphous carbon matrix [14, 15]. The storage and transport of ions within these composite materials is an area of active interest. It has been shown that the Li-ion intercalation capacity and chemical activity is strongly correlated to particle size thus driving the incorporation of active nanomaterials in energy storage [16-18]. In particular, the d-spacing of these crystallites has a strong inverse relationship with the capacity for electric charge accumulation, making it a crucial factor in lithium-ion anode performance [6]. Currently the extended capacity seen in nanomaterials is thought to be enabled by the reactivity of defect sites while kinetics are enhanced by minimizing the solid state diffusion length [16, 18]. Less is known regarding how the energetics and dynamics of the intercalation process vary with nanocrystallite size. To better understand ion transport into the nanocrystallites, an exploration of the fundamental properties of these nanocrystallites in isolation is required.

The nanoscale structure and energetics of isolated graphite or graphene layers have been studied previously through molecular simulation [19-25]. The structures of isolated graphite and graphene layers have been studied for application in energy storage materials [26-29]. For graphitic layered structures, the interplanar spacing has been reported to be an important factor that affects the sodium atom [26], hydrogen [30], and lithium ion [27] insertions. The dynamics of graphite or graphene layers have been studied mainly because of the finding of “superlubricity” [22, 31-38]. Compared with studies on the thermodynamics, structure, and dynamics of graphite or graphene, a study on carbon nanocrystallites is not reported in the literature. The study of the thermodynamic, structural, and dynamic properties of these nanocrystallites will provide a fundamental understanding that will aid in the development of advanced materials for electrochemical systems. Particularly, it will help the understanding of Li-ion insertion and the transport mechanism in the anodes which incorporate these nanocrystallites.

In this work, we studied the nanoscale thermodynamic, structural, and dynamic properties of isolated layered carbon nanocrystallites (nominal radii of 5, 7 and 17 Å) through MD simulation. The thermodynamic, structural, and dynamic properties are reported as a function of nanocrystallite size and temperature. The computational results are compared with available experimental data for these nanocrystallites and the literature reported values for graphite. This paper is organized as follows. The model and simulation details are given in section 2.2. The results and discussion are presented in section 2.3. The conclusions are listed in section 2.4.

2.2 SIMULATION METHODS

The nanocrystallites modeled in this study were intended to correspond to experimentally synthesized carbon structures from renewable resources [3]. Here, we summarize in one paragraph the experimental synthesis and characterization procedures in order to provide a background for the model nanocrystallites investigated herein. Carbon based energy storage materials with nanoscale microstructures were synthesized from solvent extracted hardwood lignin. Lignin is a complex network of phenyl units bonded through an array of different inter-unit bonds that yields 40 to 60 wt % char after pyrolysis [5, 39]. Conversion of lignin into a nanoscale graphitic material consists of oxidative stabilization to 250 °C in flowing air followed by pyrolysis under inert atmospheres. The size of the nanocrystallites was controlled by systematically varying the annealing temperatures (nominally 1000, 1500 and 2000 °C). Quantitative structural analysis of x-ray diffraction measurements taken from converted lignin carbon fibers were used to calculate the mean particle size and the lattice parameters of the nanocrystallites [15, 40]. Peak broadening was correlated to the mean particle size using Scherrer analysis [41] while the d-spacing was measured directly from the position of the peak corresponding to the (002) plane.

A structural model of the carbon nanocrystallite is initially constructed by cutting a sphere from a sample of bulk graphite with AB stacking of layers. Edge carbon atoms that are bonded to only one other carbon are removed. The three nanocrystallites are shown in **Figure 2.1**. The nominal radii of 5, 7 and 17 Å (corresponding to 85, 136, and 2,207 atoms respectively) are selected to match the experimental data to which we will compare. Within a single plane, the structure is entirely carbon in a hexagonal pattern. The distance between adjacent carbon atoms is 1.42 Å and the bond angle is 120°.

The MD simulations were conducted using LAMMPS [42]. The OPLS-AA potential was used [43]. The total interactions include bond stretching, angle bending, bond torsion, in-plane nonbonded interaction for atoms separated by three bonds or more, and the inter-plane nonbonded interaction. The nonbonded interactions are characterized by the Lennard-Jones potential. The stretching, bending, and Lennard-Jones potential parameters are taken from the work of Tsai and Tu [25] on graphite. The torsion potential parameters are taken from the work of Fileti, Dalpian [44] on graphene.

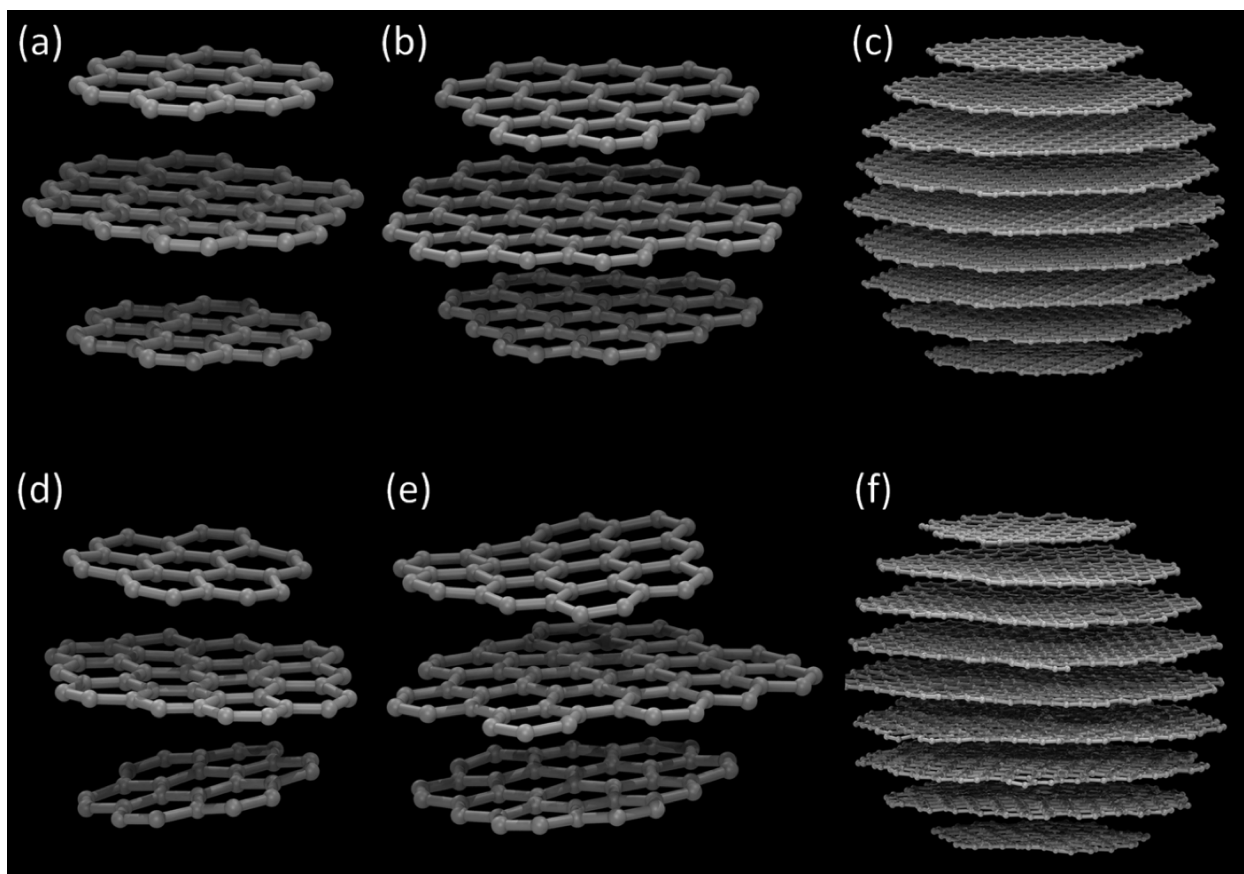


Figure 2.1. Molecular representations of three carbon nanocrystallites: (a): $r = 5 \text{ \AA}$, at 0 K; (b): $r = 7 \text{ \AA}$, at 0 K; (c): $r = 17 \text{ \AA}$, at 0 K; (d): $r = 5 \text{ \AA}$, at 300 K; (e): $r = 7 \text{ \AA}$, at 300 K and (f): $r = 17 \text{ \AA}$, at 300 K. The scale is different for each crystallite.

The OPLS-AA potential was used as the primary method of simulation because these nanocrystallites are present in much larger composite systems, consisting of hundreds of thousands of atoms. As a means of additionally validating the potential, three systems were also simulated using the AIREBO potential [45]. The AIREBO potential allows for C-C bond breaking. In this system, there is no C-C bond breaking, as evidenced through the AIREBO simulations we performed. Moreover, the structural and energetic information from the OPLS-AA and AIREBO potentials were qualitatively similar. Therefore, we chose to use the computationally less expensive (but still accurate) OPLS-AA potential. A few results from the AIREBO simulations are also presented.

The nanocrystallite is placed in a cubic simulation box in a microcanonical (NVE) ensemble. We chose not to simulate in the canonical (NVT) ensemble to eliminate the possibility that the thermostat would introduce artifacts into the largely harmonic modes of the small crystallites. Thus, the temperatures reported in our data correspond to the mean value of temperature over the duration of each simulation. The r-RESPA algorithm developed by Tuckerman, Martyna [46] was used to integrate the equations of motion. The time step of the pairwise interactions was 2 fs and the time step of the bonded interactions was 0.2 fs. The cut-off distance used was 20 Å. A temperature range from 50 K to 420 K was generated by changing the initial velocities. Every simulation was run for 1 ns of data production.

2.3 RESULTS AND DISCUSSION

In this section, important findings on the thermodynamics, structure, and dynamics of three nanocrystallites (radius, $r = 5, 7$ and 17 Å) are reported and compared with the available literature-reported data and theory. First, the thermodynamic properties are reported as a function of nanocrystallites size and temperature. Second, the structural changes are reported as a function of nanocrystallite size and temperature. Finally, we examine the dynamics of the nanocrystallite with a radius of 5 Å as a function of temperature. Through these studies, we obtained the understanding of the thermodynamics, structure, and dynamics of these carbon nanocrystallites.

2.3.1 THERMODYNAMIC PROPERTIES

In this section, the thermodynamic properties of the carbon nanocrystallites are reported. Based on the potential used, there are four contributions to the intraplanar potential energy, namely bond-stretching, bond-bending, bond-torsion, and nonbonded interactions for atoms separated by at least three bonds. There is also an interplanar potential energy due to nonbonded interactions between planes. For carbon

nanocrystallites with layered structures, the intraplanar and interplanar potentials have different impacts on the structure and dynamics. The intraplanar potentials maintain the planarity of a given layer. The interplanar potentials bind the layers together. Therefore, it is useful to study the contributions to the total potential individually. In **Figure 2.2**, the (a) stretching, (b) bending, (c) torsion, (d) intraplanar nonbonded, (e) interplanar nonbonded, and (f) total potential energy are shown as a function of temperature for the three nanocrystallites. These properties are averaged over the production run. All energies are reported on an intensive (per mole) basis. The energy associated with the stretching, bending, and torsion modes increases with temperature. There is not a large difference in these three energies as a function of crystallite size. In the inset of **Figure 2.2(a)**, (b), and (c), one can observe that the energies are slightly higher for the larger nanocrystallites. The largest noise appears in the smallest nanocrystallites because it has the fewest number of atoms. In **Figure 2.2(d)**, the intraplanar nonbonded potential energy also increases with temperature, though the difference as a function of nanocrystallite size is now significantly greater, with the larger crystallite having a larger (less favorable) energy. The intraplanar nonbonded energy is positive because in the OPLS-AA potential, the nonbonded interactions include atoms separated by three bonds. At this distance (2.84 Å), the nonbonded interaction is unfavorable. The increase in these intraplanar energies corresponds to greater fluctuations from planarity in the layer with increasing temperature. This indicates that the out-of-plane fluctuations (or ripples of layers) become more significant at elevated temperatures. This observation is in complete agreement with the fact that the intraplanar energetic contributions in **Figure 2.2(a)** through (d) increase with increasing temperature.

In **Figure 2.2(e)**, the interplanar nonbonded interaction energy is negative (favorable) and increases (becomes less favorable) with temperature. It is also observed in **Figure 2.2(e)** that the interplanar nonbonded interaction energy becomes more favorable as the size of the nanocrystallite increases, which – as shall be shown in the next section – corresponds to a decrease in average d-spacing with an increase in crystallite size.

The sum of the five contributions to the total potential energy is shown in **Figure 2.2(f)**. The total potential energy increases (becomes less favorable) with increasing temperature, as was the case for the four intraplanar nonbonded components and one interplanar component. The total potential energy decreases (becomes more favorable) with increasing particle size, as was the case with the interplanar component, but not the case for the four intraplanar nonbonded components.

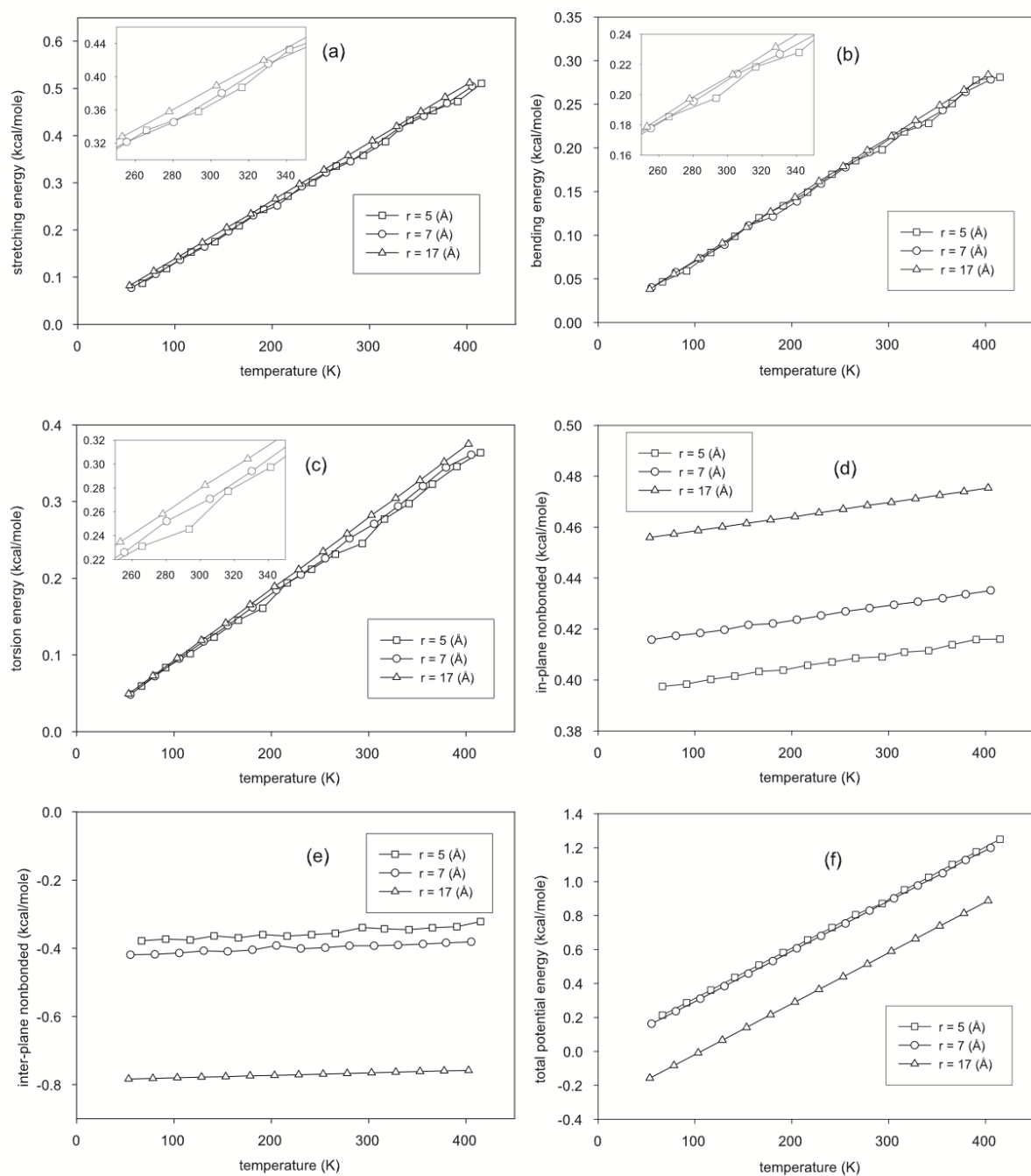


Figure 2.2. Individual potential energy as a function of temperature for the three carbon nanocrystallites. (Energy is on a per atom basis.)

Thus the temperature dependence of the potential energy is dominated by all potential modes whereas the size dependence is governed by the interplanar mode.

It is interesting to further study the interplanar nonbonded potential. The absolute value of the interplanar nonbonded potential energy is often referred to as the binding energy for AB stacking graphite layers [22]. The literature reported value for the binding energy of AB stacking graphite is 52 meV per atom at room temperature [21, 47]. In this work, the binding energy at room temperature is 14.7 ($r = 5$ Å), 17.0 ($r = 7$ Å) and 33.2 ($r = 17$ Å) meV/atom, significantly lower than that for graphite. We shall see in the next section that this binding energy is correlated to the larger d-spacing of the nanocrystallites (3.9, 3.55, and 3.4 Å) relative to graphite (3.354 Å) [47]. The lower binding energy suggests a better structure for ion intercalation, since it becomes easier for the ion to insert between the layers. Low binding energy is also good for exfoliation and provides good mechanical properties when being used as a component of nanocomposites [25].

Based on the variation of total energy on temperature, we extracted the constant-volume heat capacity (C_v) and entropy change relative to the lowest temperature for these nanocrystallites. The calculation of heat capacity is based on the central finite difference of total energy over temperature rather than the fluctuation of the potential energy, since the former procedure has been shown to provide more statistically reliable results [48]. We did not use any noise reduction filter in the potential energy, so the variations that appear in the heat capacity, especially in the smallest system, are simply due to the common issues associated with numerical differentiation of data with some noise. The calculation of entropy change is based on the integration of heat capacity over temperature. In **Figure 2.3**, we show the temperature dependence of heat capacity and entropy change for the three nanocrystallites. From **Figure 2.3(a)**, we observed that the heat capacities for the three nanocrystallites are in the range of 0.0057 to 0.0061 kcal/mol/K and show no apparent temperature dependence in the range studied. There is no available experimental heat capacity of these nanocrystallites for comparison. A reference point is the constant pressure heat capacity for graphite, which is 0.002 kcal/mol/K at 300 K [49]. The higher heat capacity of the nanocrystallites is due to the additional degrees of freedom in the nanocrystallites, as seen in the analysis of dynamics which follows. We note that the heat capacity of a composite material will be a combination of the crystalline and amorphous domains.

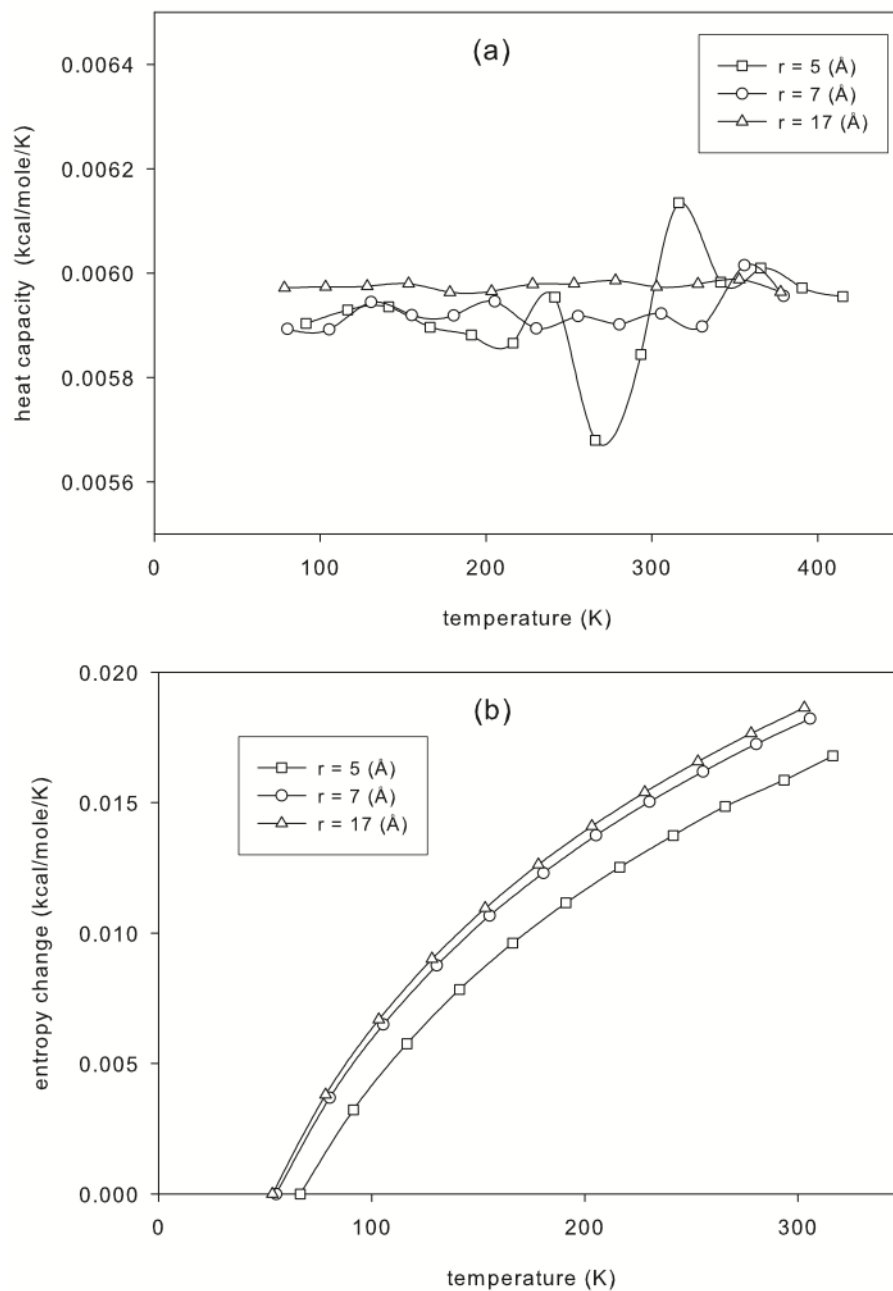


Figure 2.3. Heat capacity (a) and entropy change (b) as a function of temperature for the three carbon nanocrystallites.

In **Figure 2.3(b)**, the entropy change as a function of temperature is shown for each of the three nanocrystallites. The entropy change is measured relative to the lowest simulation temperature for each crystallite. (Because we simulated in the NVE ensemble, this temperature is not the same for each crystallite.) The entropy change increases with temperature for the three systems and the entropy change with respect to temperature is largest for the largest crystallite. We shall show in the following section that the d-spacing increases with temperature for the three crystallites.

2.3.2 *STRUCTURAL PROPERTIES*

The equilibrium structures are specifically studied for the three nanocrystallites. The structure of the carbon nanocrystallite can be characterized in several ways. In order to characterize the geometry between layers, four measures are employed here. The first is the sliding distance. The sliding distance measures the displacement of one plane relative to another along an axis parallel to the planes. As shown in **Figure 2.4**, the sliding distance is defined as d-sliding. The second measure is the breathing distance, which characterizes the perpendicular separation between layers – the d-spacing. The breathing distance is defined as d-breathing in **Figure 2.4**. The third measure is the rocking angle, which characterizes the angle between two adjacent planes. The rocking angle is also defined in **Figure 2.4**. The fourth measure is the center-of-mass (COM) distance, which is likely some linear combination of the other modes and is defined as the distance between the center of mass of two adjacent planes (COM in **Figure 2.4**). We include the dependent COM measure because in the work on graphene layers, the relative center of mass separation is used to study the sliding motion [22]. In addition to these four interplanar measures, we also report one intraplanar measure, which is the standard deviation of the perpendicular distance of each carbon atom in a layer from the best-fit mathematical plane through all of the carbon atoms in that layer. Focusing on these four modes of motion provides the essential information of interest and is pursued rather than a full normal mode analysis, resulting in 3N modes.

In **Figure 2.5**, the intraplanar measure is presented first. The standard deviation of the carbon distance from the plane is plotted as a function of temperature for all three nanocrystallites. The standard deviation increases with temperature and particle size, consistent with the observation of the intraplanar energies (**Figure 2.2 (a)-(d)**). In **Figure 2.2**, we have observed that the intraplanar energy (for stretching, bending, torsion, and intraplanar nonbonded interactions) increases with temperature and particle size, indicating increased out-of-plane fluctuations for the carbon atoms. The results shown in **Figure 2.5** further prove that the out-of-plane fluctuations increase with particle size and temperature. These out-of-plane distortions are similar in scale to those observed in free standing graphene [50, 51].

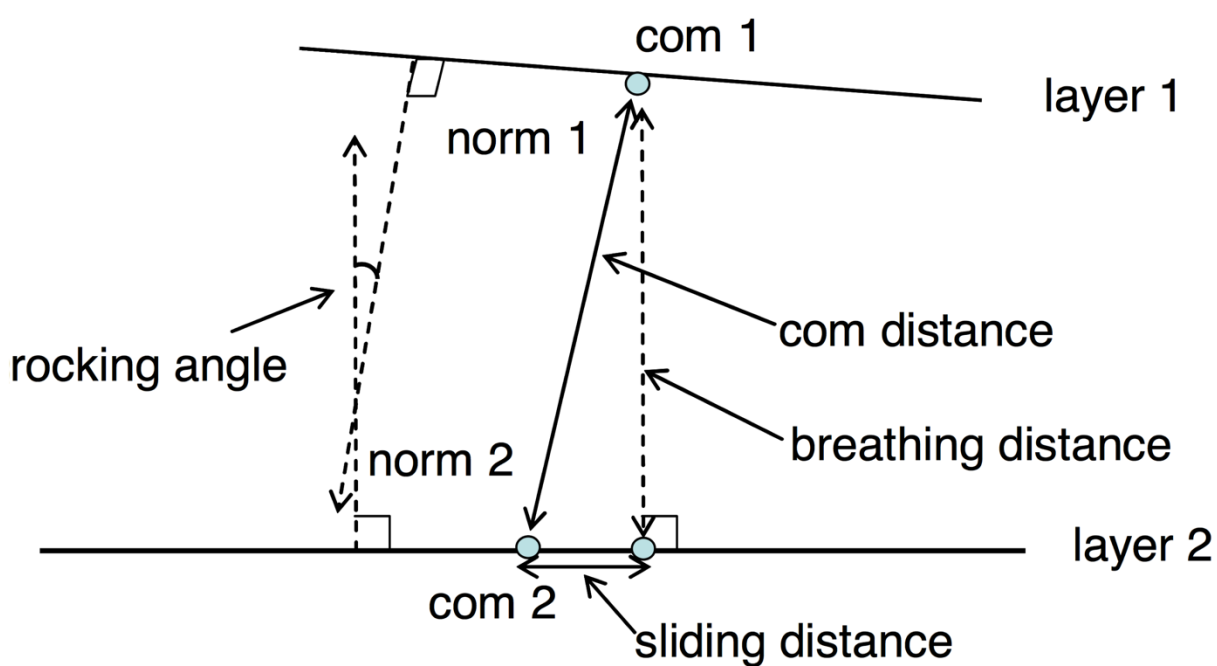


Figure 2.4. Schemes of definitions of different geometrical characterizations (COM 1: center of mass positions of layer 1; COM 2: center of mass positions of layer 2; norm 1: norm vector of layer 1; norm 2: norm vector of layer 2).

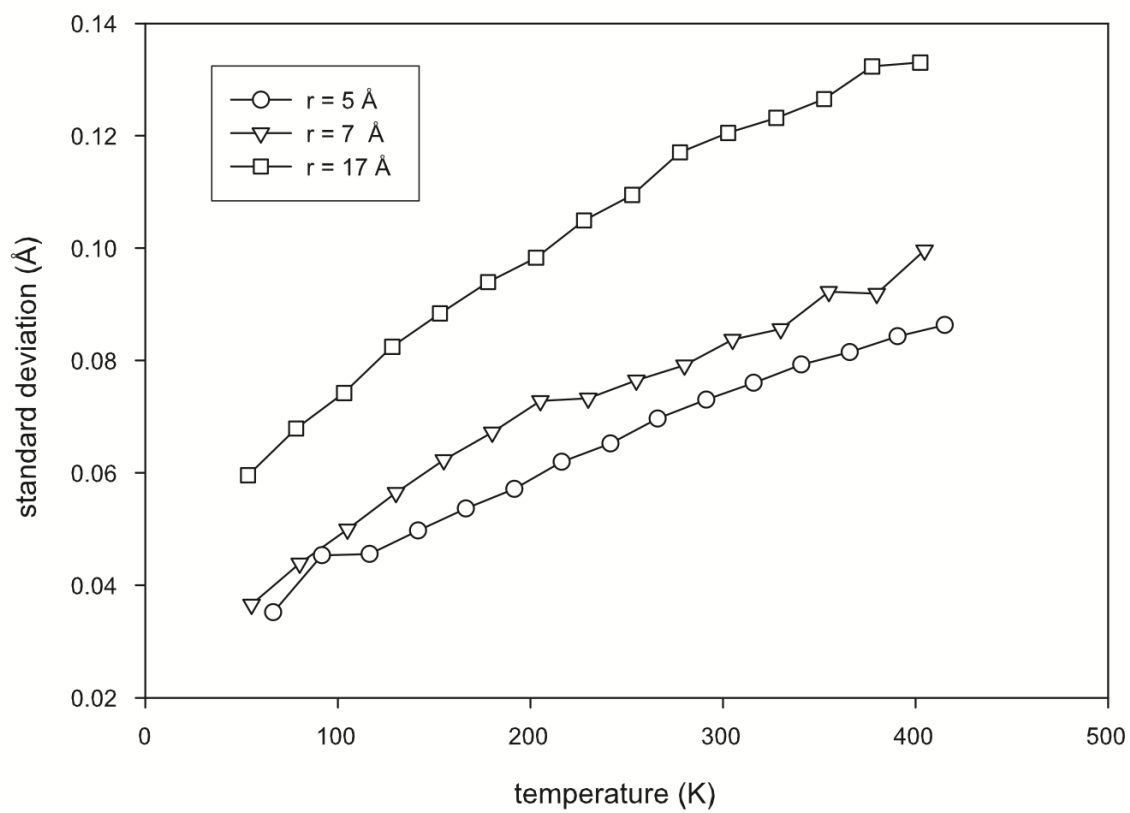


Figure 2.5. The standard deviation of the carbon distance from the plane as a function of temperature.

In **Figure 2.6**, the average values of the interplanar measures, including (a) sliding distance, (b) breathing distance, (c) rocking angle, and (d) COM distance, are plotted as a function of temperature for the three nanocrystallites. We observe that all four interplanar measures increase with increasing temperature. That is, with increasing temperature, the planes (on average) have slid farther away from the center of the crystallite, have greater separation between them, and are less parallel to each other. The COM of adjacent planes are also farther away from each other.

From **Figure 2.6**, it is also clear that at any given temperature, the value of each of the four interplanar measures decreases with increasing nanocrystallite size. In other words, with increasing nanocrystallite size, the planes have (on average) slid a smaller distance away from the center of the crystallite, have less separation between them, and are more parallel to each other. The COM of adjacent planes are also closer to each other. Furthermore, the sensitivity to temperature for each of the four interplanar measures decreases with increasing nanocrystallite size.

It is appropriate at this point, having presented the structural data, to discuss the driving force for a change in d-spacing (the distance associated with the breathing mode). The driving force for a change in d-spacing as a function of crystallite size is entropy. To demonstrate that this is an entropically driven change in structure, one begins with the Helmholtz free energy, A ,

$$A = U - TS$$

where U is the internal energy, S is the entropy, and T is the absolute temperature. At 0 K, there is no entropic contribution to the free energy. The d-spacing is defined solely by the energetic contribution to the free energy. For any given crystallite size at any arbitrary higher temperature, there is a d-spacing that corresponds to the minimum in the internal energy. We define a structural state, point 1, such that

$$A_1 = U_1 - TS_1 = U_{min} - TS_1$$

This structural state is not the one that is observed in the simulation at a finite temperature since the d-spacing associated with the minimum in free energy does not coincide with the d-spacing associated with the minimum in internal energy. We define a structural state, point 2, which is the equilibrium state observed in the simulation,

$$A_2 = A_{min} = U_2 - TS_2$$

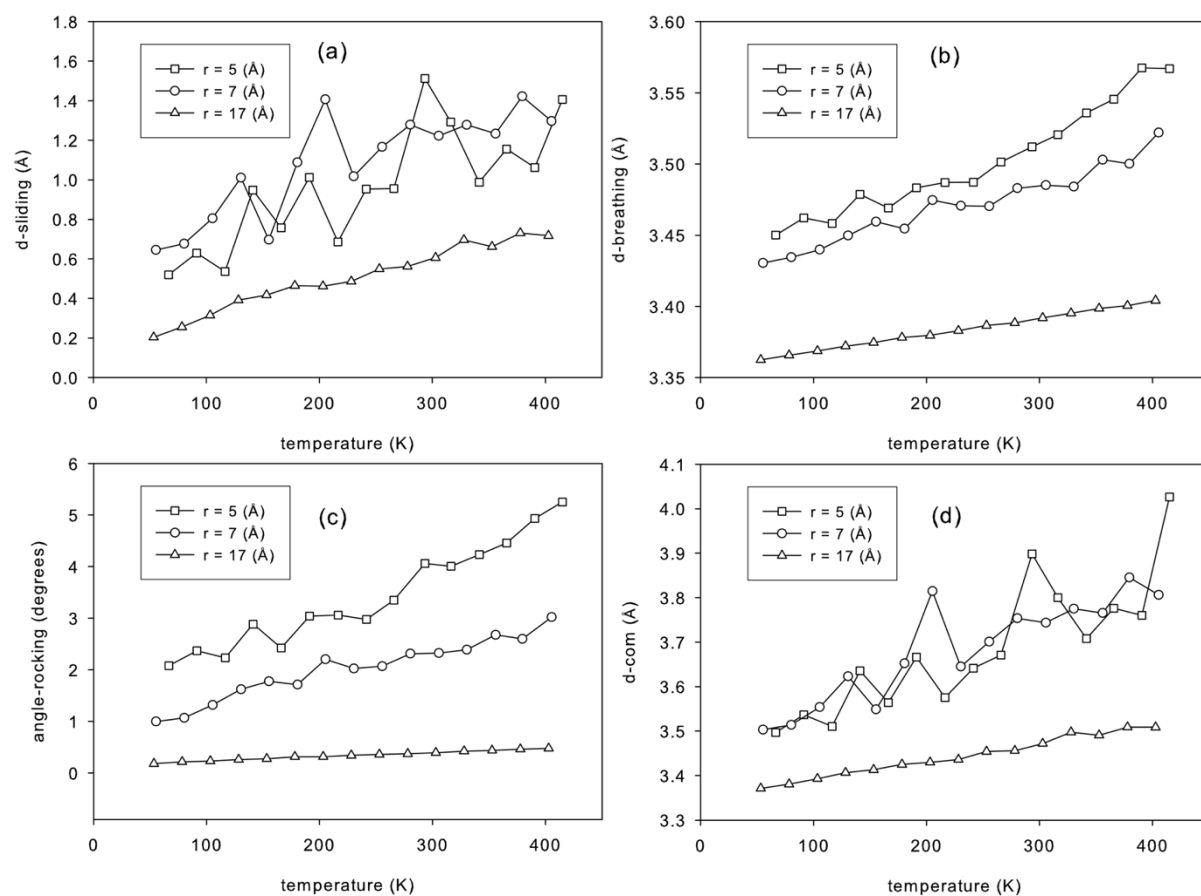


Figure 2.6. Structures as a function of temperature for the three carbon nanocrystallites (d-sliding: horizontal separation of two adjacent layers; d-breathing: vertical separation of two adjacent layers; rocking-angle: angle of two normal vectors of two adjacent layers; d-COM: center of mass separation of two adjacent layers).

The difference between states 2 and 1 is given by

$$\Delta A = A_2 - A_1 = U_2 - U_1 - T(S_2 - S_1) = \Delta U - T\Delta S$$

Because the equilibrium state is a minimum in free energy, we know that $A < 0$. By the definition of state 1, in which the internal energy is a minimum, we know that $U > 0$. (In fact at $T = 293$ K, for the crystallite with a radius of 5 \AA , the internal energy at the equilibrium state corresponding to a d-spacing [breathing] of 3.51 \AA is 1.74 kcal/mol . We cannot perform an equilibrium simulation at 293 K with a d-spacing corresponding to that associated with the minimum in internal energy. However at 0 K, the minimum internal energy is 0.013 kcal/mol , corresponding to a d-spacing of 3.41 \AA , which results in a positive U of 1.73 kcal/mol).

From these equations, two mathematical consequences emerge. First, the change in entropy must be positive,

$$\Delta S > 0$$

In other words, as the d-spacing increases, the entropy of the crystallite also increases. The second consequence is that the change in the entropic contribution to the free energy upon a change in d-spacing is greater in magnitude than the change in energy,

$$T\Delta S > \Delta U$$

In other words, the entropic advantage gained by increasing the d-spacing is greater than the energetic penalty paid by increasing the d-spacing. Therefore, the structural change can be said to be entropically driven.

The d-spacing is of particular interest for materials composed of these nanocrystallites with applications for lithium ion battery anodes, where the lithium ion is stored in an intercalated state. In **Table 2.1**, we compared the d-breathing and d-COM from MD simulation with that of experiments for carbon fibers composed of these three nanocrystallites. Both OPLS-AA [43] and [45] potential models were used in MD simulations to study the variance of d-spacing as a function of the choice of interaction potential. The calculated breathing distance agrees with the experiments on composite materials with these characteristic crystallite sizes [15, 40] for the $r = 7 \text{ \AA}$ and $r = 17 \text{ \AA}$ systems but deviates with experiments for the $r = 5 \text{ \AA}$ system. The calculated d-COM agrees with the experiments for the $r = 5 \text{ \AA}$ and $r = 17 \text{ \AA}$ systems but deviates with experiment for the $r = 7 \text{ \AA}$ system.

Table 2.1. Comparison of measures of interplanar spacing (breathing and COM distances) for the three carbon nanocrystallites around 291 K ($r = 5 \text{ \AA}$: 293 K; $r = 7 \text{ \AA}$: 280 K; $r = 17 \text{ \AA}$: 278 K, experiment data is taken at 291 K [15]).

Type	breathing distance (\AA) - MD		COM distance (\AA) - MD		d-spacing (\AA) exp.
	OPLS-AA	AIREBO	OPLS-AA	AIREBO	
$r = 5 \text{ \AA}$	3.51	3.61	3.89	3.91	3.89
$r = 7 \text{ \AA}$	3.48	3.60	3.75	3.84	3.67
$r = 17 \text{ \AA}$	3.39	3.48	3.45	3.56	3.51

The calculated results by either method capture the trend of experimental interplanar spacing of the three nanocrystallites and show little dependence on interactions potentials. The d-spacings predicted using the AIREBO potential are slightly larger than those predicted using the OPLS-AA potential.

2.3.3 DYNAMICAL PROPERTIES

To study the dynamics behavior of the three nanocrystallites, we analyzed the four interplanar modes described above. In **Figure 2.7**, the sliding distance, breathing distance, rocking angle, and COM distance are plotted as functions of time for the $r = 5 \text{ \AA}$ nanocrystallite near 291 K. Only 30 ps of data is shown for visual clarity, but samples from the entirety of the simulation were recorded. In the $r = 5 \text{ \AA}$ nanocrystallite, there are three planes, with plane 2 being in the middle. The values of all four modes are shown for the combination of both the 1-2 (top and middle) and 2-3 (middle and bottom) planes. All four modes fluctuate around average values. All four modes show some periodicity with simulation time.

One observes in **Figure 2.7(b)** that the breathing distance of the 1-2 layers is highly positively correlated with the breathing distance of the 2-3 layers. As the distance between the 1-2 layers increases, so too does the distance between the 2-3 layers. Similarly, as the distance between the 1-2 layers decreases, so too does the distance between the 2-3 layers. Thus, this is a breathing mode, representing expansion and contraction of the nanocrystallite in the axis normal to the planes. The alternative motion – a mode where the 1-2 and 2-3 distances are negatively correlated in time and for which the middle plane bounces between two outer planes that maintain a constant distance from each other – is not observed. While this modal analysis is certainly not a complete normal mode analysis, this breathing mode likely corresponds to one of the eigenvectors of the crystallite.

Similarly, in **Figure 2.7(a)**, the sliding mode shows a positive correlation between the sliding distance of layers 1-2 and that of layers 2-3. It is not clear whether the mode corresponds to both the top and bottom layers moving in one direction (e.g. to the right) while the middle layer moves to the left, or rather whether the top layer moves to the right and the bottom layer to the left, while the middle layer is stationary. Either of these two modes fit the observed data. A movie of the crystallite is available in an archived, online website [40] indicates that it is the latter rather than the former mode that is active.

In order to obtain the frequencies associated with these modes, we performed Fast Fourier Transforms [52] on the transient data for all four modes. The resulting spectra for the $r = 5 \text{ \AA}$ nanocrystallite at select temperatures are shown in **Figure 2.8**. The fundamental frequency for the sliding mode is 0.4 THz (dashed line in **Figure 2.8(a)**), close to 0.336 THz, a value reported for the sliding mode of graphite using the

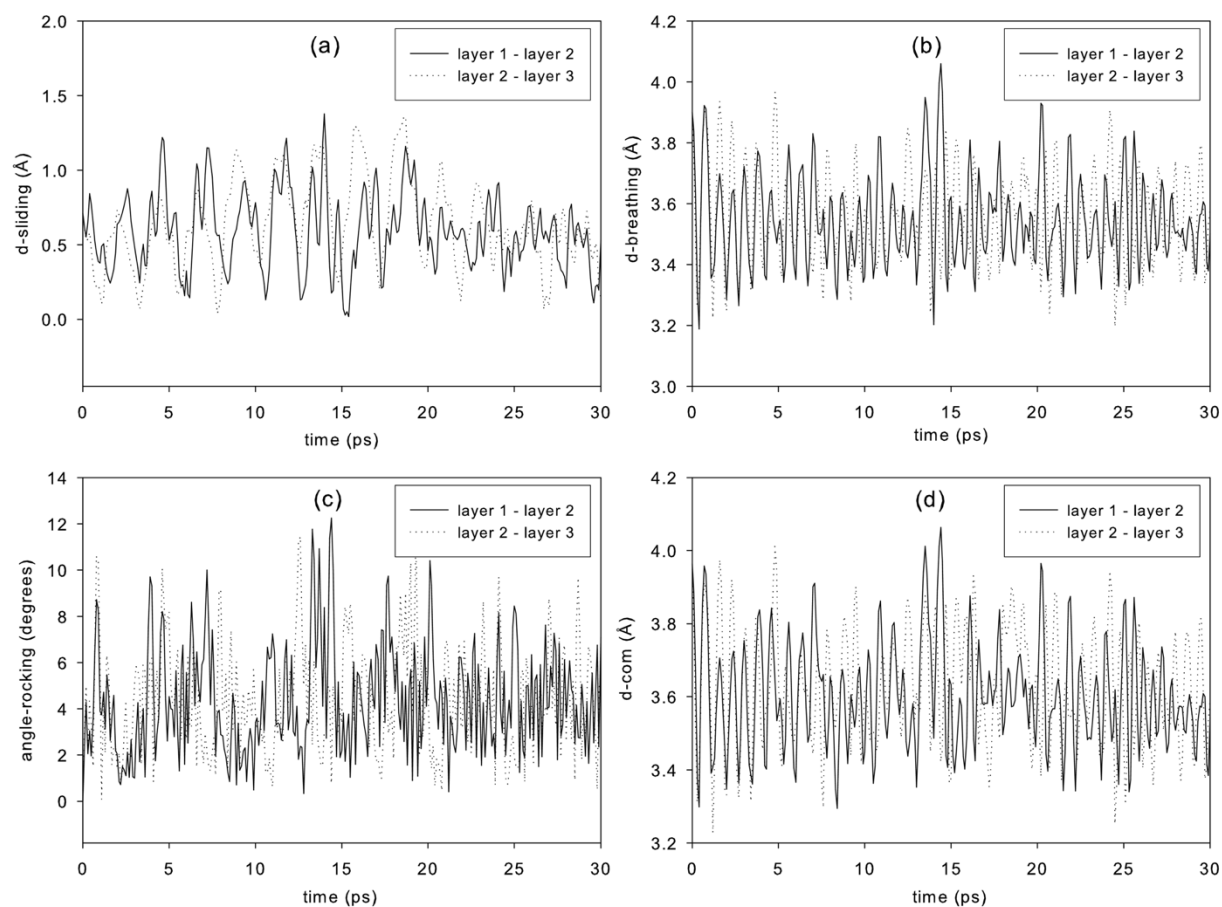


Figure 2.7. Structures as a function of time for the nanocrystallite with $r = 5 \text{ \AA}$ at 266 K. (d-sliding: horizontal separation of two adjacent layers; d-breathing: vertical separation of two adjacent layers; rocking-angle: angle of two normal vectors of two adjacent layers; d-COM: center of mass separation of two adjacent layers).

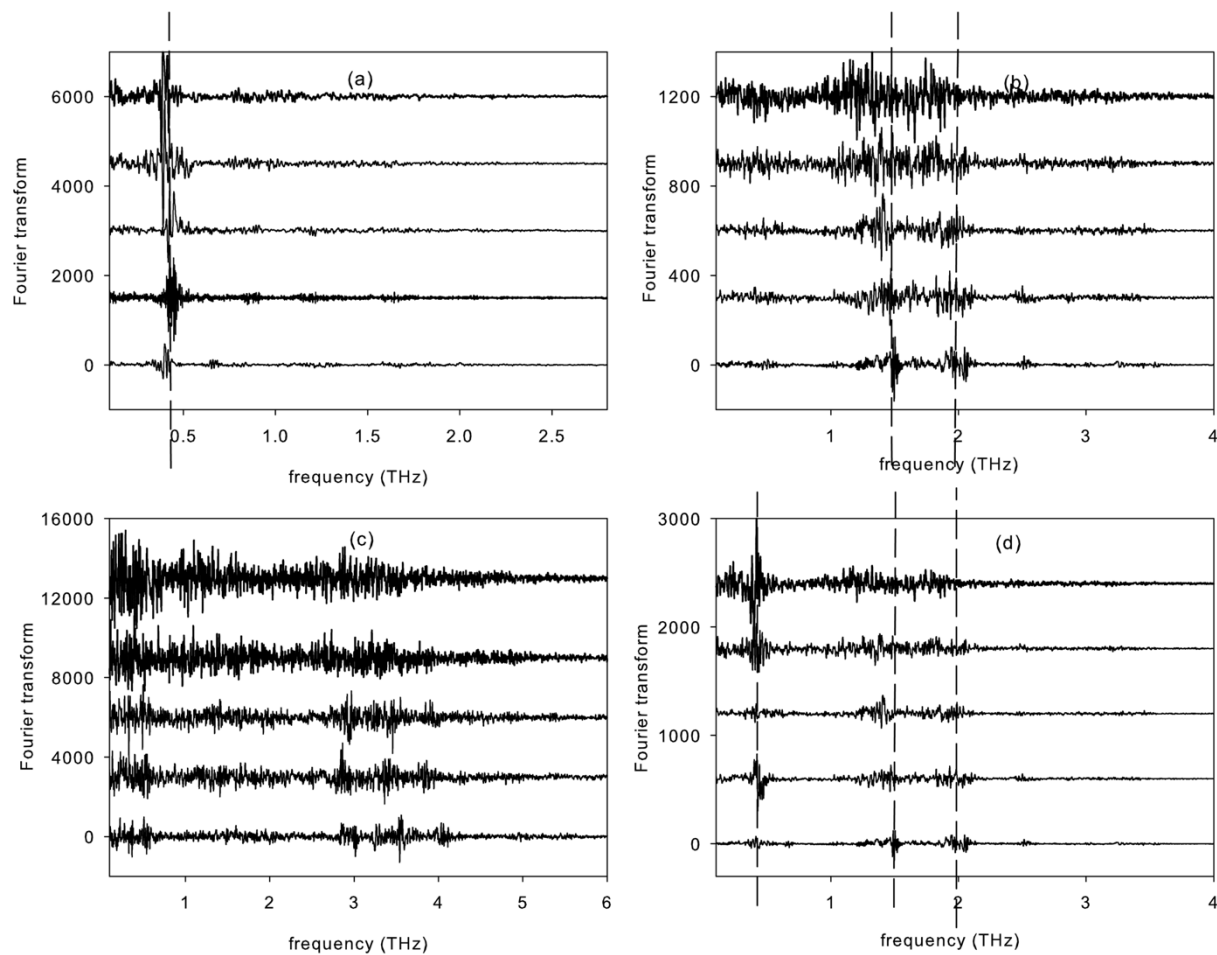


Figure 2.8. Calculated Fourier transforms of (a): horizontal separation (d-sliding), (b): vertical separation (d-breathing), (c): angle rocking and (d) center of mass separation (d-COM) for the top two layers of the nanocrystallite with $r = 5 \text{ \AA}$ at different temperatures (from bottom to top: 67 K, 141 K, 216 K, 293 K, 366 K).

Lennard-Jones potential [22]. The breathing mode shows two major fundamental frequencies at 1.45 and 1.95 THz, as shown in **Figure 2.8(b)**. The spectrum for the rocking mode has a variety of features between 3 and 4 THz. In all cases, the distinct features of the spectra are more pronounced at lower temperatures. In **Figure 2.8(d)**, the COM mode is presented. It shows three major peaks, corresponding to the one peak from the sliding mode (~ 0.4 THz) and two peaks from the breathing mode (dashed lines at 1.5 and 1.9 THz). Clearly, sliding and breathing distances contribute to the COM distance. The rocking angle does not contribute to the COM distance and is not observed in the COM spectrum. We note here that the experimentally measured fundamental frequency reported for the sliding motion of graphite is 1.5 THz [53], close to 1.45 THz, one of breathing frequencies reported here. Also note that this comparison is between nanocrystallites and bulk graphite, which may be responsible for the discrepancy. Further study is warranted.

2.4 CONCLUSIONS

The thermodynamic, structural, and dynamic properties of carbon nanocrystallites have been studied through molecular dynamics simulations. The results show that the d-spacing increases with decreasing nanocrystallite size, in agreement with experimental observations from composite materials containing carbon nanocrystallites of different sizes. It is found that the increase in d-spacing is due to entropic effects. The binding energy between planes commensurately weakens with decreasing nanocrystallite size. The bonded potential energy (stretching, bending, and torsion) and in-plane nonbonded potential energy become less favorable with nanocrystallite size. The heat capacities of the nanocrystallites are in the range of 0.0057 to 0.0061 kcal/mole/K, significantly higher than bulk graphite. Three types of layer motion (breathing, sliding, and rocking angle) are observed for all three nanocrystallites at different temperatures. The Fourier transforms were conducted for all three types of motions and center of mass motion. The results show that there is a major frequency for sliding motion at 0.4 THz, which is close to the literature-reported value for graphite using the same potential. There are two major frequencies for breathing motion, with one at 1.45 THz and the other at 1.95 THz. These frequencies show little apparent variation with temperature over the range studied here. The study provides fundamental understanding of the physical properties of these layered carbon nanocrystallites. This work can aid in the understanding of Li-ion intercalation in composite anodes, which have shown strong dependence of ion capacity on crystallite size [3], and a strong inverse relationship between electric charge capacity and crystalline d-spacing width [6].

2.5 ACKNOWLEDGMENTS

Q.W. was supported by the Joint Directed Research and Development program (JDRD) of the University of Tennessee Science Alliance. N.M. was supported by a grant from the Oak Ridge Associated Universities High Performance Computing Program and by a grant from the Sustainable Energy Education and Research Center of the University of Tennessee. This research project used resources of the National Institute for Computational Sciences (NICS) supported by NSF under agreement number: OCI 07-11134.5. This research was also sponsored in part by the Laboratory Directed Research and Development Program of Oak Ridge National Laboratory, managed by UT-Battelle, LLC, for the U. S. Department of Energy. We thank Dr. Don Nicholson for invaluable advice during the preparation of this manuscript.

3 STRUCTURAL ANALYSIS OF LIGNIN-DERIVED CARBON COMPOSITE ANODES

This chapter is a slightly revised version of a paper by the same title published in the *Journal of Applied Crystallography* in 2014 by Nicholas McNutt, Orlando Rios, Mikhail Feygenson, Thomas Proffen, and David Keffer:

N. W. McNutt, O. Rios, M. Feygenson, T. E. Proffen, and D. J. Keffer, "Structural analysis of lignin-derived carbon composite anodes", *J. Appl. Cryst.* **47**, 1577-1584 (2014).

The use of "we" in this part refers to the co-authors and the author of this dissertation. My primary contributions to this paper include (1) development of the problem into a work relevant to the study of lignin-derived carbon composite Li-ion battery anodes, (2) experiments conducted at the NOMAD beam line at the Spallation Neutron Source at Oak Ridge National Laboratory, (3) implementation of the simulation methodology, (4) all of the simulation work, and (5) most of the writing.

Reproduced with permission from *J. Appl. Cryst.* © 2014 International Union of Crystallography.

3.1 INTRODUCTION

Low-cost, high-quality lithium batteries are a desirable product in a market that is moving towards cleaner, less expensive, and more efficient energy. The development of these batteries occurs with a trade-off between cost and effectiveness. High-performance batteries are often accompanied by a difficult manufacturing process or a steep financial penalty [1]. On the other hand, batteries developed from low-cost materials are produced at a charge capacity, cycling capability, or safety penalty [1]. Recently however, materials derived from abundant, low-cost lignin sources show promise in achieving a good balance in both financial and performance aspects. Novel processes for the development of this raw material using advanced carbon fiber technologies at Oak Ridge National Laboratory (ORNL) yield superior anode materials in the form of all-carbon composites composed of nanoscale crystalline domains dispersed within an amorphous matrix [3]. Carbon-carbon composite materials have advantages including high reversible capacity, low irreversible capacity loss, high cycle life due to strong mechanical integrity, and enhanced safety because of a lack of substrate dissolution during overcharge [2].

On the molecular scale, lignin is a complex mix of branched polyaromatic macromolecules containing a large fraction of aromatic rings resulting in a high char yield (over 40 wt. %) after pyrolysis [4, 5]. A key step in the manufacturing process is the pyrolyzation and subsequent thermal annealing of lignin fiber.

The resulting structural properties of the composite materials are an incompletely understood function of the specific pyrolysis temperature and thermal history. However, as each pyrolysis temperature corresponds to a unique set of experimentally measurable parameters (composite density, crystalline volume fraction, and size of the crystalline nanoparticles), a structure-property relationship can be developed. For these materials, these properties include intracrystallite d-spacing. As used in this paper, “d-spacing” refers to the distance between two parallel, or almost parallel, layers of graphene. The motivation for understanding d-spacing is due to the fact that this distance has a direct inverse relationship with the capacity of electric charge accumulation [6], and so is a critical factor in anode performance.

In this work, we used neutron diffraction on three lignin-derived carbon samples to obtain experimental pair distribution functions (PDFs) to compare with our simulation results. In contrast to X-rays, neutrons are more sensitive to the light elements, and neutron time-of-flight diffraction enables higher resolution PDFs because of the broader Q-range accessible [54]. In experimental PDFs, peak position, height, and width are attributed to the inter-atomic distance, coordination number, and thermal motion of atoms.

Although such qualitative information can be directly observed in the experimental PDF, a fundamental understanding of the local structure on an atomic level requires advanced analytical methods to extract quantitative structural information [55-57]. It is therefore necessary to develop a predictive model that reproduces the experimental PDF.

Decomposition of the PDF into individual components is possible in a simulation, whereas in experimental neutron PDFs, only isotope substitution experiments can differentiate between partial PDFs. Such a decomposition enables an unambiguous identification of the origin of each feature in the PDF. Although multiple phases with distinct space groups often lead to isolated signatures in the PDF, analysis of complex materials results in highly overlapped features that are rich in structural information. Without advanced modeling of the complex structures, extracting meaningful information is very difficult. Once the model is developed, the reverse procedure can be applied, whereby material properties are predicted from the PDFs. This could be of particular use for lithiated/de-lithiated anodes, as the manner in which the material has evolved through charging/discharging can be better understood from the PDF. At the simplest level of modeling, neighbor-bonding distances can predict the sharp intraplanar peaks at short distances within the PDF. However, analytical models corresponding to amorphous and mesoscopic structure are not so easily developed, as these factors are emergent phenomena that arise from the complex interplay of many simpler atomic interactions.

In this work, a model is developed through the use of molecular dynamics (MD). This procedure simulates the atomic interactions among the crystalline and amorphous domains of the composite systems and reveals both nanoscale and mesoscale phenomena. The properties of interest in these carbon composite systems are those that cannot be easily obtained through experiment, but whose understanding will lead to the development of better anode materials. These properties include the d-spacing between carbon layers (graphene) within the nanocrystallites, the nature of how these nanocrystallites distribute and deform with the amorphous carbon matrix, and the nature of lithium ion storage/transport within this anode material. The first two properties are addressed within this article, which focuses exclusively on uncharged anode materials. The last property is to be addressed in a forthcoming contribution, addressing charged and discharged materials.

3.2 METHODS FOR SIMULATION AND EXPERIMENT

3.2.1 *SYNTHESIS*

The carbon materials with nanoscale structure were synthesized from solvent extracted hardwood lignin. Lignin is a highly cross-linked polyphenolic polymer without repeating units that yields 40 to 60 wt % char after pyrolysis [4, 5]. Conversion of lignin into nanoscale graphitic material consists of oxidative stabilization to 250 °C in flowing air followed by pyrolysis under inert atmospheres. The scale of the crystalline domains is a result of systematically varying the annealing temperatures (1000, 1500, and 2000 °C).

3.2.2 *STRUCTURAL CHARACTERIZATION*

The experimentally obtainable parameters describing these three carbon structures include estimates of the overall composite density, the volume fraction of crystalline material, and the size of the crystallites. The volume fraction was determined through the use of transmission electron microscopy, and crystallite diameter was obtained through Scherrer analysis of X-ray diffraction measurements obtained using a PANalytical X'Pert Pro MPD diffractometer with Cu K α 1 radiation [3].

3.2.3 *NEUTRON SCATTERING*

The neutron scattering experiments were carried out at the Nanoscale-Ordered Materials Diffractometer (NOMAD) at the Spallation Neutron Source at Oak Ridge National Laboratory [54]. Three samples (~150 mg each) were measured in 3 mm quartz capillaries at room temperature for a total of 2 hours. The measurements were performed in an argon atmosphere to reduce scattering from the air. In order to

obtain the structure factor $S(Q)$, the background was subtracted and the data was normalized by the scattering from the solid vanadium rod. The experimental PDFs were obtained by a Fourier transform of $S(Q)$ using $Q_{\text{MAX}} = 30 \text{ \AA}^{-1}$ for all samples.

3.2.4 SIMULATION

The structural model for the crystallites was the same as that used for simulation of isolated nanocrystallites (spherical particles containing 3 to 9 layers of graphene) [58], in which spherical particles of fixed radius were extracted from bulk graphite. The placement of these crystallites within a periodic simulation volume was performed using a genetic algorithm designed to maximize the distance between crystallites. The orientation of each crystallite was randomly chosen, and the placement of crystallites did not fall into a regular lattice of close-packed structure. This algorithm was a three-dimensional extension of those used in digital half-toning to achieve an unordered two-dimensional arrangement of dots [59]. For volume fractions of crystalline material higher than the maximal random close packing of 64% [60], a Voronoi decomposition of the existing crystallite locations was performed using Zeo++ [61] to determine the largest empty sphere in the system, whereupon a crystallite was centered and then truncated to avoid overlap with other crystallites. This procedure was repeated until the desired volume fraction of crystalline material was attained. It is likely that the experimental materials contain a distribution of crystallite sizes and shapes – the distribution being a complex function of pyrolysis temperature; however, for modeling purposes all crystallites within each system were approximated as uniform, except where truncated as noted. The use of the experimentally determined mean crystallite size within the simulated counterparts combined with the fact that the experimental crystallite size distribution is narrow implies this uniformity is an approximation that should contribute little error to the qualitative characteristics of the resulting PDFs. The model for amorphous carbon consisted of random placement of graphene layers within the simulation volume in a fashion such that there were no overlapping carbon atoms. Where overlap existed between a placed sheet and crystallites and/or other sheets, atoms were removed from the newly placed sheet until there was no atomic overlap. This procedure provides an initial composite structure with uniform crystallites oriented randomly and arranged without long-range order, and an amorphous phase oriented randomly and composed of irregularly shaped graphene planes filling to a variable degree the volume between crystallites. These models were made to match experimental materials by (1) directly specifying the crystallite size, (2) adding crystallites until the specified crystalline volume fraction was met, and (3) adding amorphous material until the specified composite density was achieved.

The generated systems ranged from 70,000 to 550,000 C atoms. The simulation volumes were cubic in shape with sides ranging from 100 to 200 Å. These generated systems were then minimized and equilibrated using the molecular dynamics software LAMMPS [42]. The OPLS-AA potential was used [43]. The total interactions included bond stretching, angle bending, bond torsion, and non-bonded interactions for atoms separated by three or more bonds. The non-bonded interactions were characterized using the Lennard-Jones potential. The parameters for this potential, along with those for the stretching and bending modes, were taken from the work of Tsai and Tu [25] on graphite. The torsion potential was taken from the work of Fileti, Dalpian [44] on graphene.

The composite systems were equilibrated in the canonical (NVT) ensemble for 2 ns using the r-RESPA algorithm developed by Tuckerman, Martyna [46] to integrate the equations of motion. A resolution of 2 fs was used for the non-bonded interactions along with a resolution of 0.2 fs for the bonded interactions. The Lennard-Jones cut-off distance was 12 Å. The simulation temperature was 298 K. This temperature was regulated using a Nosé-Hoover thermostat [57, 62, 63].

The pair distribution functions for the equilibrated structures were obtained by time-averaging the instantaneous pair distribution functions for the last 2 ps of simulation time. The simulated PDFs are obtained through direct summing of pairs; consequently there is no Fourier transforming of the data and therefore no introduction of numerical artifacts due to that data processing step [64].

3.3 RESULTS AND DISCUSSION

In order to develop a relationship between the experimentally measurable properties and the pair distribution functions, a set of composite systems was generated that varied each of three properties—nanocrystallite radius, crystalline volume fraction, and composite density—independently. Experimentally, these three properties are correlated and cannot be independently manipulated. Three of the fifteen simulated models are intended to correspond to experimentally synthesized materials. The purpose of the other twelve models is to isolate the effect of each parameter on the PDF. The fifteen composite systems are described in **Table 3.1**.

Table 3.1. The upper limit of the volume fraction varied, since it is not possible to simultaneously obtain a specified low composite density and high crystalline volume fraction. An asterisk denotes experimentally synthesized materials.

Crystallite Radius (Å)	Composite Density (g/cm³)	Crystalline Volume Fraction
$r = 5$	$\rho = 1.94$	$\Phi_c = 0.1, 0.5, 0.9^*$
$r = 7$	$\rho = 1.94$	$\Phi_c = 0.1, 0.5, 0.9$
$r = 7$	$\rho = 1.51$	$\Phi_c = 0.1, 0.5^*, 0.75$
$r = 7$	$\rho = 1.38$	$\Phi_c = 0.1, 0.5, 0.7$
$r = 17$	$\rho = 1.38$	$\Phi_c = 0.1^*, 0.5, 0.6$

3.3.1 DIRECT MEASUREMENT OF D-SPACING

With regard to the behavior of the PDF in the region that contains the d-spacing, a clear relation between the nature of the curve in this region and the d-spacing width must be understood. This d-spacing distance was directly calculated for the crystallites within the equilibrated composite systems using the same procedure as McNutt, Wang [58]. Only crystallites that remained intact through the process of equilibration were considered for this measurement. In our simulations, 50% to 95% of the crystallite layers remained localized, as can be confirmed in **Figure 3.1**, where similarities in the initial and equilibrated structures can be visually observed, indicating little relaxation. The determination of a given pair of planes remaining adjacent was performed by examining the distribution of d-spacings and including only those pairs that fell within the central Gaussian-like peak (not shown).

The importance of the d-spacing measurements is to characterize not the exact values of d-spacing, but rather the trends in d-spacing *changes* as parameters vary so that the same trends can be understood for the experimental composites. Two geometric measures of d-spacing between adjacent planes in a crystallite were considered: breathing distance and center-of-mass (COM) distance, as previously used [58]. The COM distance is defined to be the length of the vector from the center of mass of one plane to the center of mass of the other plane (this vector is referred to as the COM vector). The projection of each plane's normal vector onto the COM vector is calculated, and of these two projected vectors, the one with minimum length is defined as the breathing distance. It is noted that the COM distance includes both breathing and any lateral sliding between planes and always gives a greater absolute value than the breathing distance. The results of these measurements are summarized in **Table 3.2**. By having multiple configurations of composite systems for each isolated parameter change, any correlated effects between parameters can also be determined.

As we examine PDFs for signs of d-spacing, **Table 3.2** will be referenced in each of the following three subsections, exploring the impact of crystallite radius, composite density, and crystalline volume fraction. Here we point out the changes in d-spacing from direct (geometrical) measurement. First, when crystallite size and composite density are held constant, an increase in crystalline volume fraction corresponds to a decrease in COM d-spacing (9 out of 10 comparisons in **Table 3.2**) and almost no effect on breathing distance. Thus, an increase in crystalline volume fraction not surprisingly restricts lateral motion of the planes within a crystallite.

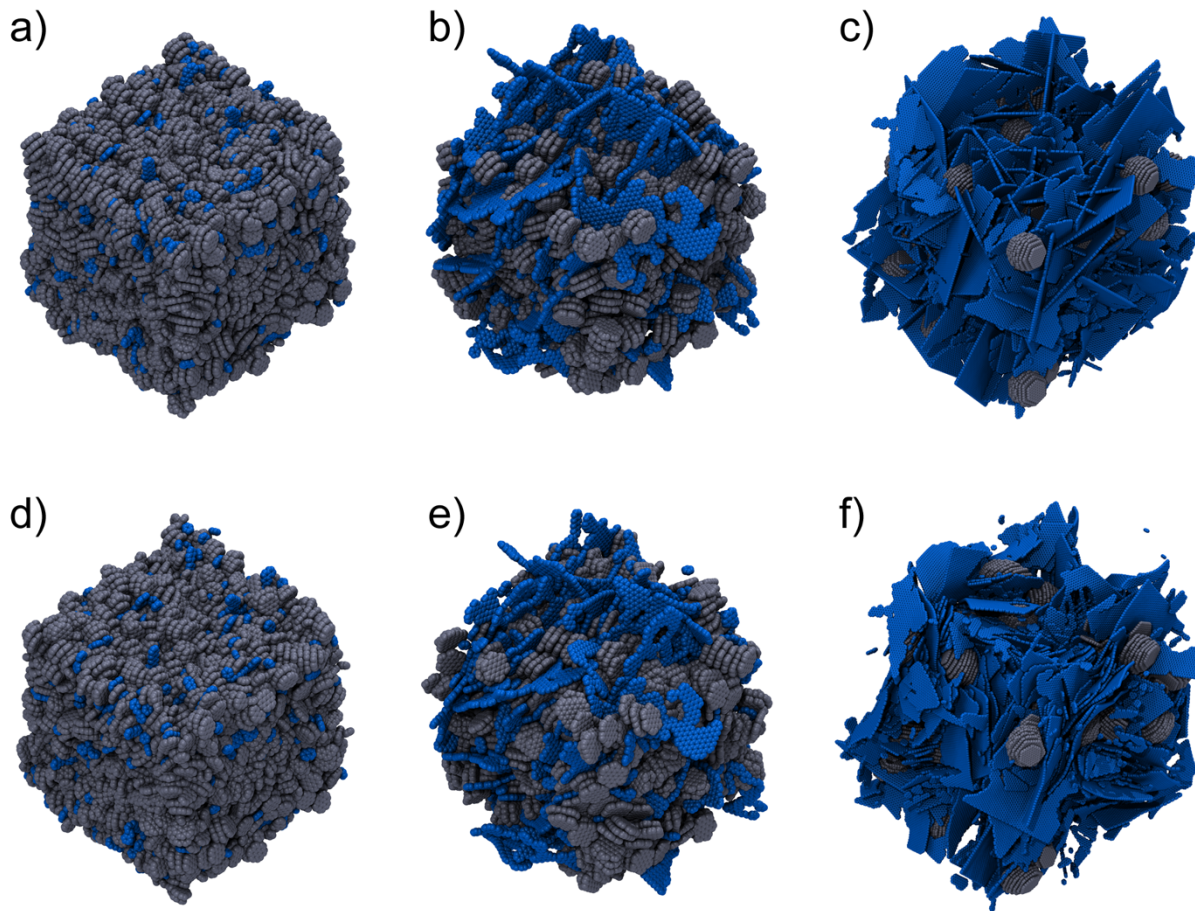


Figure 3.1. Molecular representation of three composite systems before equilibration (top row) and after (bottom row): (a) & (d) $r = 5 \text{ \AA}$, $\rho = 1.94 \text{ g/cm}^3$, $\Phi_c = 0.9$; (b) & (e) $r = 7 \text{ \AA}$, $\rho = 1.51 \text{ g/cm}^3$, $\Phi_c = 0.5$; (c) & (f) $r = 17 \text{ \AA}$, $\rho = 1.38 \text{ g/cm}^3$, $\Phi_c = 0.1$.

Table 3.2. Effect of changing one property of a composite material on d-spacing (two types: breathing distance and center-of-mass distance).

Constant	Changed prop.	Changed values	Breathing distance (Å)	COM distance (Å)
$\rho = 1.38, \Phi_c = 0.1$	Radius (Å)	$7 \rightarrow 17$	$3.41 \rightarrow 3.38$	$5.09 \rightarrow 4.18$
$\rho = 1.38, \Phi_c = 0.5$		$7 \rightarrow 17$	$3.40 \rightarrow 3.39$	$4.12 \rightarrow 4.03$
$\rho = 1.94, \Phi_c = 0.1$		$5 \rightarrow 7$	$2.90 \rightarrow 2.97$	$3.77 \rightarrow 3.70$
$\rho = 1.94, \Phi_c = 0.5$		$5 \rightarrow 7$	$2.89 \rightarrow 2.94$	$3.61 \rightarrow 3.55$
$\rho = 1.94, \Phi_c = 0.9$		$5 \rightarrow 7$	$2.90 \rightarrow 2.94$	$3.55 \rightarrow 3.63$
$r = 7, \Phi_c = 0.1$	Density (g/cm ³)	$1.38 \rightarrow 1.51 \rightarrow 1.94$	$3.41 \rightarrow 3.34 \rightarrow 2.97$	$5.09 \rightarrow 5.03 \rightarrow 3.70$
$r = 7, \Phi_c = 0.5$		$1.38 \rightarrow 1.51 \rightarrow 1.94$	$3.40 \rightarrow 3.31 \rightarrow 2.94$	$4.12 \rightarrow 4.20 \rightarrow 3.55$
$r = 5, \rho = 1.94$	Volume fraction	$0.1 \rightarrow 0.5 \rightarrow 0.9$	$2.90 \rightarrow 2.89 \rightarrow 2.90$	$3.77 \rightarrow 3.61 \rightarrow 3.55$
$r = 7, \rho = 1.38$		$0.1 \rightarrow 0.5 \rightarrow 0.7$	$3.41 \rightarrow 3.40 \rightarrow 3.45$	$5.09 \rightarrow 4.12 \rightarrow 3.90$
$r = 7, \rho = 1.51$		$0.1 \rightarrow 0.5 \rightarrow 0.75$	$3.34 \rightarrow 3.31 \rightarrow 3.36$	$5.03 \rightarrow 4.20 \rightarrow 4.08$
$r = 7, \rho = 1.94$		$0.1 \rightarrow 0.5 \rightarrow 0.9$	$2.97 \rightarrow 2.94 \rightarrow 2.94$	$3.70 \rightarrow 3.55 \rightarrow 3.63$
$r = 17, \rho = 1.38$		$0.1 \rightarrow 0.5 \rightarrow 0.6$	$3.38 \rightarrow 3.39 \rightarrow 3.39$	$4.18 \rightarrow 4.03 \rightarrow 3.89$

Second, when crystallite size and crystalline volume fraction are held constant, an increase in composite density corresponds to a decrease in both the breathing and COM d-spacing (7 of 8 cases). As the density increases, the mobility of planes within a crystallite in both normal and lateral directions is restricted.

Third, when composite density and crystalline volume fraction are held constant, an increase in crystallite size corresponds to more complex behavior in d-spacing, with a correlation between crystallite size and both composite density and crystalline volume fraction. From an analysis of simulated, isolated nanocrystallites (in vacuum) [58], we expect d-spacing to decrease with increasing crystallite size, based on entropic arguments. As shown in **Table 3.2**, when the total density and crystalline volume fraction are held constant and crystallite radius is varied, this intuitive trend between size and d-spacing is observed in four of the five cases for the COM distance but only two of the five cases for the breathing distance. It is apparent that the effect of crystallite radius on the change in d-spacing is more complicated in the composite than in the isolated crystallites. At low density ($\rho = 1.38 \text{ g/cm}^3$) – a situation closest to the isolated crystallite – both the breathing distance and the COM distance decrease, corresponding to the results from the isolated crystallites. However, at high density ($\rho = 1.94 \text{ g/cm}^3$) and low to intermediate crystalline volume fractions ($\Phi_c = 0.1$ & 0.5), when the crystallite size increases, the breathing distance increases (representing more compaction in the smaller crystallites) while the COM distance decreases (representing more lateral sliding in the smaller crystallites). Finally, at high density and high crystalline volume fraction ($\Phi_c = 0.9$), when the crystallite size increases, both the breathing and COM distance increase (representing more compaction and less sliding in the smaller crystallites). This last observation alone is most likely an artifact of the necessary addition of “truncated” crystallites to the systems with high crystalline volume fractions (see the “methods” section). As these high density systems exhibit significant internal pressure, truncated crystallites with smaller or non-circular planes will more easily compact together than larger ones. These are the only two systems that exhibit this anomalous d-spacing trend, and they are also the only two systems that contain truncated crystallites.

3.3.2 PAIR DISTRIBUTION FUNCTIONS

Two forms of the pair distribution functions, $g(r)$ and $G(r)$ are presented. The first is the PDF itself, $g(r)$, which is calculated in the simulation as the ensemble average of the ratio of the local density distribution, $\rho(r)$, to the average bulk density, ρ [64],

$$g(r) = \frac{\rho(r)}{\rho} = \frac{1}{\rho} \frac{1}{N} \left(\sum_i \sum_{j \neq i} \delta(r - r_{ij}) \right)$$

This form of the PDF emphasizes the local structure of amorphous materials and liquids at low r . It is also the Fourier transform of the structure factor $S(Q)$, a function experimentally obtained from neutron scattering. The second common form of the PDF, $G(r)$, sometimes called the density-density correlation function (DDCF) [56, 65], is defined as

$$G(r) \equiv (g(r) - 1) r^2$$

The DDCF is better suited for the crystalline materials and nanoparticles with medium- and long-range order. Since in our samples we have a combination of amorphous and crystalline counterparts, we will present both functions for ease of visualization.

Because the information describing the simulated composite systems is available at the atomic level, the PDFs for these systems can be decomposed into component functions that sum to the total PDF. This permits a deeper understanding of the origin of specific traits of the PDFs. These component functions are described in **Table 3.3**.

The attributes of the PDFs that are of particular interest for the composite systems include: 1) the magnitude of intraplanar peaks, 2) the distance to which these intraplanar peaks extend, 3) the behavior of the PDF in the d-spacing region ($\sim 3 - 4$ Å), and 4) the unique long-range order in these composite systems which is manifest in the form of oscillations in the PDF.

In **Figure 3.2**, we present a simulated PDF in three formats for one of the materials ($r = 7$ Å, $\rho = 1.51$ g/cm³, and $\Phi_c = 0.5$). In **Figure 3.2(a)**, a plot of $g(r)$ is shown, in which the short-range features of the PDF are most clearly visible. In **Figure 3.2(b)**, a decomposition of $g(r)$ is shown, in which the contributions to the total PDF are evident. In **Figure 3.2(c)**, a plot of $G(r)$ is shown, in which the long-range features (up to 50 Å) are most clearly visible. Several observations are immediately apparent from **Figure 3.2**. From the decomposition, it is clear that the sharp peaks that appear in the PDF arise from two contributions: (i) intraplanar interactions within a layer of a nanocrystallite and (ii) an amorphous-amorphous (A-A) component, which includes both intraplanar and interplanar interactions. The peak at 1.42 Å corresponds to the C-C bond distance, the peak at 2.45 Å to carbon atoms separated by two bonds, and the peak at 2.83 Å to carbon atoms separated by three bonds. Note that there is no peak at 2.30 Å – the distance corresponding to the diagonal of a 5-membered carbon ring. This peak is absent in both the experimental data and our simulated data, indicating the systems do not contain 5-membered rings.

Table 3.3. Description of component functions for pair distribution functions.

Component Function Name	Description
Total = A-A + A-C + C-C	Total pair distribution function
A-A	Only amorphous-amorphous (A-A) pairs of carbon atoms
A-C	Only amorphous-crystalline (A-C) pairs of carbon atoms
C-C = Inter-C + Inter-P + Intra-P	Only crystalline-crystalline (C-C) pairs of carbon atoms
Inter-crystallite (Inter-C)	Pairs of carbon atoms between different crystallites
Inter-plane (Inter-P)	Pairs of carbon atoms within the same crystallite but different planes
Intra-plane (Intra-P)	Pairs of carbon atoms within the same crystallite and the same plane

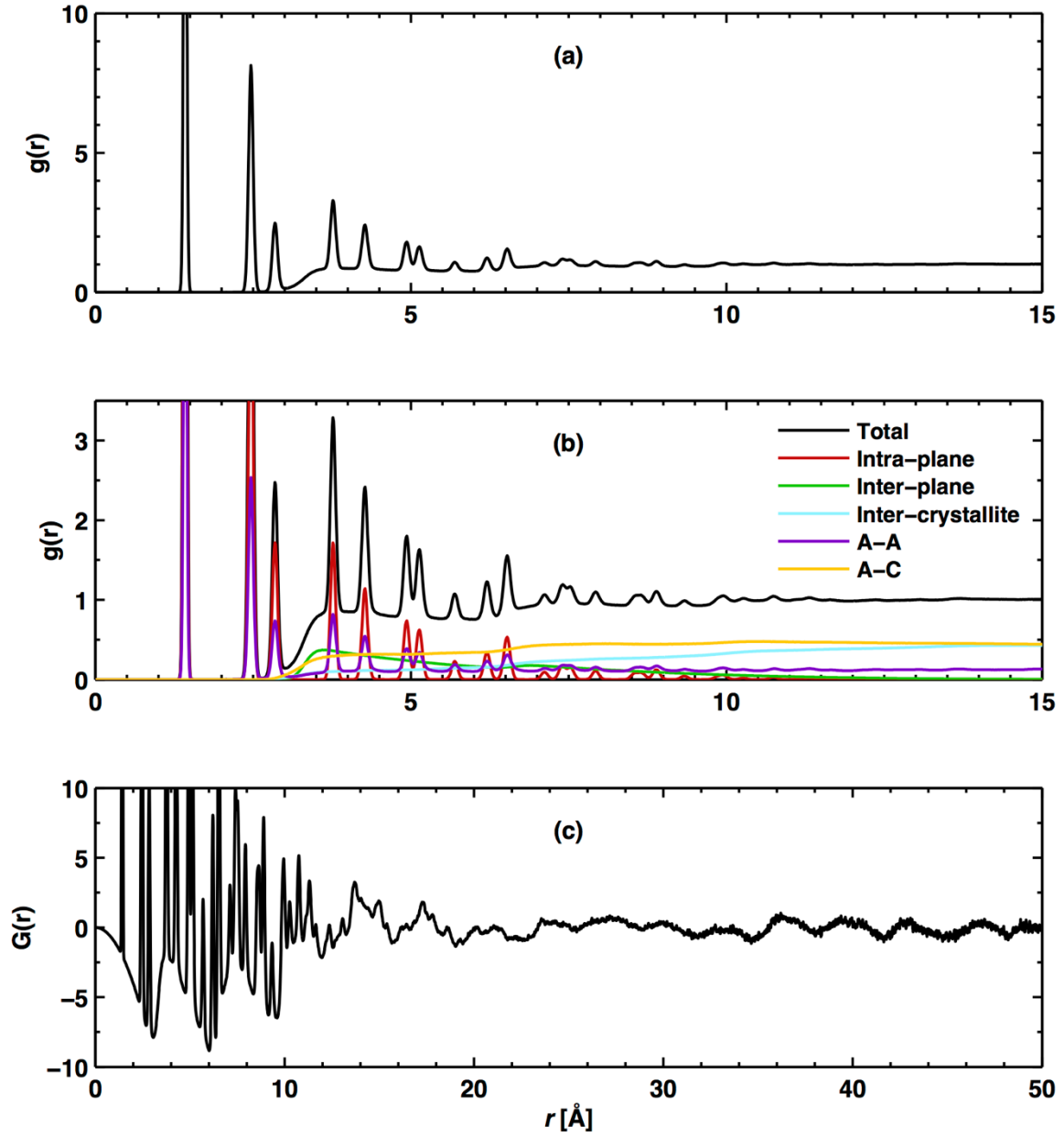


Figure 3.2. Simulated PDFs ($r = 7$ Å, $\rho = 1.51$ g/cm³, $\Phi_c = 0.5$) in three formats: (a) $g(r)$ to reveal short-range features, (b) decomposition of $g(r)$ into component functions, (c) $G(r)$ to reveal long-range features.

The component of the PDF due to interplanar interactions within a single nanocrystallite should directly capture d-spacing. At low temperature in a well-ordered crystallite (such as was captured in our initial configurations in **Figure 3.1(a)**, (b) and (c)), these peaks are well-defined. The peaks at 3.40 Å and 3.68 Å in **Figure 3.3(a)** correspond to C atoms in adjacent layers in nanocrystallites at 0 K. In the equilibrated structure at room temperature, as shown in **Figure 3.3(b)**, the interplanar peaks have broadened and appear in the total PDF as a contribution to the baseline. (In the materials with a crystallite radius of 7 Å as shown in **Figure 3.2**, there are only three layers and thus only two broad intracrystallite, interplanar peaks, with the second one barely visible to the eye in **Figure 3.2(b)** at 7.0 Å.) The analysis of the equilibrated structure at room temperature rather than at lower temperatures is performed because the batteries (nominally) operate at room temperature, and thus the development of the structure/property relationship between d-spacing width and lithium ion intercalation should be understood at these temperatures.

The intercrystallite and amorphous-crystalline (A-C) components of the PDF shown in **Figure 3.2(b)** monotonically increase with distance, showing plateaus. The structure of these components reflects the distribution of crystallites and the morphology of the amorphous domain. These components represent interfacial boundaries and, as a unique aspect of the composite carbon material, are not present in the PDF of bulk graphite. In **Figure 3.2(c)**, $G(r)$ reveals features at longer distances that are hardly visible in $g(r)$. The origin of these oscillations and the meaning of their frequency and amplitude are discussed below. Having provided an overview of the information content present in these PDFs, we now examine the effect of crystallite radius, composite density and crystalline volume fraction individually.

3.3.2.1 Effect of crystallite radius on the pair distribution functions

In **Figure 3.4**, simulated PDFs with their decompositions are shown for two materials with the same composite density ($\rho = 1.38 \text{ g/cm}^3$) and volume fraction ($\Phi_c = 0.5$) and different crystallite radii ($r = 7 \text{ Å}$ and 17 Å). Effects in the d-spacing region ($\sim 3\text{-}4 \text{ Å}$) can most easily be observed between the third and fourth peak in the PDF. This region includes the initial rise of the intracrystallite interplanar component, which captures d-spacing. Very subtle differences in the d-spacing are observed in the total PDF. Direct extraction of the d-spacing from visual inspection of this region in the total spectra is difficult. This is not altogether surprising since the effects of crystallite radius on d-spacing seen in **Table 3.2** are fairly small – the difference in breathing distance as a function of crystallite radius is on the order of fractions of an Angstrom.

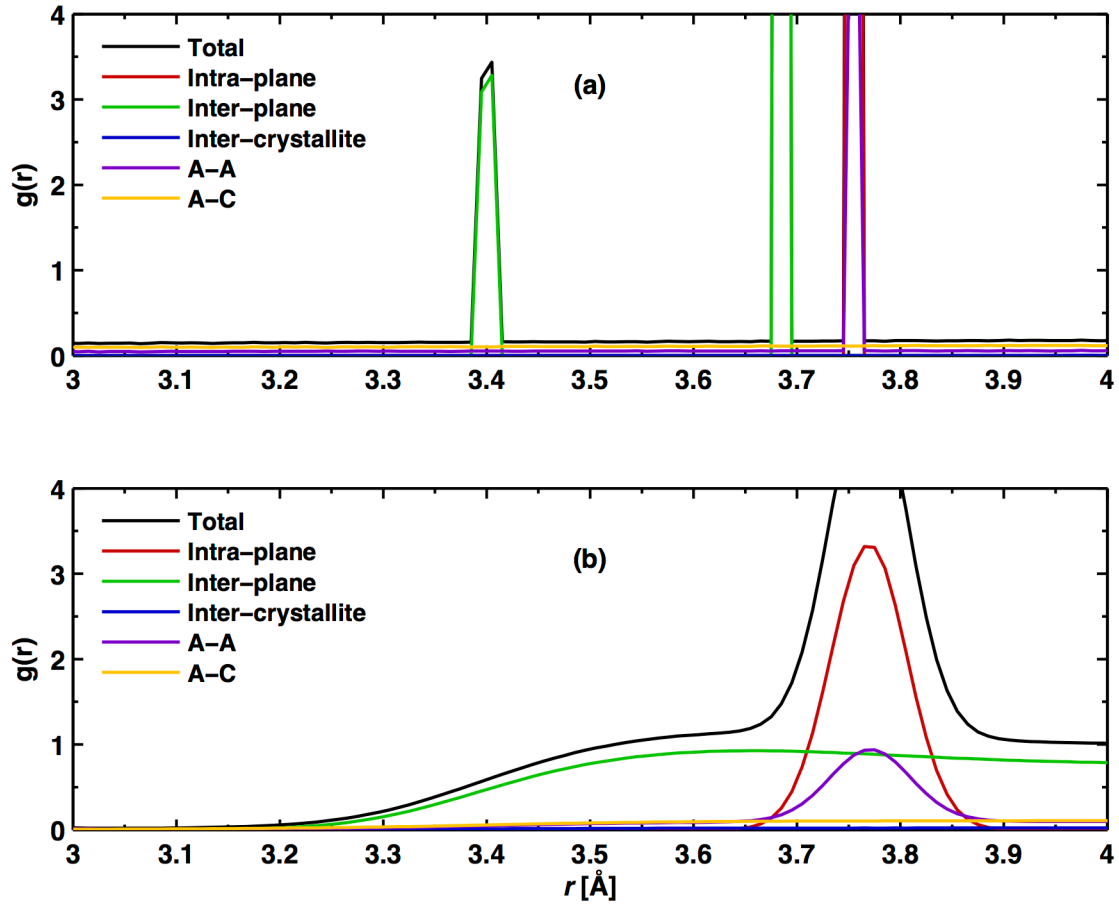


Figure 3.3. Simulated PDFs ($r = 17$ Å, $\rho = 1.38$ g/cm³, $\Phi_c = 0.5$) showing the d-spacing region for the initial composite system (a) and the equilibrated composite system (b).

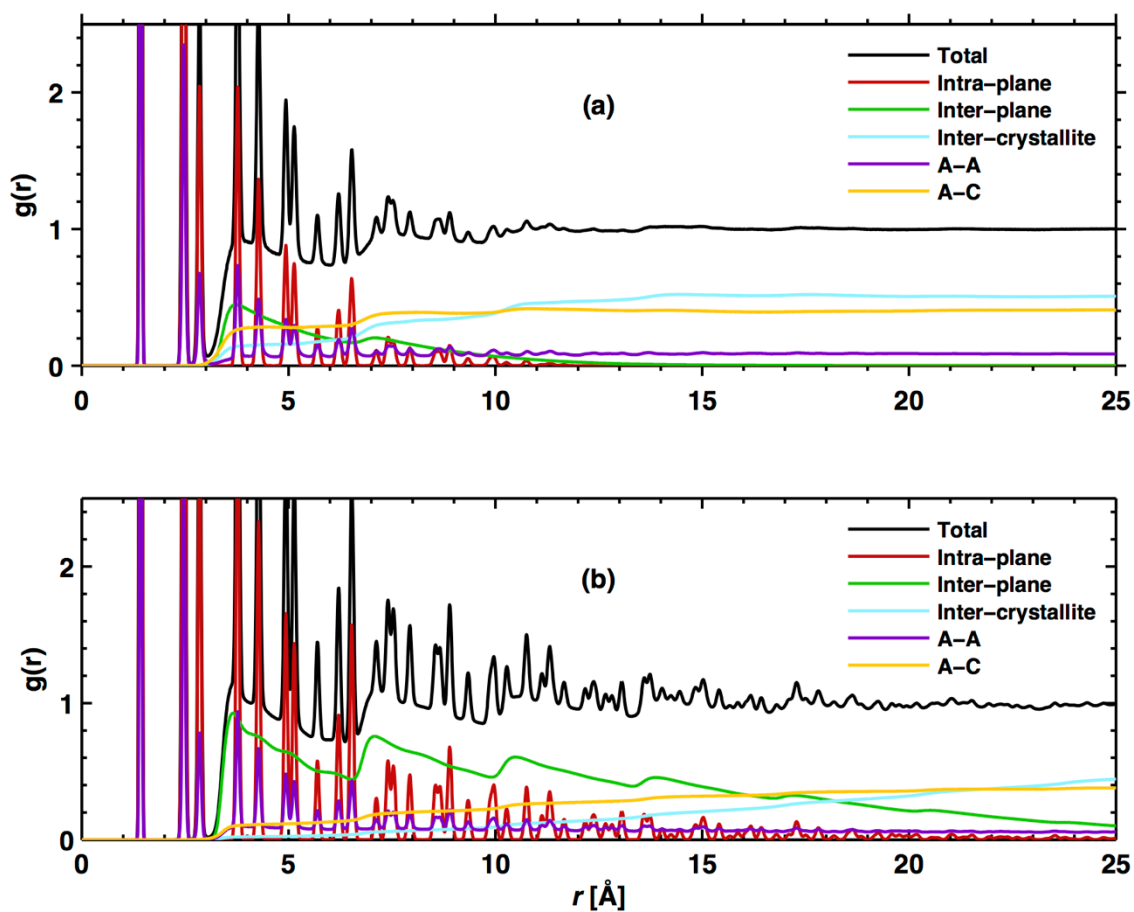


Figure 3.4. Simulated PDFs with decomposition for two materials with common density and crystalline volume fraction. ($\rho = 1.38 \text{ g/cm}^3$, $\Phi_c = 0.5$). (a) smaller crystallites ($r = 7$ Å) and (b) larger crystallites ($r = 17$ Å).

Moreover, there are significant changes in the amorphous-crystalline component and, to a lesser extent, the intercrystallite component in this same range. It is worth noting that the intracrystallite interplanar component shows additional peaks for the composite with larger crystallites, indicating separations for layers separated by integer numbers of planes.

The magnitude of the intraplanar peaks and the distance to which they extend is a feature in the PDF that has been correlated to particle size through an “envelope function” [66]. One can naively apply this approach to these composite materials. As shown in **Figure 3.5**, the magnitudes of the peaks are larger and extend farther out for the larger nanocrystallites, when the composite density and crystalline volume fraction are held constant. However, in the real materials, a change in pyrolysis temperature results in a change in all three parameters – crystallite size, composite density and crystalline volume fraction. Additionally, we have already noted that the observed peaks have two contributions, those due to intraplanar pairs in the crystalline and amorphous domains. Therefore, this simple rule may fail in the analysis of real materials. This effect is discussed in greater detail in the section on changes in the PDF due to crystalline volume fraction.

There is discussion in the literature regarding the interpretation of oscillations in long-range data. Below the characteristic nanoparticle domain size, ξ , there are sharp peaks due to intramolecular structure, while beyond ξ there are only broad intermolecular features, or crystallite-crystallite correlations [67].

In the simulations there are no equipment effects or artifacts, or sample inhomogeneity. Moreover, in the simulation, the PDFs are measured directly; thus there are no artifacts due to any numerical Fourier transform procedure. Thus, every feature in the PDF, including long-range oscillations, can only arise due to the structure. Additionally, these long-range oscillations cannot arise due to spurious effects of the finite size of the simulation volumes. The simulations were cubic in shape with sides ranging from 100 to 200 Å. The PDF is evaluated only to 50 Å, which is always smaller than the half the box length, thus avoiding any artificial features due to periodic boundary conditions.

In **Figure 3.6** we observe that there is a correlated effect involving both crystallite radius and the crystalline volume fraction on the long-range oscillations. At low crystalline volume fractions, there are no long-range oscillations. However, as the crystalline volume fractions increase, two forms of long-range oscillation appear.

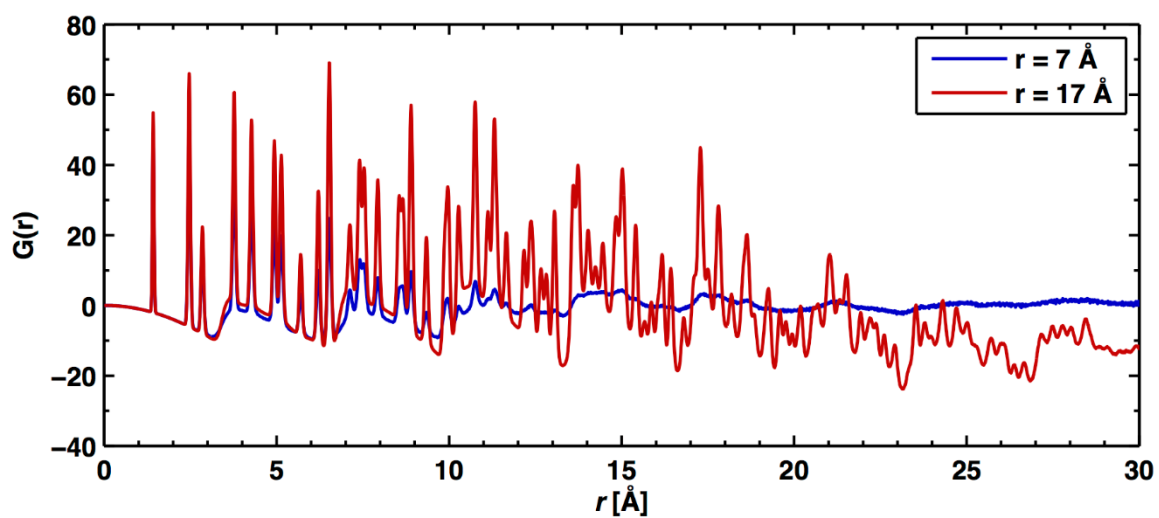


Figure 3.5. Simulated DDCFs for two materials with common density and crystalline volume fraction ($\rho = 1.38 \text{ g/cm}^3$, $\Phi_c = 0.5$) and varying crystallite size.

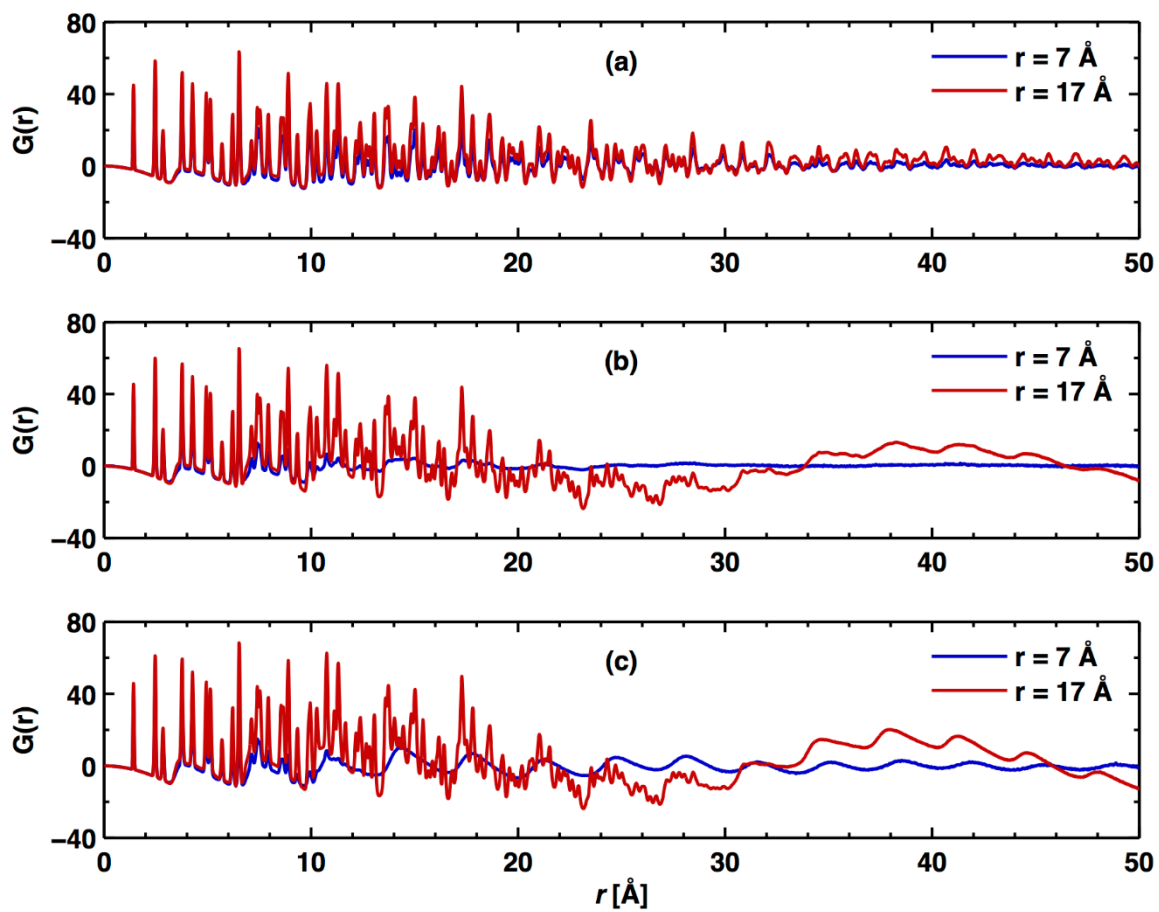


Figure 3.6. Simulated DDCFs for materials with common density ($\rho = 1.38 \text{ g/cm}^3$) at two crystallite radii and three crystalline volume fractions: (a) low $\Phi_c = 0.1$, (b) medium $\Phi_c = 0.5$, (c) high $\Phi_c = 0.7/0.6$.

There is a high frequency (wavelength of nominally 3 Å) mode and a low frequency (wavelength of nominally 20 Å) mode that emerge. For the systems studied herein, the high frequency mode is observed in the large crystallite material at intermediate crystalline volume fraction and in both materials at high crystalline volume fraction. The low frequency mode is only observed in the material with large crystallites. To understand the origin of these oscillations, the decomposition of $G(r)$ was performed for the highest crystalline volume fraction systems corresponding to $r = 7$ Å and $r = 17$ Å in **Figure 3.7**. From the plot, it is seen that long-range oscillations are primarily due to intercrystallite pairs of carbon atoms. In the material with larger crystallites, this intercrystallite component is responsible for both the high and low frequency modes. It is important to note that these long-range oscillations appear only in model systems containing both large crystalline domains and intermediate to high volume fractions of crystalline material. As none of our experimental systems possess this combination of parameters, these unique features of the simulated PDFs are unavailable for experimental comparison.

3.3.2.2 Effect of density on the pair distribution function

From **Table 3.2**, it is evident that composite density has by far the greatest effect of any of the experimental properties on d-spacing. Higher density systems have much smaller d-spacings, measured as either breathing or COM distances. This observation is corroborated in **Figure 3.8**, where it is seen that as composite density increases, the broad peak of the d-spacing curve shifts toward smaller distances. At the same time, it increases in magnitude. In this case, the increase in magnitude is primarily due to the amorphous-amorphous component of the PDF as revealed in the decomposition (not shown), which is reasonable given that the means by which the composite density increases when crystalline volume fraction is held constant is through the addition of amorphous components.

The effect of density on the intraplanar peaks is also seen in $g(r)$ in **Figure 3.8** and in $G(r)$ in **Figure 3.9**. The magnitude of these peaks decreases with increasing density. However, the distance to which these peaks reach remains about the same. Because the crystalline volume fraction is low in **Figure 3.9** ($r = 7$ Å, $\Phi_c = 0.1$), we do not observe any low or high frequency long-range oscillations. This is consistent with **Figure 3.6**, where the difference in scales on the y-axis is noted.

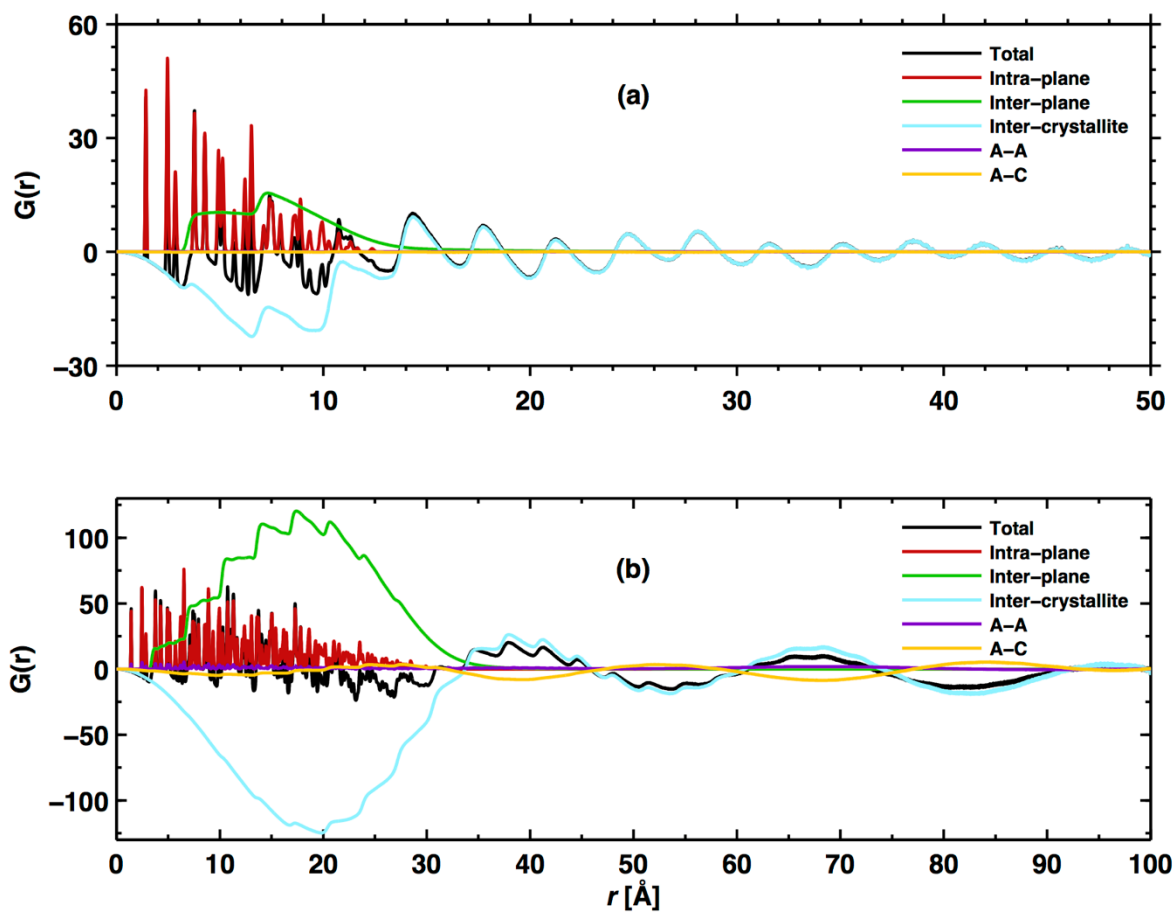


Figure 3.7. Simulated DDCFs with decomposition for two materials with common density and high crystalline volume fraction ($\rho = 1.38 \text{ g/cm}^3$, $\Phi_c = 0.7/0.6$). (a) smaller crystallites ($r = 7 \text{ Å}$) and (b) larger crystallites ($r = 17 \text{ Å}$).

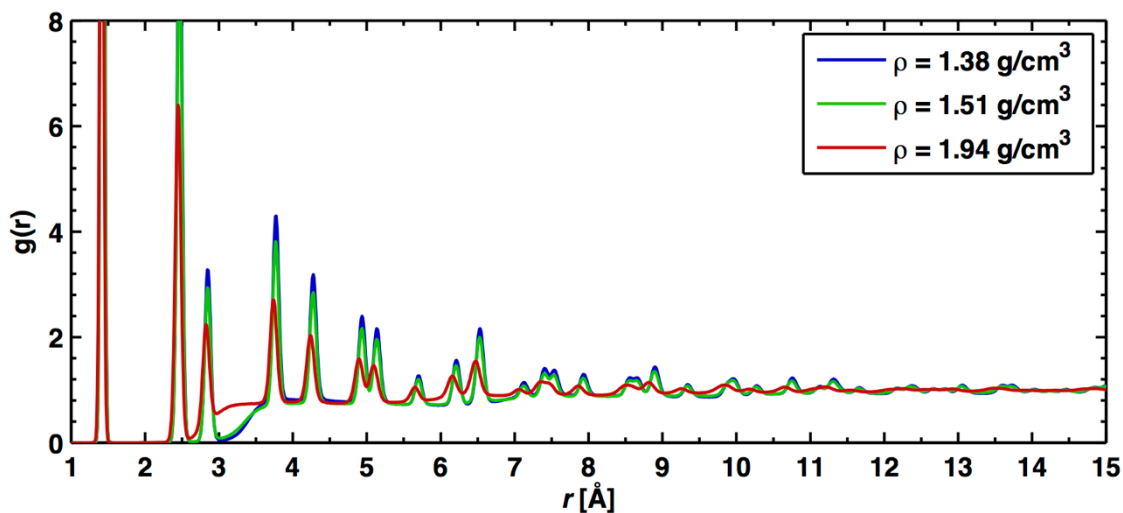


Figure 3.8. Simulated short-range PDFs for materials with common crystallite size and crystalline volume fraction ($r = 7 \text{ \AA}$, $\Phi_c = 0.1$) and varying density.

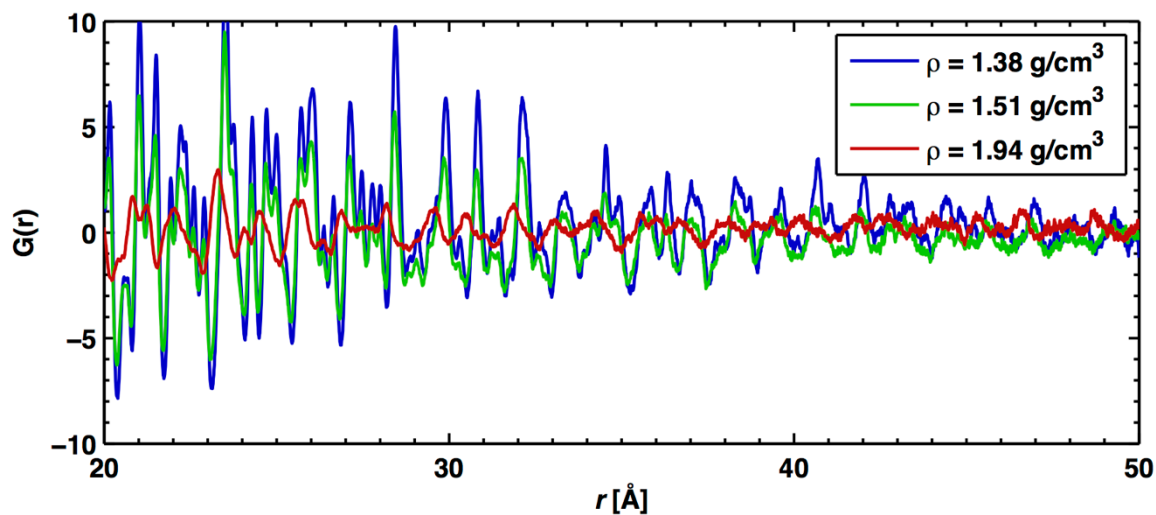


Figure 3.9. Simulated long-range DDCFs for materials with common crystallite size and crystalline volume fraction ($r = 7 \text{ \AA}$, $\Phi_c = 0.1$) and varying density.

3.3.2.3 Comparison of simulated and experimental pair distribution functions

In this section, the experimental and simulated PDFs are compared. In **Figure 3.10(a)**, three simulated PDFs are plotted, corresponding to the three models constructed according to the experimentally determined combinations of crystallite size, composite density and crystalline volume fraction resulting from three different pyrolysis temperatures. The scaled experimental PDF is plotted in **Figure 3.10(b)**.

From comparison of **Figure 3.10(a)** with **Figure 3.10(b)**, it is seen that all peaks present in the experimental spectra are reproduced in the simulated spectra. This is also evident in **Table 3.4**. Small (0.02 Å) discrepancies in these peak locations are likely within the level of uncertainty associated with the interaction potential for bond stretching. The relative magnitudes of the peaks with respect to pyrolysis temperature are reproduced in the simulated spectra. Namely, the magnitudes of the peaks increase with increasing pyrolysis temperature.

The absolute magnitudes of the peaks are not the same in the simulated and experimental PDFs. The simulation is performed at the same temperature as the experiment (298 K), eliminating temperature as a source of the discrepancy. Presumably, the interaction potentials used in the simulation are slightly too stiff, resulting in sharper peaks. At the same time, experimental PDF peaks are broadened due to the instrument resolution, correlated atomic motion, finite QMAX used in the Fourier transform and the size distribution of nanocrystallites [68-71]. These effects were omitted in the simulations. Comparing peak heights, however, is not the best measure of comparison. It is preferable to compare the integral of the peaks to understand the number of neighbors in each shell. Since the first peak corresponds to the C-C bond distance, the integral should be 3 in bulk graphite. In these composite materials, the integral will be less than 3, since there are C atoms at the edges of the nanocrystallites and at the edges of amorphous planes that are only bound to 2 other C atoms. Numerical integration of the first peak in the simulated materials yields an average number of C neighbors of 2.45, 2.57, and 2.79 for the materials with crystallite radii of 5 Å, 7 Å and 17 Å respectively. That the average number of bonds decreases with decreasing crystallite size is to be expected since surface area to volume ratio of the crystallite increases and thus the number of C atoms at the edges increases.

In **Figure 3.10(b)** the experimental data is scaled by a constant so that the integrals of the first peak match those of simulation. The scaling only serves to enhance the agreement between simulation and experiment as it accentuates the differences in peak heights between the three materials.

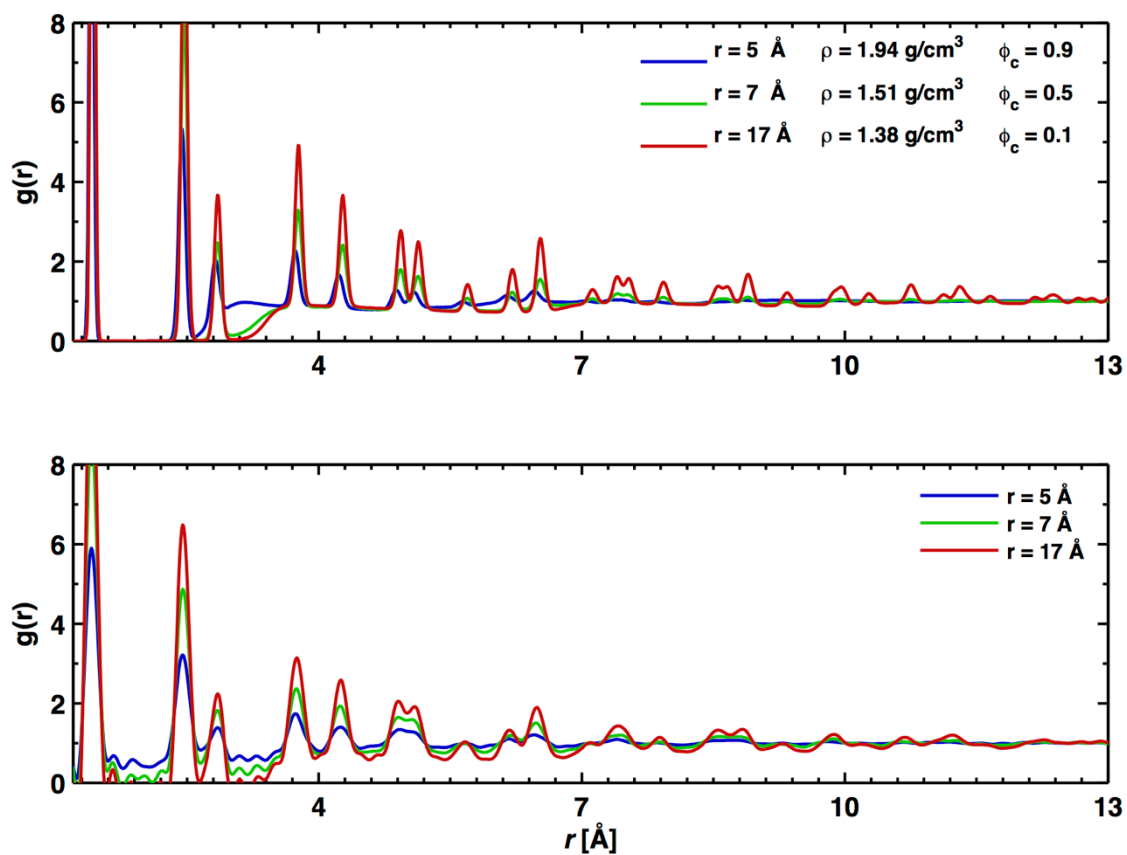


Figure 3.10. (a) Plots of simulated composite systems and (b) the corresponding experimental systems scaled such that the first peak integral equals that of simulation.

Table 3.4. Listing of first peak positions in experimental and simulated PDFs.

Radius		1st peak	2nd peak	3rd peak	4th peak	5th peak
r = 5 Å	Exp.	1.41 Å	2.45 Å	2.84 Å	3.75 Å	4.25 Å
	Sim.	1.41 Å	2.44 Å	2.82 Å	3.72 Å	4.23 Å
r = 7 Å	Exp.	1.41 Å	2.45 Å	2.84 Å	3.75 Å	4.25 Å
	Sim.	1.43 Å	2.47 Å	2.85 Å	3.77 Å	4.28 Å
r = 17 Å	Exp.	1.41 Å	2.45 Å	2.84 Å	3.75 Å	4.24 Å
	Sim.	1.43 Å	2.47 Å	2.85 Å	3.77 Å	4.28 Å

This close comparison is further confirmation that the model structures correspond well to the experimental materials.

The portion of the experimental PDFs that corresponds to d-spacing, the segment between the third and fourth peak, is also reproduced by the simulated PDFs. A lower pyrolysis temperature raises the curve and shifts it to the left. One difference between experimental and simulated PDFs is that the experimental curves have small features in this region. As there should be no features for an all-carbon system, the split must either be due to contamination ripples from Fourier transform of the experimental data (as also evident in the region $1.42 \text{ \AA} - 2.45 \text{ \AA}$) or minor contamination within the experimental samples.

In **Figure 3.11**, the comparison of $G(r)$ for simulated and experimental spectra are shown. The earlier analysis of the simulated PDFs indicated that the combination of larger crystallite size and high crystalline volume fraction gave rise to the most prominent signatures of mesoscale structure. The experimentally synthesized structures do not possess this combination. Instead, the material with a large crystallite size (17 \AA) has a low crystalline volume fraction (0.1) and the material with a high crystalline volume fraction (0.9) has a small crystallite size (5 \AA). Consequently, the absence of long-range order in $G(r)$ is well predicted by the simulated spectra.

3.3.2.4 Effect of crystalline volume fraction on the pair distribution function

We examine the effect of crystalline volume fraction on the pair distribution function, beginning with a focus on the d-spacing region. The crystalline volume fractions used in our simulated models were obtained as visual approximations of volume fraction from electron microscopy. Much as with the experimental d-spacing measurements, the goal here is not to reproduce the exact experimental values via simulation, but to understand the PDF trends as the volume fraction changes. Thus the three percentages chosen for our models represent three distinct systems for which changes in this property can be clearly understood. From **Table 3.2**, the volume fraction of crystalline material within the composite systems has little effect on crystallite breathing distance but an inverse relation with COM distance. This implies that having more crystallites within a system restricts the sliding modes of the planes within adjacent crystallites. In **Figure 3.12**, simulated short-range PDFs for materials with common crystallite size and composite density ($r = 17 \text{ \AA}$, $\rho = 1.38 \text{ g/cm}^3$) and varying crystalline volume fraction are plotted. It is seen that the location of the curve in the d-spacing region does not change; however, the magnitude (particularly at the right edge of the curve) increases.

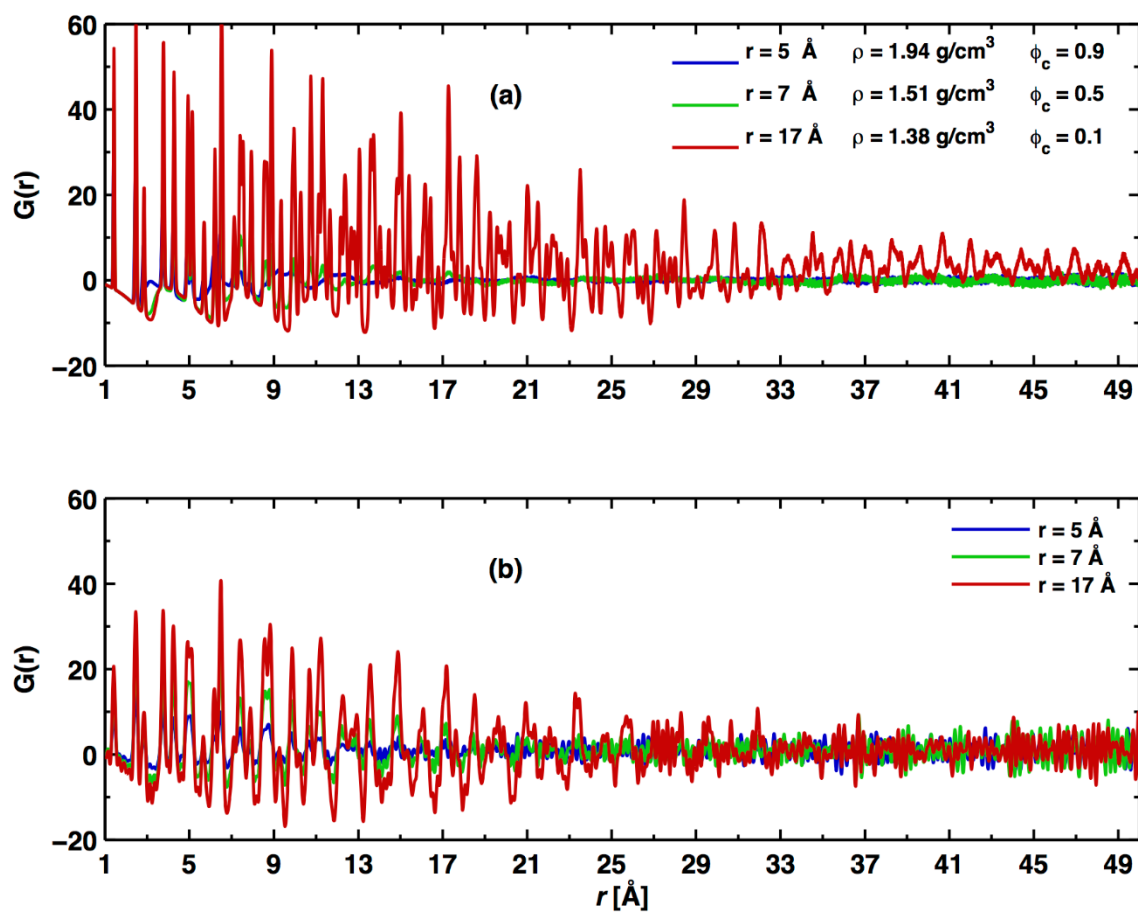


Figure 3.11. Plots of $G(r)$ for (a) simulated composite systems, and (b) the corresponding experimental systems ($Q_{\text{MAX}} = 30$ Å⁻¹) scaled such that the first peak integral equals that of simulation.

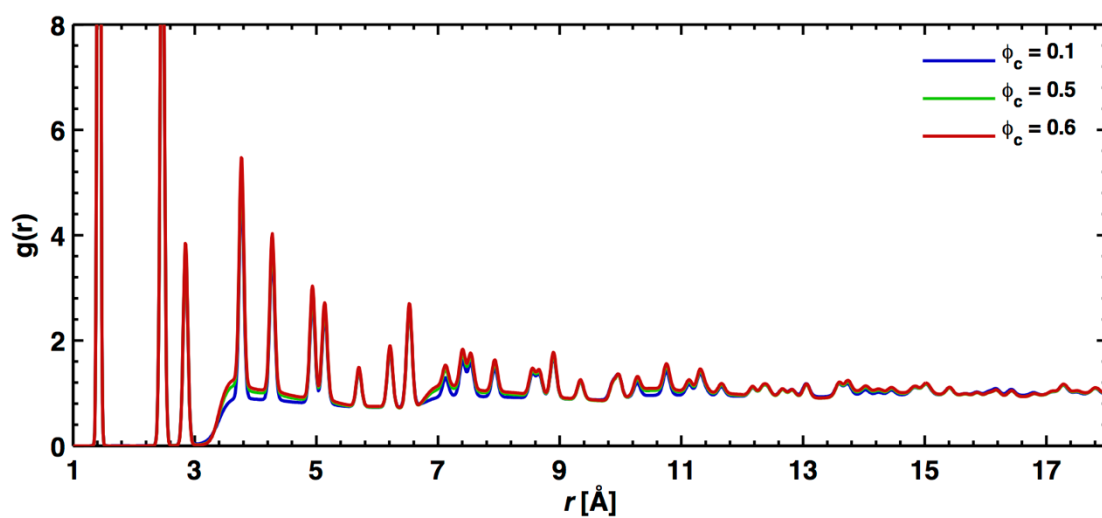


Figure 3.12. Simulated short-range PDFs for materials with common crystallite size and composite density ($r = 17 \text{ \AA}$, $\rho = 1.38 \text{ g/cm}^3$) and varying crystalline volume fraction.

This suggests that breathing distance measurements better correspond to the location of the d-spacing curve while COM distances have an inverse relationship with the magnitude of the right edge of the curve. From an analysis of the decomposition of the PDFs (not shown), the origin of the change in height of the PDF in this range is due to the increase of the intracrystallite interplanar component with increasing crystalline volume fraction.

From **Figure 3.12**, it is also possible to observe that there is little effect on intraplanar peak magnitude as a function of crystalline volume fraction. However, the distance to which these peaks extend decreases as volume fraction increases, which is more readily apparent when plotted as $G(r)$ in **Figure 3.13**. The explanation for this effect lies in the fact that as the crystalline volume fraction decreases, the amorphous volume fraction ($1 - \Phi_c$) increases. The amorphous component also contains intraplanar interactions. The peaks extend at low crystalline volume fraction because the sheets in the amorphous domain are larger in that material. Again, this complicates the use of an envelope function to extract nanocrystallite size from these PDFs. From **Figure 3.12**, it is also seen that increasing crystalline volume fraction leads again to both low and high frequency oscillations in the long-range order of the material.

3.4 CONCLUSIONS

Novel anodes for use in lithium-ion batteries have been produced from the pyrolysis of low-cost lignin materials. These anodes consist of carbon composites with nanoscale structure in the form of nanocrystalline domains dispersed throughout an amorphous carbon matrix. The neutron spectra of these materials have been obtained, and the understanding of these spectra has been realized through the generation of a suite of simulated composite systems that replicate the measurable properties of the experimental systems (summary in **Table 3.5**).

The correct reproduction of the experimental neutron spectra from the simulated systems confirms the accuracy of the model and allows its use in relating unique characteristics of the pair distribution functions to structural properties of the system. In particular, a correspondence between a region of the experimental pair distribution functions and the d-spacing within crystalline domains has been identified, potentially enabling the prediction of microstructural features in composite systems. This information provides insight useful in the design of advanced energy storage materials and manufacturing methods.

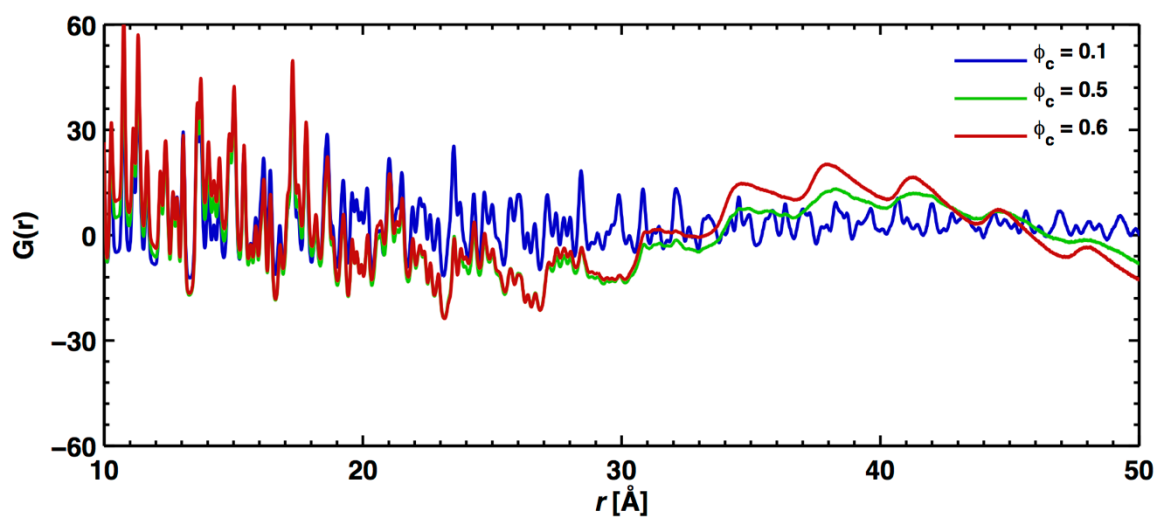


Figure 3.13. The long-range effect of crystalline volume fraction on the DDCF of a representative material ($\rho = 1.38 \text{ g/cm}^3$, $r = 17 \text{ \AA}$).

Table 3.5. Summary of effects of different properties on the PDFs.

	Peak magnitude	Peak extent	D-spacing region (~3-4 Å)	Long-range order
Increasing crystallite radius	Increases	No effect for low Φ_c Increases for high Φ_c	No visible effect	Amplifies oscillations due to changing Φ_c
Increasing composite density	Decreases	No observed effect	Increases and left-shifts peak	No observed effect
Increased crystalline volume fraction	No significant effect	Governed by amorphous phase	Increases in magnitude but no peak shift	Gives rise to both high frequency (~3 Å) and low frequency (~20 Å) oscillations

Therefore, it is important to develop computational tools for analysis, potentially without reliance on computationally-intensive molecular dynamics simulations, that allow for an estimation of the decomposition based on structural factors such as composite density, crystallite size, and crystalline volume fraction. Extraction of d-spacing for example from the decomposition is then straight-forward.

Finally, as d-spacing has a direct influence on both the storage and rate of diffusion of lithium ions within the composite anodes, this capability will allow the understanding of lithium-ion diffusion within charged and uncharged lithiated composites from the pair distribution function alone.

3.5 ACKNOWLEDGMENTS

N.M. was supported by a grant from the Oak Ridge Associated Universities High Performance Computing Program, by a grant from the Sustainable Energy Education and Research Center of the University of Tennessee and by a grant from the National Science Foundation (DGE-0801470). This research project used resources of the National Institute for Computational Sciences (NICS) supported by NSF under agreement number: OCI 07-11134.5. This research was also sponsored in part by the Laboratory Directed Research and Development Program of Oak Ridge National Laboratory, managed by UT-Battelle, LLC, for the U.S. Department of Energy. This research at Oak Ridge National Laboratory's Spallation Neutron Source was sponsored by the U.S. Department of Energy, Office of Basic Energy Sciences.

4 INTERFACIAL LI-ION LOCALIZATION IN HIERARCHICAL CARBON ANODES

This chapter is a slightly revised version of a paper to be submitted by Nicholas McNutt, Orlando Rios, and David Keffer:

N. W. McNutt, O. Rios, and V. Maroulas, D. J. Keffer, "Interfacial Li-ion Localization in Hierarchical Carbon Anodes", to be submitted.

The use of "we" in this part refers to the co-authors and the author of this dissertation. My primary contributions to this paper include (1) development of the problem into a work relevant to the study of Li-ion localization in uncharged and charged lignin-derived carbon composites, (2) experiments conducted at the NOMAD beam line at the Spallation Neutron Source at Oak Ridge National Laboratory, (3) implementation of the simulation methodology, (4) all of the simulation work and analysis, and (5) almost all of the writing.

4.1 INTRODUCTION

Low-cost, high-quality lithium batteries are a desirable product in a market that is moving towards cleaner, less expensive, and more efficient energy. The development of these batteries occurs with a trade-off between cost and effectiveness. High-performance batteries are often accompanied by a difficult manufacturing process or a steep financial penalty [1]. On the other hand, batteries developed from low-cost materials are produced at a charge capacity, cycling capability, or safety penalty [1]. Recently however, materials derived from abundant, low-cost lignin sources show promise in achieving a good balance in both financial and performance aspects. Novel processes for the development of this raw material using advanced carbon fiber technologies at Oak Ridge National Laboratory (ORNL) yield superior anode materials in the form of all-carbon composites composed of nanoscale crystalline domains dispersed within an amorphous matrix [3]. Carbon-carbon composite materials have advantages including high reversible capacity, low irreversible capacity loss, high cycle life due to strong mechanical integrity, and enhanced safety because of a lack of substrate dissolution during overcharge [2].

Herein, we report the discovery of a novel mechanism of Li-ion storage, one in which Li^+ is not intercalated between layers of carbon, but rather localized at the interface of crystalline carbon domains. This implies that the charge capacity of these types of hierarchical materials is at least partially proportional to the surface area of the phase boundary. While many studies have been performed to understand the nature

of lithium storage in carbon anodes, most research has focused on homogeneous or non-hierarchical materials (e.g. graphite). For those materials, it has been experimentally determined that Li^+ intercalates between adjacent graphitic planes.

For disordered carbon anodes, a significant amount of research was performed on these materials in the mid-1990s in order to elucidate the mechanism of Li-ion storage. Dahn et al. proposed three distinct mechanisms responsible for ion localization: 1) Li-ion intercalation occurs between layers of graphitic carbon, but not between layers that exhibits high turbostratic disorder 2) the maximum amount of lithium that can be inserted is proportional to the atomic ratio of hydrogen to carbon, suggesting that “lithium binds somehow in the vicinity of the H atoms” and 3) in materials that are predominantly composed of loose layers of graphene, lithium appears to adsorb onto both sides of the carbon sheets [72]. Zheng, Liu [73] find a “striking correlation” between the H/C ratio and Li-ion capacity and conjecture that the phenomenon is due to binding of Li in the vicinity of hydrogen atoms. They note that this high charge capacity comes with a penalty, as the anode voltage profiles exhibit a large hysteresis. In a subsequent study, they show that lithium must overcome an energy barrier before it can localize near edge-terminating hydrogens. They hypothesize that reducing this energy barrier is paramount to decreasing the hysteresis penalty.

Approaching the topic computationally, Papanek, Radosavljevic [74] perform semiempirical simulations and reveal that the correlation between ion capacity and the H/C ratio is partially attributed to Li binding at H-terminated edges of hexagonal carbon fragments. They note that the local environment resembles that of $\text{C}_2\text{H}_2\text{Li}_2$. Rothlisberger and Klein [75] find a similar $\text{C}_2\text{H}_2\text{Li}_2$ geometry in ab initio molecular dynamics simulations.

4.2 METHODS

For our hierarchical carbon anodes, a large atomistic model (75,795 C, 32,353 H and 5,012 Li) is necessary in order to correctly capture all of the experimentally observed nanoscale structural features, including the presence of phase boundaries. In a previous study of these unique materials, we developed such a model and used molecular dynamics (MD) simulations to understand the structural properties of the uncharged (unlithiated) anode. The OPLS-AA forcefield [43] was chosen for the MD simulation in order to allow structural relaxation over a long period of time. We found that the structural characteristics of the

equilibrated model closely matched the features revealed experimentally via neutron scattering, thus validating our model and choice of potential [76].

For this work, a computational method that accurately accounts for the chemical reactivity of Li^+ is necessary. As it is not currently feasible to use quantum chemical techniques to study such large systems, we instead utilize ReaxFF, a reactive MD forcefield that addresses both the size of the simulation and the chemical reactivity of lithium [77-79]. The specific ReaxFF potential chosen was developed on the basis of density functional theory (DFT) calculations and is designed to account for chemical interactions between lithium, carbon, and hydrogen [80, 81]. This potential has been successfully used to understand the fracture mechanisms of lithiated graphene [82].

Our anode model is composed of small domains of crystalline carbon interspersed throughout an enveloping matrix of amorphous carbon. The crystalline carbon consists of nanocrystallites 7 Å in radius, and the density of the overall composite is 1.51 g/cm³. In order to guide the initial placement of lithium ions in the system, we intercalated the ions between the layers of the carbon nanocrystallites. Raju et al. showed that when lithium atoms are placed outside of isolated stacks of carbon layers, the atoms tend to migrate into the spaces between the layers [80]. In addition to carbon and lithium, the composite contains hydrogen atoms that run along the edges of the carbon sheets that constitute the crystalline and amorphous domains.

The computational model was equilibrated in the canonical (NVT) ensemble using the Nosé-Hoover thermostat [57, 62]. The duration of the equilibration was 224 ps, and the timestep was 0.25 fs. LAMMPS [42] was used to perform the simulation. For this work, “equilibration” is defined as the point in which all energy contributions to the total system energy have significantly leveled off. All properties are computed as time-averages across a flat energy profile.

We investigated two concentrations of Li^+ : a high ion loading at 147.8 mAh g⁻¹, and a lower ion loading at 19.8 mAh g⁻¹. The high loading value was selected as the maximum charge capacity for this particular anode material [3] (with the assumption that each unit of positive electric charge e^+ corresponds to exactly one Li^+), and the low loading value was selected as the value that would intercalate one Li^+ between two planes of a crystallite, given that all crystallites are occupied.

Because the redistribution processes of Li^+ may occur on timescales greater than that accessible to atomistic simulation (milliseconds or greater), we investigated two initial conditions for each

concentration of Li^+ , one in which all Li^+ are initially intercalated within planes of the graphitic nanoparticles and the other in which all ions are placed in the amorphous domain.

4.3 RESULTS

A snapshot of the system upon reaching a flat energy profile is shown in **Figure 4.1**. From the snapshot, it is immediately clear that Li-ions do not remain strictly localized within the carbon nanocrystallites. In order to determine the extent of Li-ion migration out of the carbon nanocrystallites, a smaller (yet compositionally identical) system containing just one nanocrystallite embedded within an amorphous carbon matrix was created and simulated for a duration of 2 ns. The results from this simulation (shown in **Figure 4.2**) highlight the egress of Li-ions from the interior vacancies of the nanocrystallite to the interfacial boundary separating the crystalline and amorphous carbon domains.

Within carbon anodes, an irreversible capacity loss occurs when Li-ions bind too strongly to the encompassing environment; the high adsorption energy leads to effectively infinite adsorbate stay times. Conversely, a failure to store charge occurs when Li-ions bind too loosely, resulting in low charge capacity. In order to understand the mobility of the ions in the carbon composite, we study the localization of Li-ions as a function of their energy and the local environment.

The distribution of Li-ion energies is shown in **Figure 4.3**. For equivalent levels of ion loading, the distributions of binding energies differ somewhat with initial condition, indicating that true Li-ion equilibration occurs on a much longer time scale than MD simulation allows. However, the crystalline distribution tended toward the amorphous distribution, while the amorphous distribution tended to stay the same, indicating that a complete long-time equilibration would have the final distribution lie in between the two initial distributions, but very close to the short-time equilibrated amorphous distribution. The data from these distributions reveals several insights. First, conventionally, an adsorption energy of ~ 10 kcal/mol is considered the threshold between physisorption and chemisorption [83-85]. It is clear from **Figure 4.3** that both chemisorption and physisorption occur within the hierarchical carbon anode. Second, a high charge density is necessary to push Li-ions into the realm of chemisorption. This can be stated in an alternative way. In physisorption, deep binding sites are occupied first and weak sites later, resulting in a binding energy that weakens with an increase in loading.

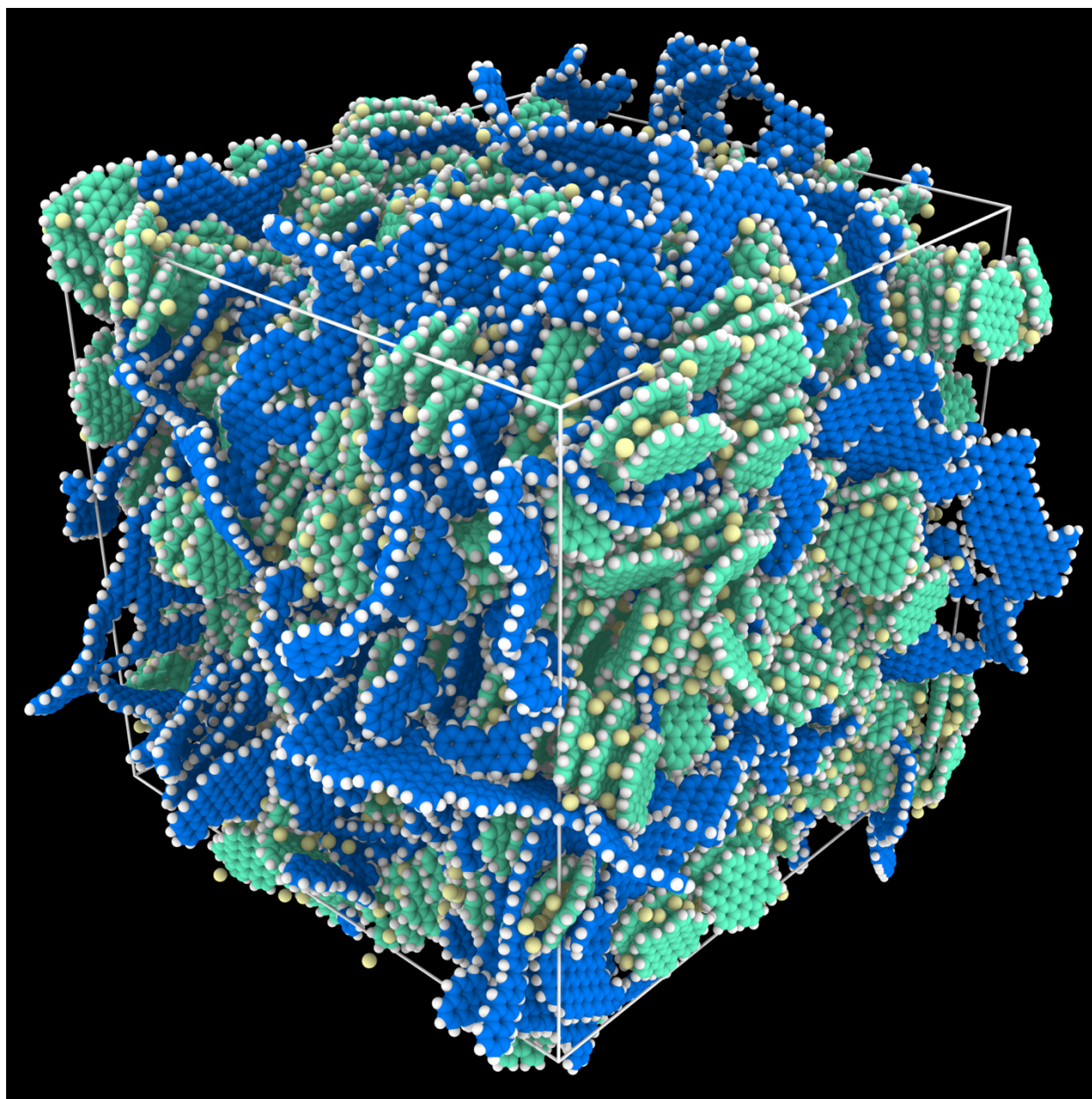


Figure 4.1. The hierarchical carbon anode model after equilibration. Atoms are colored by type: amorphous carbon is blue, crystalline carbon is green, hydrogen atoms are white, and lithium ions are yellow. This simulation corresponds to a loading of 147.8 mAh g^{-1} and an initial condition in which all atoms were initially intercalated within the crystalline domain.

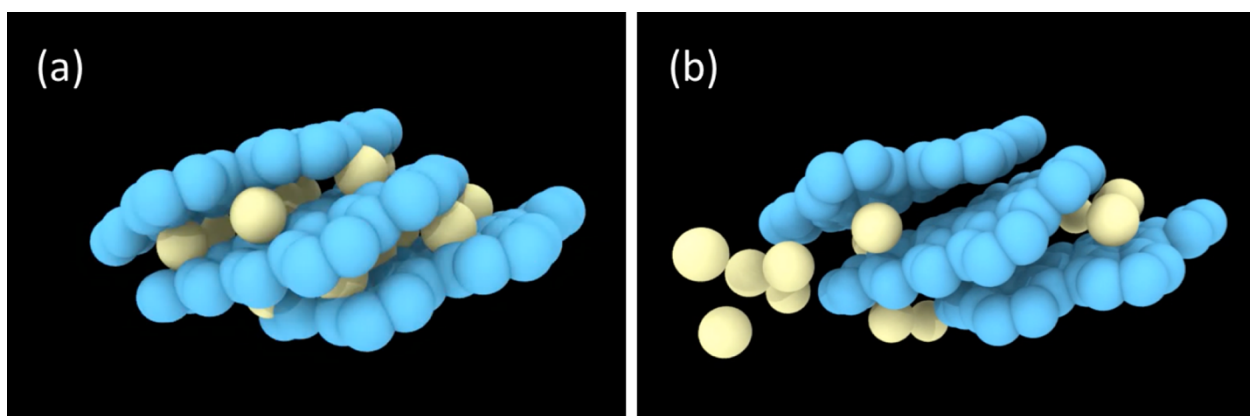


Figure 4.2. A small composite system with Li-ions intercalated in the crystalline domain (a) pre-equilibration and (b) post-equilibration. For clarity, the amorphous carbon matrix and hydrogen atoms surrounding the carbon nanocrystallite are rendered invisible.

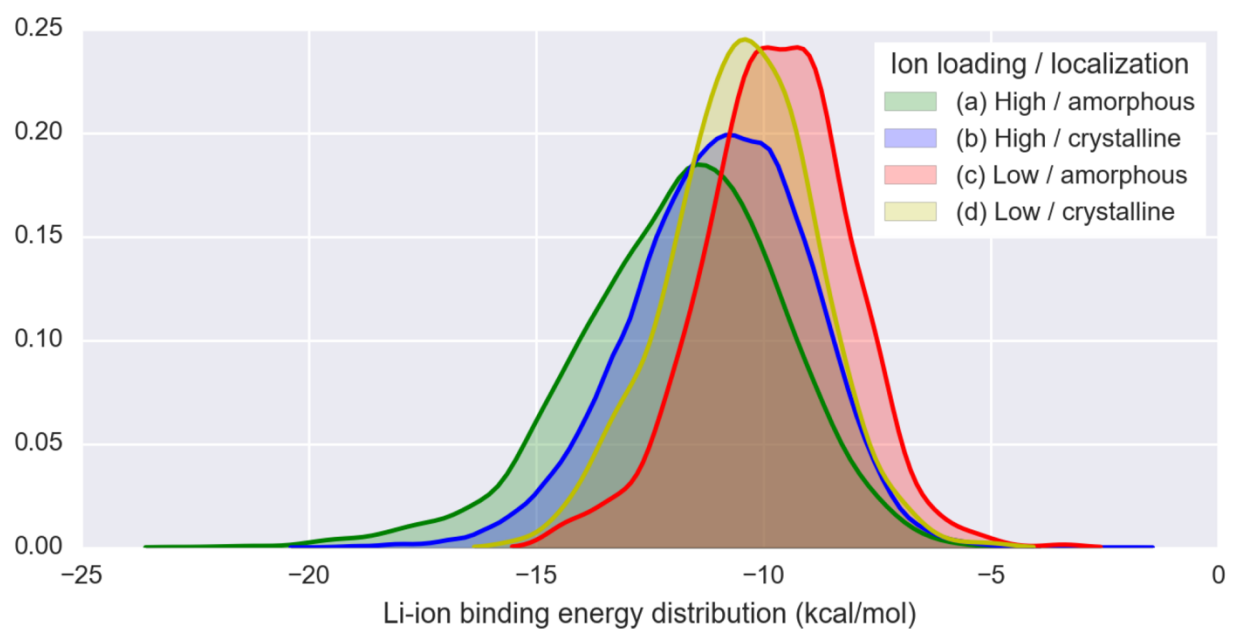


Figure 4.3. Probability density functions of the distribution of Li-ion binding energies in the equilibrated large composite anode system for (a) high amorphous loading, (b) high crystalline loading, (c) low amorphous loading, and (d) low crystalline loading.

Here, the opposite trend is observed. The average binding at high loading is stronger than at low loading because strong binding sites are created only with the additional loading of Li^+ . This suggests a cooperative aggregation of Li^+ . Such a phenomenon can be confirmed through an examination of pair distribution functions.

The pair distribution functions (PDFs) for Li-L, Li-H, and Li-C pairs are shown in **Figure 4.4** for a selection of Li-ion energy ranges for a loading of 147.8 mAh g^{-1} and an initial condition in which all atoms were initially localized within the amorphous domain. For the Li-Li PDF (**Figure 4.4(a)**), the highest density peak occurs when Li-ions are strongly bound (chemisorbed). This trend reverses for the Li-C PDF (**Figure 4.4(c)**), as the highest peak occurs when Li-ions are weakly bound (physisorbed). The most interesting observation is in the Li-H PDF (**Figure 4.4(b)**), however, as the highest density peak occurs at a moderate energy level at the boundary of the chemisorption/physisorption transition ($\sim 12 \text{ kcal/mol}$). This suggests that specific types of Li-H pairs exist for particular Li-ion energies. Furthermore, because the Li-H peaks are much narrower than the Li-Li and Li-C peaks, this implies that the distances between Li-H atom pairs fall within a tight range.

In order to gain a deeper insight into the nature of Li-ion localization, it is important to understand not just the radial component of the environment surrounding a given ion, but the angular components as well. To this end, an original technique has been developed to extract 3D structural motifs from atomic position data. The local atomic environments surrounding each Li-ion are sorted into one of three groups on the basis of the ion's binding energy. We then note that the central atom's energy is invariant to certain transformations of its local environment. These transformations include rotations, inversions, and permutations of atoms of the same type. In order to isolate the symmetry-invariant information contained within the environment, the atomic configurations within each group are rotated and reflected in such a way as to globally maximize their overlap. The results of this process are shown in **Figure 4.5**.

In **Figure 4.5**, we present three-dimensional density distributions of atoms around a central Li atom for: (a) strong binding energies (-20.86 to -14.04) kcal/mol , (b) moderate binding energies (-11.04 to -10.71) kcal/mol , and (c) weak binding energies (-8.20 to -1.08) kcal/mol . It is apparent from **Figure 4.5(a)** that the most structured environment is the one surrounding the most strongly bound Li-ions. The neighboring hydrogen atoms are localized into tight regions of space, and the neighboring Li-ions are located shortly beyond the hydrogens. The Li ions are arranged at the corners of a cube. The H atoms are arranged at the faces of a cube.

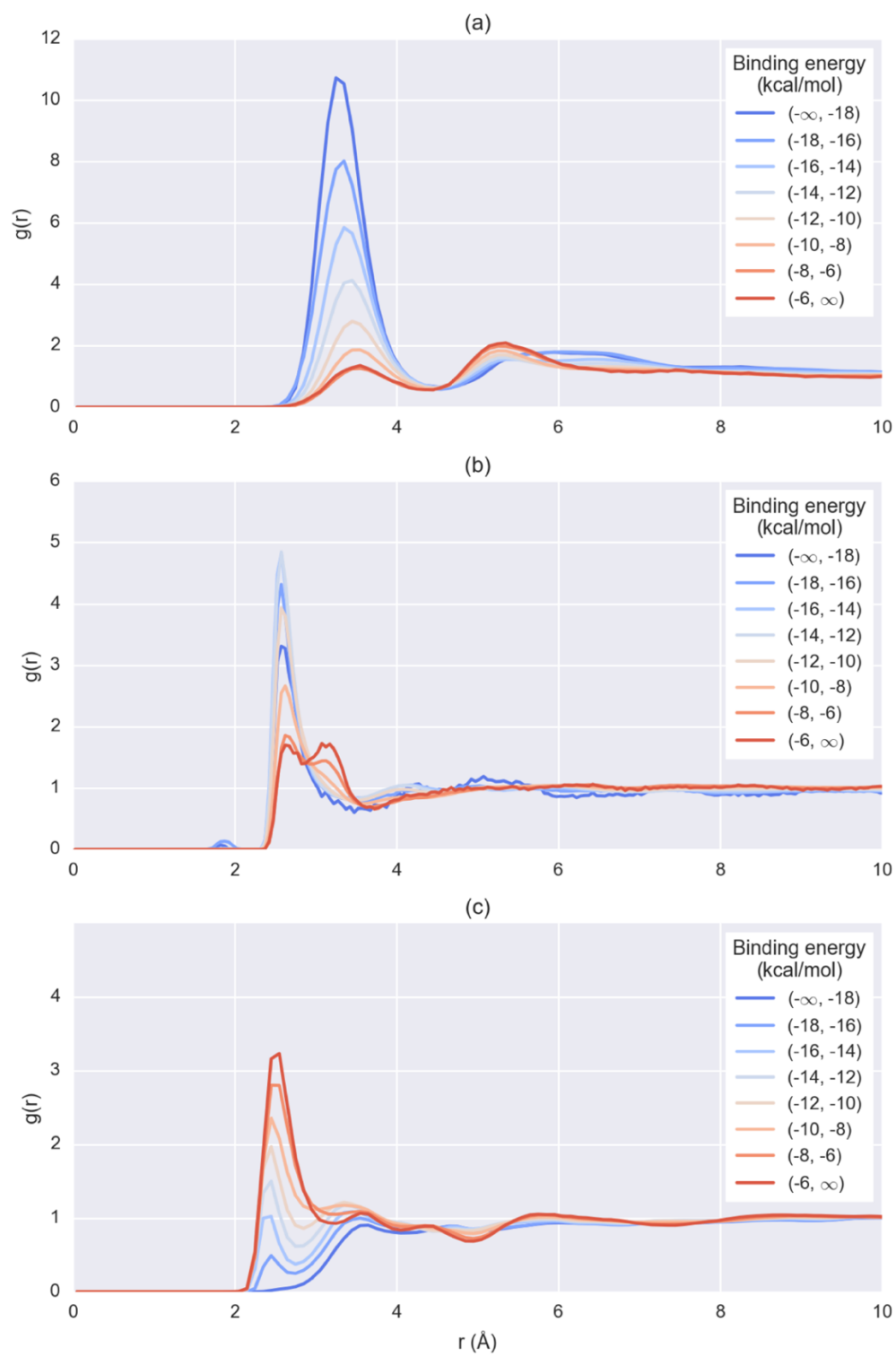


Figure 4.4. PDFs for (a) Li-Li, (b) Li-H, and (c) Li-C pairs of atoms.

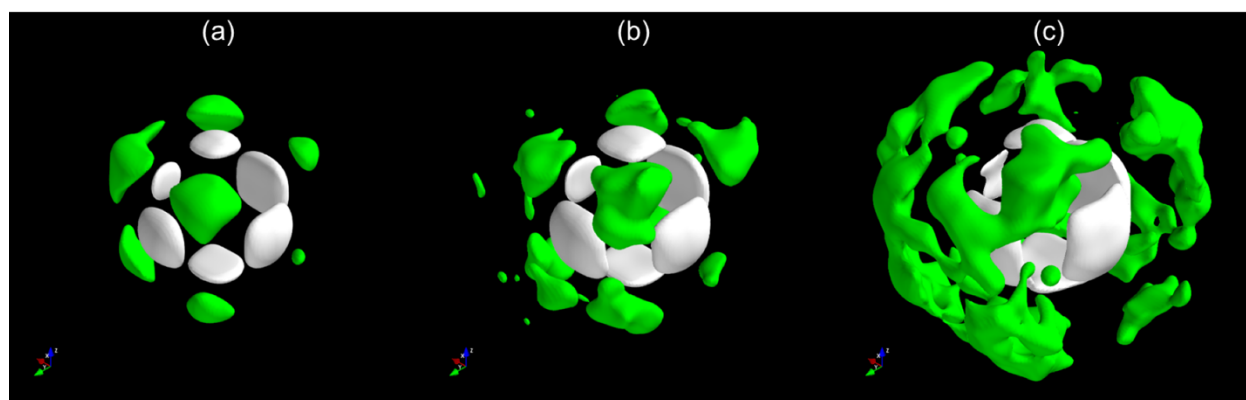


Figure 4.5. 3D density distributions of Li (green) and H (white) for (a) strong Li-ion binding energies, (b) moderate Li-ion binding energies, and (c) weak Li-ion binding energies. Each distribution is centered around a Li ion, which is not shown.

Note that a stoichiometry of a Li-H complex cannot be directly extracted from these images since the density contours of the two species are different. (One can think of the white clouds corresponding to H as having a lower occupancy than the green clouds describing the Li^+ distribution). This cube represents an archetypal structure averaged over all strongly bound Li^+ . No single local environment observed in the simulation corresponds to this reference. On the contrary, manifestations in the simulation can be considered highly defective perturbations of this structure. The defects are due to (1) the disordered nature of the carbon composite and (2) thermal energy.

From **Figure 4.5(b)** and **Figure 4.5(c)** it is seen that as the Li-ions become more weakly bound, two changes occur. First, the clouds expand in size, corresponding to the local environment becoming more disordered. Second, the neighboring Li-ions are found at a greater distance from the central ion. This further validates the idea that strong binding is a result of a cooperative Li and H effect.

Lastly, we look at the relationship between charge and binding energy. **Figure 4.6** reveals a tight correlation between the two properties. Chemisorbed Li-ions tend to share their charge with neighboring atoms, whereas physisorbed ions tend to retain more of their +1 ionization. Interestingly, in this material the average charge of Li^+ in the anode is found to be $0.28 e^+$, indicating a state of partial charge transfer between the atom and the formal Li^{+1} ion.

In **Figure 4.7**, the carbon-carbon PDF from the simulation at the high concentration with initial positions in the amorphous domain is compared to experimental neutron scattering data for a lignin carbon composite [3, 76] in both the uncharged and lithiated states. From this plot, it is evident that the experimental PDF for the lignin-based anode closely resembles the PDF of our computational model. The change upon lithiation in the carbon composite material is negligible, an indication of the lack of atomic level restructuring of the anode during the charging process, resulting in the high cyclability of these materials. This lack of restructuring also contrasts with the restructuring that occurs in graphite during the charging process [86]. The X-ray diffraction peak for Li-intercalated graphite reveals a significant change in the interlayer spacing between planes of carbon. This provides experimental evidence for a mechanism of ion storage in our materials that differs from that of conventional graphitic anodes.

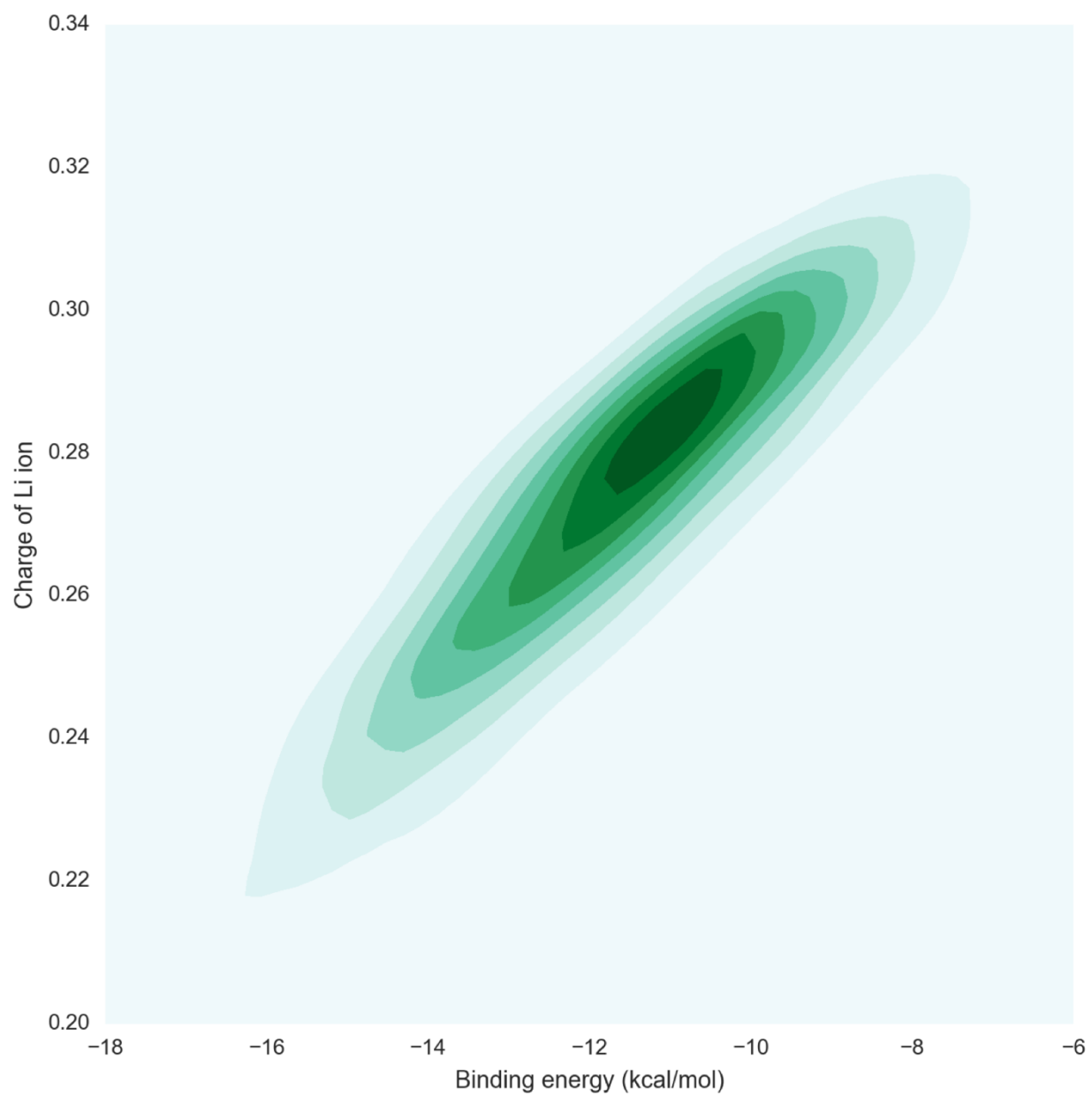


Figure 4.6. Li-ion partial charge as a function of ion energy.

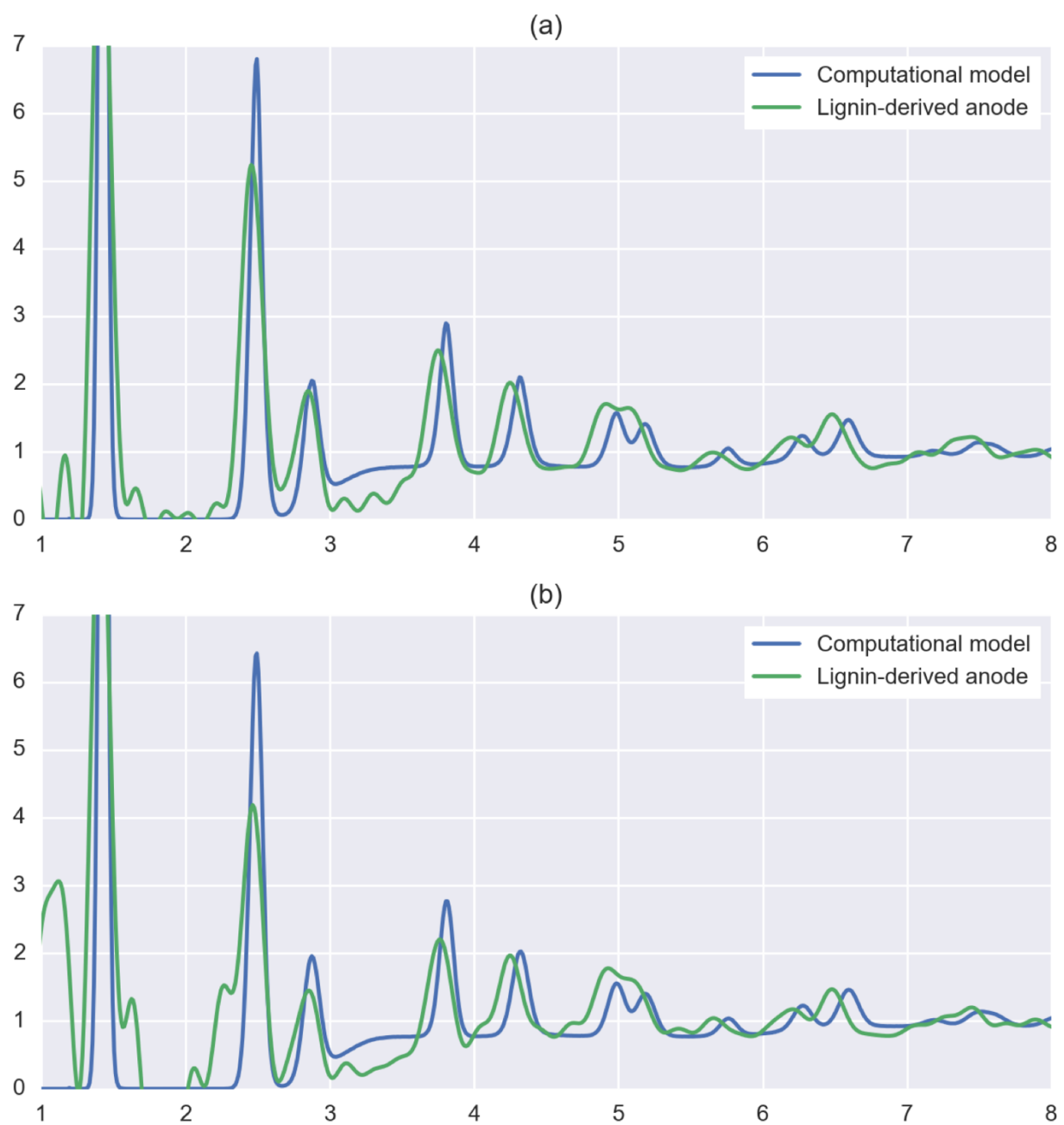


Figure 4.7. Comparison of the carbon (C-C) PDFs for (a) the uncharged materials and (b) the lithiated materials.

4.4 CONCLUSIONS

By inspecting the data in a variety of ways, a clear trend emerges for the nature of Li-ion localization in these hierarchical carbon materials. Most notably — and counter to the nature of ion storage in graphitic carbons — Li-ions do not intercalate between the layers of $r = 7 \text{ \AA}$ carbon nanocrystallites. The most energetically favorable positions for Li-ion storage are located near the hydrogen atoms located at the interface between the crystalline and amorphous domains of carbon. Because hydrogen content scales with interface size, Li-ion storage capacity (and thus charge capacity) is proportional to the surface area of the interfacial boundary. This suggests that a material with small crystallites, a high volume fraction of crystalline material, and a high total density should correspond to a high capacity anode material. As the experimental carbon anode pyrolyzed at $1000 \text{ }^{\circ}\text{C}$ has exactly these properties, this suggests that future anode developments should focus on emphasizing these structural traits.

The binding energies of lithium are highly variable, ranging from chemisorption to physisorption. This heterogeneity in binding energy can be partially captured in the PDFs, which show Li^+ aggregation for strongly bound Li^+ . For these composites, we have identified archetypal structures that correspond to the atomic density distributions of Li and H. Observed deviations from this structure reflect structural and thermal disorder.

4.5 ACKNOWLEDGMENTS

N.M. was supported by a grant from the Oak Ridge Associated Universities High Performance Computing Program, by a grant from the Sustainable Energy Education and Research Center of the University of Tennessee, by a grant from the National Science Foundation (DGE-0801470), and by the STAIR program at the University of Tennessee. This research project used resources of the National Institute for Computational Sciences (NICS) supported by NSF under agreement number: OCI 07-11134.5. This research was also sponsored in part by the Laboratory Directed Research and Development Program of Oak Ridge National Laboratory, managed by UT-Battelle, LLC, for the U.S. Department of Energy. This research at Oak Ridge National Laboratory's Spallation Neutron Source was sponsored by the U.S. Department of Energy, Office of Basic Energy Sciences.

5 LI-ION LOCALIZATION AND ENERGETICS AS A FUNCTION OF ANODE STRUCTURE

This chapter is a slightly revised version of a paper under preparation by Nicholas McNutt, Marshall McDonnell, Orlando Rios, and David Keffer:

N. W. McNutt, M. McDonnell, O. Rios, and D. J. Keffer, "Li-ion Localization and Energetics as a Function of Anode Structure", to be submitted.

The use of "we" in this part refers to the co-authors and the author of this dissertation. My primary contributions to this paper include (1) the selection and development of the problem into a work relevant to the study of the effect of carbon anode structure on Li-ion localization, (2) the implementation of the simulation methodology, (3) all of the simulation work and analysis, and (4) all of the writing.

5.1 INTRODUCTION

Low-cost, high-quality lithium batteries are a desirable product in a market that is moving towards cleaner, less expensive, and more efficient energy. The development of these batteries occurs with a trade-off between cost and effectiveness. High-performance batteries are often accompanied by a difficult manufacturing process or a steep financial penalty [1]. On the other hand, batteries developed from low-cost materials are produced at a charge capacity, cycling capability, or safety penalty [1]. Recently however, materials derived from abundant, low-cost lignin sources show promise in achieving a good balance in both financial and performance aspects. Novel processes for the development of this raw material using advanced carbon fiber technologies at Oak Ridge National Laboratory (ORNL) yield superior anode materials in the form of all-carbon composites composed of nanoscale crystalline domains dispersed within an amorphous matrix [3]. Carbon-carbon composite materials have advantages including high reversible capacity, low irreversible capacity loss, high cycle life due to strong mechanical integrity, and enhanced safety because of a lack of substrate dissolution during overcharge [2].

On the molecular scale, lignin is a complex mix of branched polyaromatic macromolecules containing a large fraction of aromatic rings resulting in a high char yield (over 40 wt. %) after pyrolysis [4, 5]. A key step in the manufacturing process is the pyrolyzation and subsequent thermal annealing of lignin fiber. The resulting structural properties of the composite materials are an incompletely understood function of the specific pyrolysis temperature and thermal history.

In this work, we used neutron diffraction on three lignin-derived carbon samples to obtain experimental pair distribution functions (PDFs) to compare with our lithiated/unlithiated simulation results. In contrast to X-rays, neutrons are more sensitive to the light elements, and neutron time-of-flight diffraction enables higher resolution PDFs because of the broader Q-range accessible [54]. In experimental PDFs, peak position, height, and width are attributed to the inter-atomic distance, coordination number, and thermal motion of atoms.

Although such qualitative information can be directly observed in the experimental PDF, a fundamental understanding of the local structure on an atomic level requires advanced analytical methods to extract quantitative structural information [55-57]. It is therefore necessary to develop a predictive model that reproduces the experimental PDF.

In this work, an atomistic, computational model is developed through the use of molecular dynamics (MD). This procedure simulates the atomic interactions among the crystalline and amorphous domains of the composite systems and reveals both nanoscale and mesoscale phenomena. The properties of interest in these carbon composite systems are those that cannot be easily obtained through experiment, but whose understanding will lead to the development of better anode materials. These properties include the d-spacing between carbon layers (graphene) within the nanocrystallites, the nature of how these nanocrystallites distribute and deform with the amorphous carbon matrix, and the nature of lithium ion energetics and localization within this anode material. The first two properties are addressed in a previous article [76], which focuses exclusively on uncharged anode materials. The last property two properties are addressed herein.

5.2 METHODS

5.2.1 SYNTHESIS

The carbon materials with nanoscale structure were synthesized from solvent extracted hardwood lignin. Lignin is a highly cross-linked polyphenolic polymer without repeating units that yields 40 to 60 wt % char after pyrolysis [4, 5]. Conversion of lignin into nanoscale graphitic material consists of oxidative stabilization to 250 °C in flowing air followed by pyrolysis under inert atmospheres. The scale of the crystalline domains is a result of systematically varying the annealing temperatures (1000, 1500, and 2000 °C).

5.2.2 STRUCTURAL CHARACTERIZATION

The experimentally obtainable parameters describing these three carbon structures include estimates of the overall composite density, the volume fraction of crystalline material, and the size of the crystallites. The volume fraction was determined through the use of transmission electron microscopy, and crystallite diameter was obtained through Scherrer analysis of X-ray diffraction measurements obtained using a PANalytical X'Pert Pro MPD diffractometer with Cu K α 1 radiation [3].

5.2.3 NEUTRON SCATTERING

The neutron scattering experiments were carried out at the Nanoscale-Ordered Materials Diffractometer (NOMAD) at the Spallation Neutron Source at Oak Ridge National Laboratory [54]. Three samples (~150 mg each) were measured in 3 mm quartz capillaries at room temperature for a total of 2 hours. The measurements were performed in an argon atmosphere to reduce scattering from the air. In order to obtain the structure factor $S(Q)$, the background was subtracted and the data was normalized by the scattering from the solid vanadium rod. The experimental PDFs were obtained by a Fourier transform of $S(Q)$ using $Q_{\text{MAX}} = 30 \text{ \AA}^{-1}$ for all samples.

5.2.4 SIMULATION

The fifteen computational models studied in this work are the same atomistic systems studied previously [76]. These systems are shown in **Figure 5.1**. For the three experimental systems, the only parameter that can be directly controlled is the lignin pyrolysis temperature; however, the systems that result from pyrolysis have three measurable properties: crystallite size, volume fraction of crystalline material, and total composite density. Using the computational models, these properties can be varied independently in order to isolate their effect on the structure of the material and to determine their effect on the energetics and localization of Li-ions.

For our previous work, the OPLS-AA forcefield [43] was used to investigate the structural properties of the uncharged composites [76] and the crystallites contained within them [58]. For this work, however, an accurate simulation requires taking into consideration the chemical reactivity of Li-ions. To this end, we utilize the ReaxFF forcefield [77-79], parameterized for systems containing C/H/Li atoms [80]. This forcefield has been successfully used to understand the fracturing mechanism behind lithiated graphene [82].

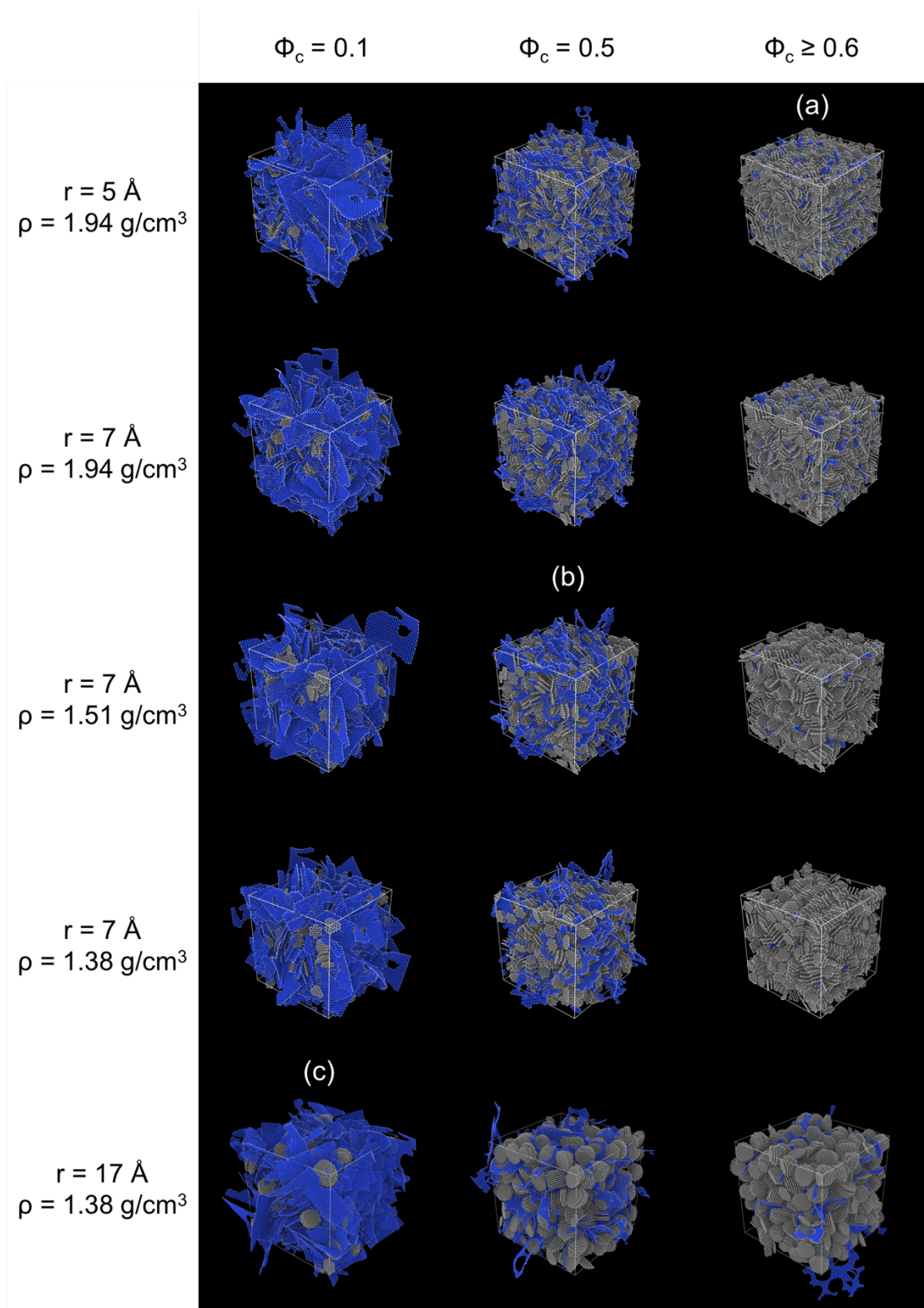


Figure 5.1. The model composite systems with properties specified. Crystalline carbon is gray; amorphous carbon is blue; hydrogen is white. The model systems that correspond to the experimental systems are labeled on the basis of pyrolysis temperature: (a) 1000 °C, (b) 1500 °C, and (c) 2000 °C.

The uncharged model systems were first equilibrated in the canonical (NVT) ensemble at 298 K using the Nosé-Hoover thermostat [57, 62, 63]. For this work, “equilibration” is defined as the point in which all energy contributions to the total system energy have significantly leveled off. All properties are computed as time-averages across a flat energy profile. The simulations were conducted in LAMMPS [42] using the ReaxFF forcefield, and with a timestep of 0.25 fs.

Once the uncharged systems reached equilibration, lithium ions were added to each composite to induce a charged state. For slurry-coated electrodes, Tenhaeff, Rios [3] show that the lignin-derived composites have average specific charge capacities (over the first 70 cycles) of 349.8 mAh g⁻¹, 147.8 mAh g⁻¹, and 126.1 mAh g⁻¹ for the composites pyrolyzed at 1000 °C, 1500 °C, and 2000 °C, respectively. We assume that one unit of positive electric charge (e⁺) in the experimental systems corresponds to exactly one Li⁺ in the model systems. Because our previous results indicate that it is energetically unfavorable for Li-ions to intercalate within the crystalline domain [87], we place the Li-ions into the amorphous domain using a random placement strategy that avoids placing ions too close to existing atoms/ions.

Simulating one model system for every unique combination of experimental properties would result in too many systems for meaningful analysis, so we selected eleven charged systems that allow us to understand the effect of changing one property in isolation. These systems are shown in **Table 5.1**.

Table 5.1. Collections of systems with one property changed.

Constant	Changed prop.	Changed values
$\rho = 1.94, \Phi_c = 0.5, q = 147.8$	Radius (Å)	5 → 7
$r = 7, \Phi_c = 0.5, q = 147.8$	Density (g/cm ³)	1.38 → 1.51 → 1.94
$r = 7, \rho = 1.51, q = 147.8$	Volume fraction	0.1 → 0.5 → 0.75
$r = 7, \rho = 1.38, \Phi_c = 0.5$	Charge (mAh/g)	126.1 → 147.8 → 349.8

5.3 RESULTS

Snapshots of the three charged model systems that correspond to the experimental systems are shown in **Figure 5.2**.

5.3.1 PAIR DISTRIBUTION FUNCTIONS

The pair distribution function, $g(r)$, is presented in this work. The PDF is calculated in simulation as the ensemble average of the local density distribution to the average bulk density [64]. The PDF emphasizes the local structure at low r .

5.3.1.1 Effect of lithiation on carbon structure

The PDFs of the experimental systems in the uncharged and charged states are shown in **Figure 5.3**. The PDFs of the simulated models corresponding to the experimental systems are shown in **Figure 5.4**. The presence of waviness in the PDFs of the experimental systems below 1 Å is caused by noise. Both the experimental and simulated systems change very little after lithiation. The good correspondence between simulation and experiment for the uncharged systems was determined previously [76]. **Figure 5.4** demonstrates that this correspondence holds even for the charged systems.

Similar to the procedure performed in [76], we decompose the total PDF of a representative system into component PDFs that sum to reproduce the original function. This concept is expounded upon in [88] to develop a mathematical theory describing the way that small-scale structural features combine to result in the overall PDF. Abbreviations for these component functions are given in **Table 5.2**.

From the plot in **Figure 5.5**, it is evident that very little structural change occurs as a result of lithiation. However, the simulation duration was at too small of a time scale to rule out the possibility of long term structural deformation, one that occurs at a time far beyond the point in which a flat energy profile is attained. A close-up view of these component PDF functions is shown in **Figure 5.6**. Even at this small length-scale, it is apparent that very little changes structurally, however, the C-C component does show a slight decrease in the height of its first peak, indicating that the nanocrystallites within the composite system tend to fall apart a bit more in the presence of Li-ions.

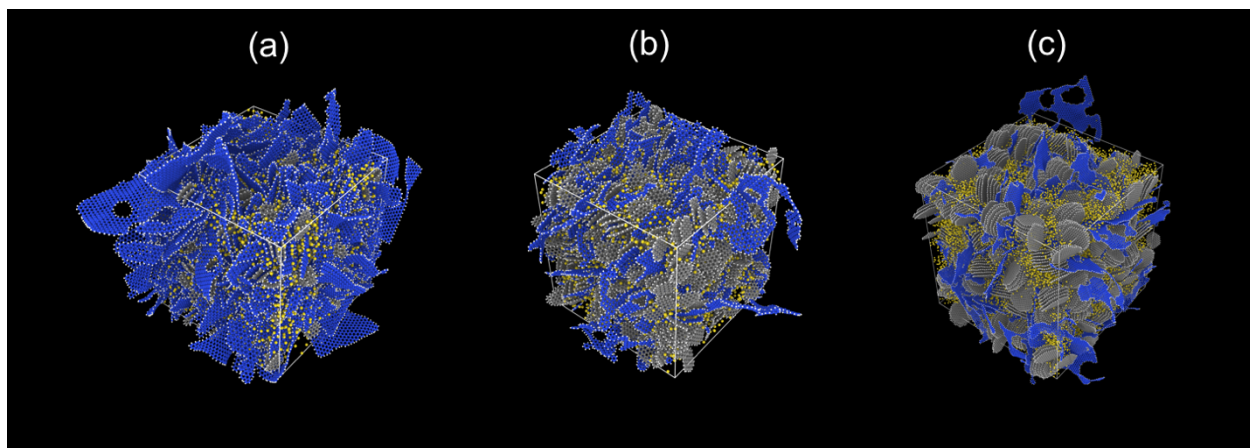


Figure 5.2. Snapshots of the three model systems that correspond to the three experimental systems after lithiation and equilibration: (a) $r = 5 \text{ \AA}$, $\rho = 1.94 \text{ g/cm}^3$, $\Phi_c = 0.9$, and $q = 126.1 \text{ mAh g}^{-1}$; (b) $r = 7 \text{ \AA}$, $\rho = 1.51 \text{ g/cm}^3$, $\Phi_c = 0.5$, and $q = 147.8 \text{ mAh g}^{-1}$; (c) $r = 17 \text{ \AA}$, $\rho = 1.38 \text{ g/cm}^3$, $\Phi_c = 0.1$, and $q = 349.8 \text{ mAh g}^{-1}$. Amorphous carbon is blue, crystalline carbon is gray, and Li-ions are yellow.

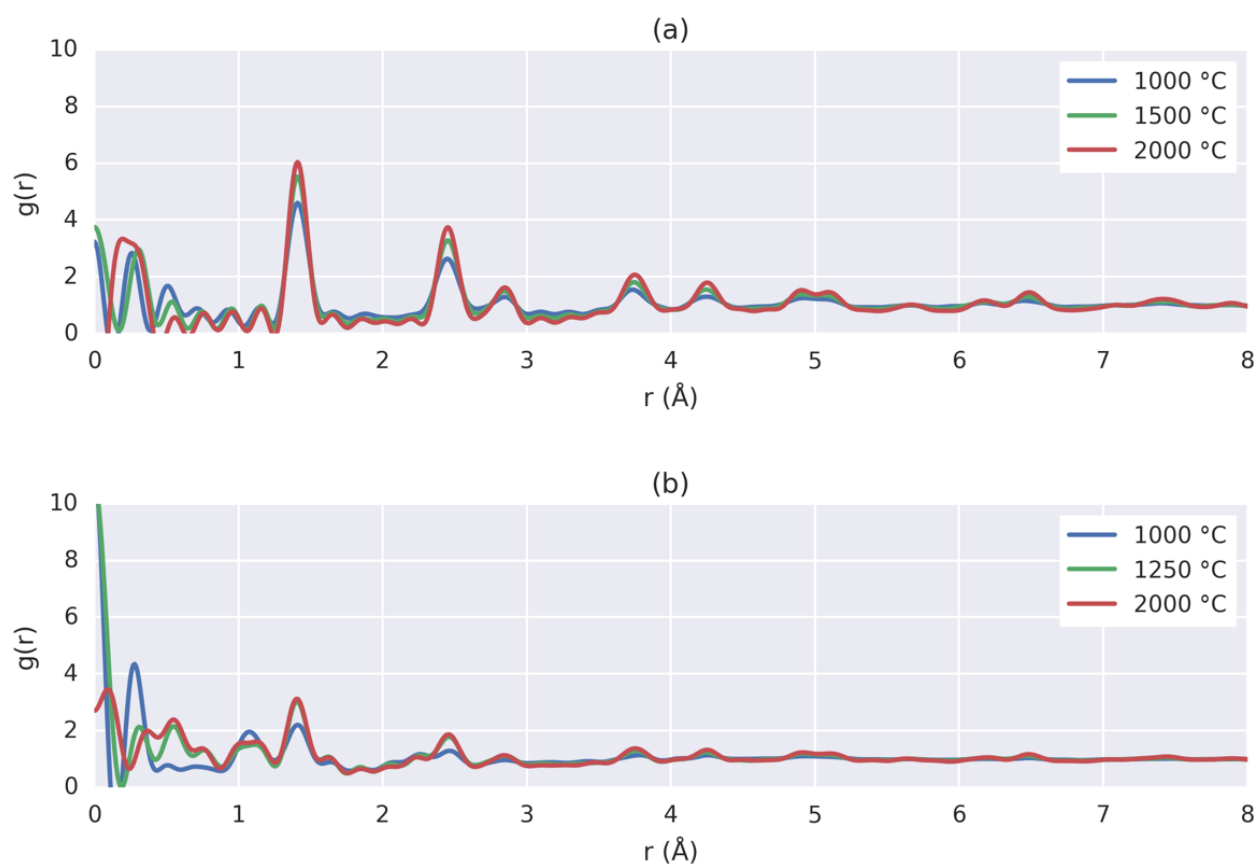


Figure 5.3. Experimentally obtained PDFs of (a) the uncharged systems and (b) the charged systems for three temperatures each.

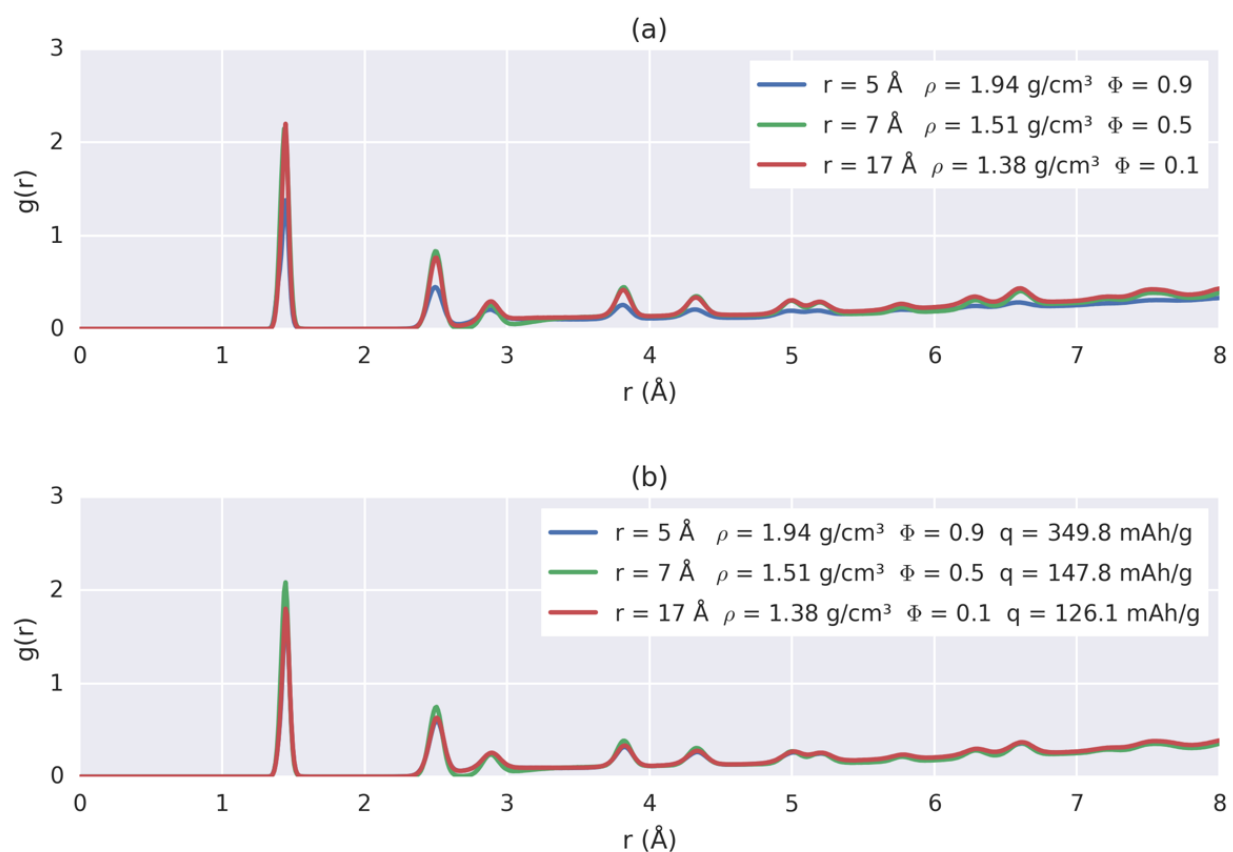


Figure 5.4. PDFs of the simulated models corresponding to the experimental systems in (a) the uncharged state and (b) the charged state.

Table 5.2. Description of component functions for pair distribution functions.

Component Function Name	Description
Total = A-A + A-C + C-C	Total pair distribution function
A-C	Only amorphous-crystalline (A-C) pairs of carbon atoms
A-A = Inter-A + intra-A	Only amorphous-amorphous (A-A) pairs of carbon atoms
A-A Intraplane	Pairs of amorphous atoms within the same amorphous fragment
A-A Interplane	Pairs of amorphous atoms between different amorphous fragments
C-C = Inter-C + Inter-P + Intra-P	Only crystalline-crystalline (C-C) pairs of carbon atoms
Intra-plane (Intra-P)	Pairs of carbon atoms within the same crystallite and the same plane
Inter-plane (Inter-P)	Pairs of carbon atoms within the same crystallite but different planes
Inter-crystallite (Inter-C)	Pairs of carbon atoms between different crystallites

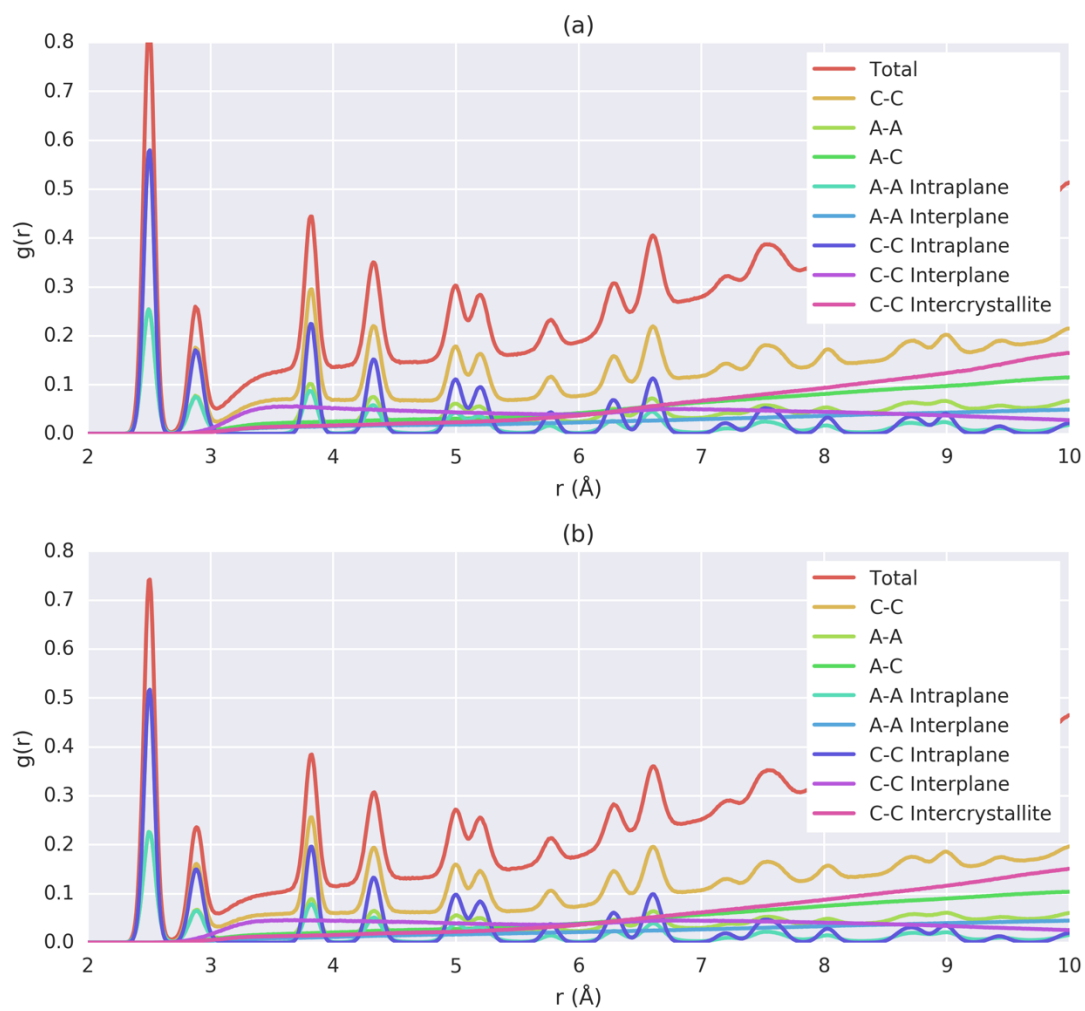


Figure 5.5. Carbon PDF decompositions of a representative uncharged system (a) and the charged system (b). The composite parameters are $r = 7 \text{ \AA}$, $\rho = 1.51 \text{ g/cm}^3$, $\Phi_c = 0.5$, and $q = 147.8 \text{ mAh g}^{-1}$.

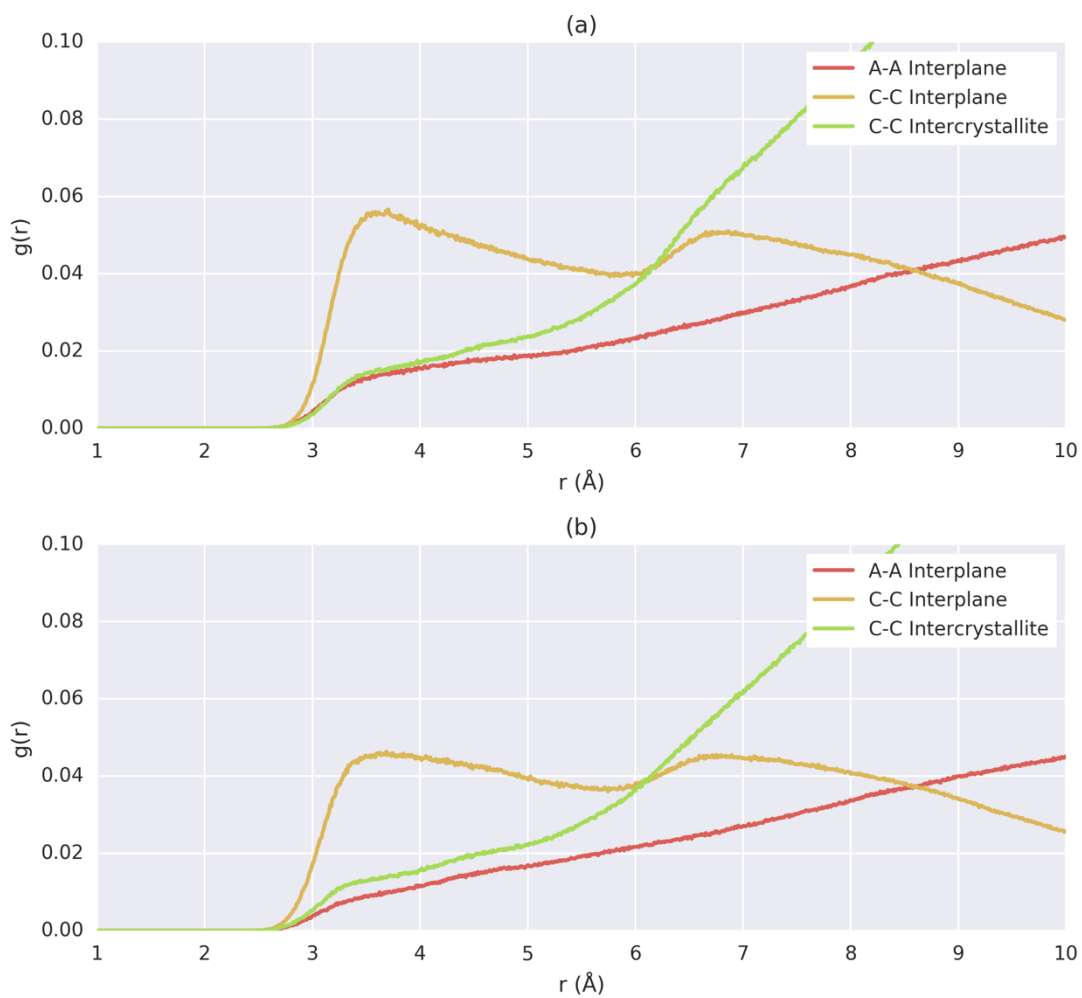


Figure 5.6. A close up view of the inter-carbon PDF component functions in **Figure 5.5** of (a) the uncharged composite and (b) the charged composite.

In order to better understand the effect of lithiation on the structure of the experimental systems, three-dimensional density distributions of the local atomic environment surrounding each Li-ion are created for different Li-ion energy levels and plotted for each experimental pyrolysis temperature. For a pyrolysis temperature of 1000 °C, **Figure 5.7** shows the localization of nearby lithium (green) and hydrogen (white) for strong (-20.86 to -14.04 kcal/mol), medium (-11.03 to -10.71 kcal/mol), and weak (-8.20 to 3.46 kcal/mol) Li-ion binding energies.

From the plot, it is clear that stronger binding energies correspond to more tightly localized hydrogen atoms. For weak binding energies (**Figure 5.7(c)**), the hydrogen loses its positional symmetry and tends to clump to one side. This allows the neighboring lithium ions (that were beginning to localize further away for medium binding energies) to return closer to the central Li-ion.

For a pyrolysis temperature of 1500 °C, **Figure 5.8** reveals that strong binding energies continue to correlate with precise hydrogen localization. The surrounding Li-ions have a very clear structural symmetry in **Figure 5.8(a)**, but they begin to lose this localization as the Li-ion binding energies become weaker.

For a pyrolysis temperature of 2000 °C, **Figure 5.9** shows that hydrogen is not as tightly localized as for the previous two systems. Because this system has a low total density and contains crystallites on the order of $r = 17 \text{ \AA}$, hydrogen is less available than in the systems with higher densities and smaller crystallites.

The neighboring crystalline carbon (colored blue and denoted "C") and amorphous carbon (colored yellow and denoted "A") distributions are shown for pyrolysis temperatures of 1000 °C, 1500 °C, and 2000 °C in **Figure 5.10**, **Figure 5.11**, and **Figure 5.12**, respectively. Similar to hydrogen, the surrounding carbon tends to localize most precisely for the strongest Li-ion binding energies.

5.3.1.2 Effect of density

The effect of density on Li-ion localization is presented in **Figure 5.13**. From these plots, it is clear that Li-ions are more tightly localized in the low density systems (corresponding to the height of the blue and red peaks in **Figure 5.13(a)** and (b)). The Li-H plot in **Figure 5.13(c)**, further corroborates this, as it is evident that peak height increases with decreasing composite density. This suggests that a lower density of atoms around the Li-ions permits them to fall into more highly localized energy wells.

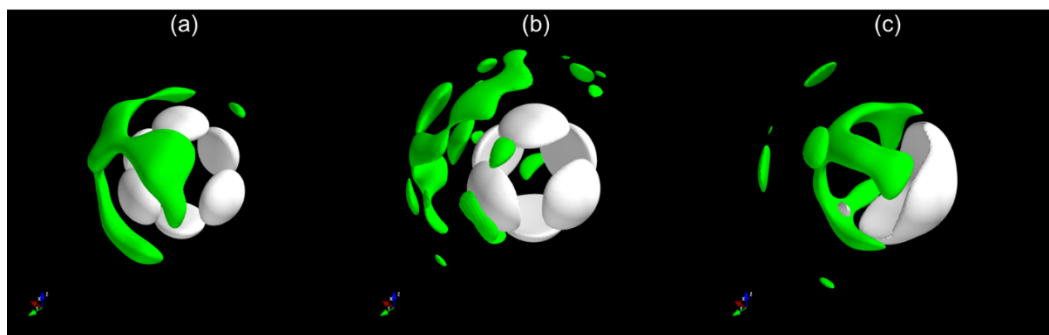


Figure 5.7. For the model of the 1000 °C experimental system, the 3D density distributions of Li (green) and H (white) for (a) strong Li-ion binding energies, (b) moderate Li-ion binding energies, and (c) weak Li-ion binding energies. Each distribution is centered around a Li ion, which is not shown.

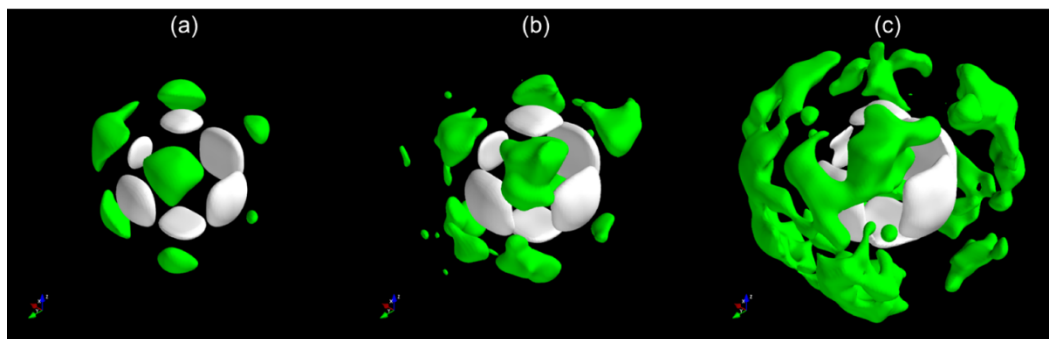


Figure 5.8. For the model of the 1500 °C experimental system, the 3D density distributions of Li (green) and H (white) for (a) strong Li-ion binding energies, (b) moderate Li-ion binding energies, and (c) weak Li-ion binding energies. Each distribution is centered around a Li ion, which is not shown.

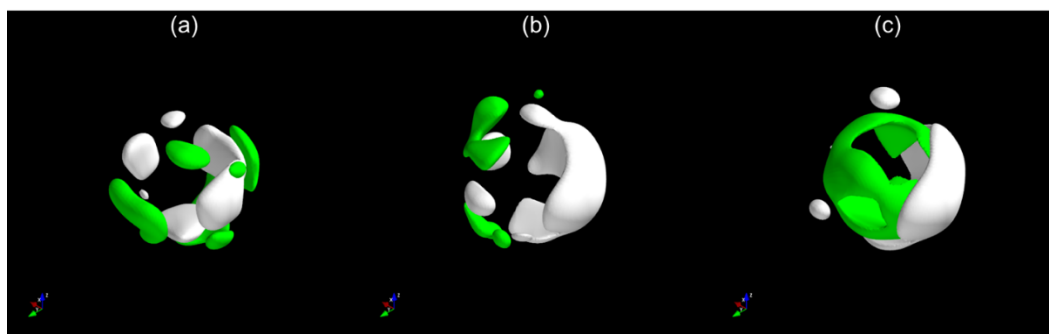


Figure 5.9. For the model of the 2000 °C experimental system, the 3D density distributions of Li (green) and H (white) for (a) strong Li-ion binding energies, (b) moderate Li-ion binding energies, and (c) weak Li-ion binding energies. Each distribution is centered around a Li ion, which is not shown.

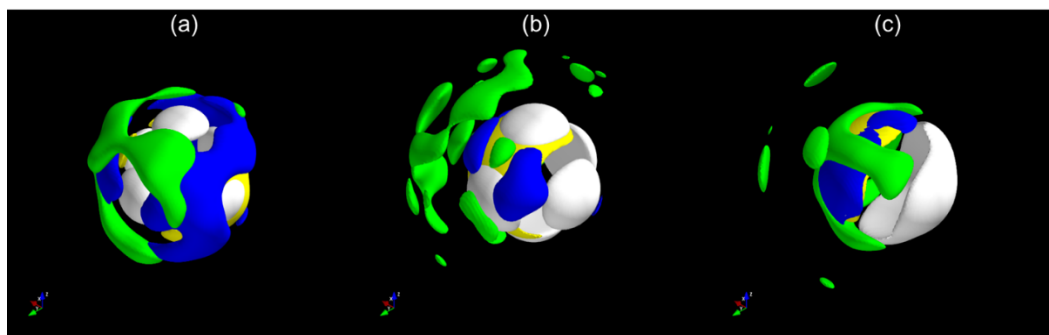


Figure 5.10. For the model of the 1000 °C experimental system, the 3D density distribution of Li (green), H (white), crystalline C (blue), and amorphous C (yellow) for (a) strong Li-ion binding energies, (b) moderate Li-ion binding energies, and (c) weak Li-ion binding energies.

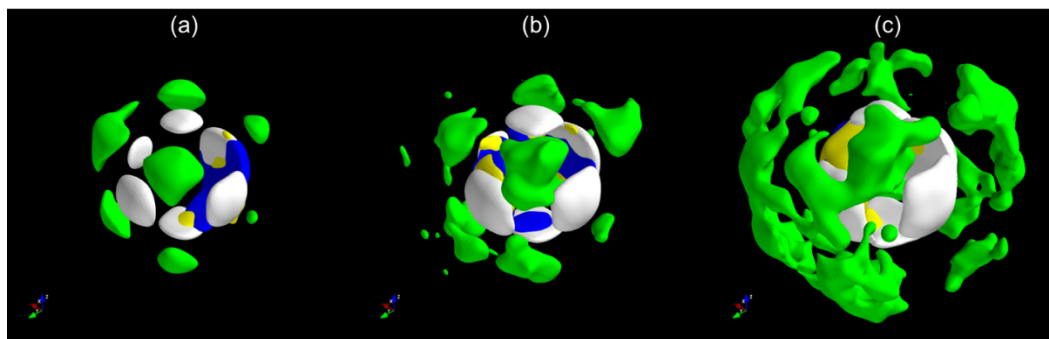


Figure 5.11. For the model of the 1500 °C experimental system, the 3D density distribution of Li (green), H (white), crystalline C (blue), and amorphous C (yellow) for (a) strong Li-ion binding energies, (b) moderate Li-ion binding energies, and (c) weak Li-ion binding energies.

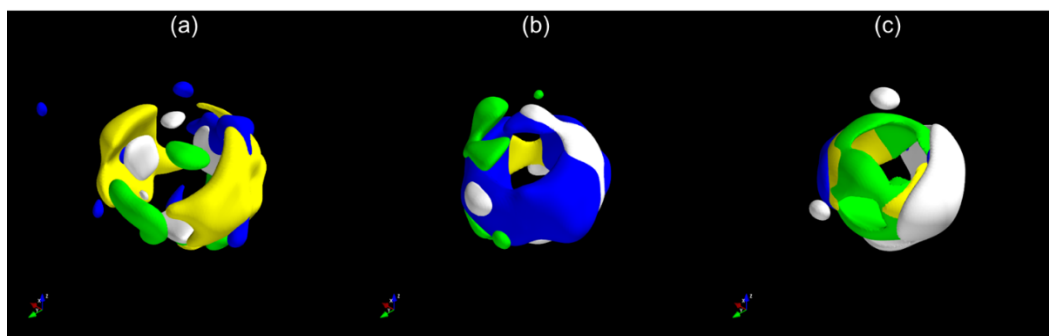


Figure 5.12. For the model of the 2000 °C experimental system, the 3D density distribution of Li (green), H (white), crystalline C (blue), and amorphous C (yellow) for (a) strong Li-ion binding energies, (b) moderate Li-ion binding energies, and (c) weak Li-ion binding energies.

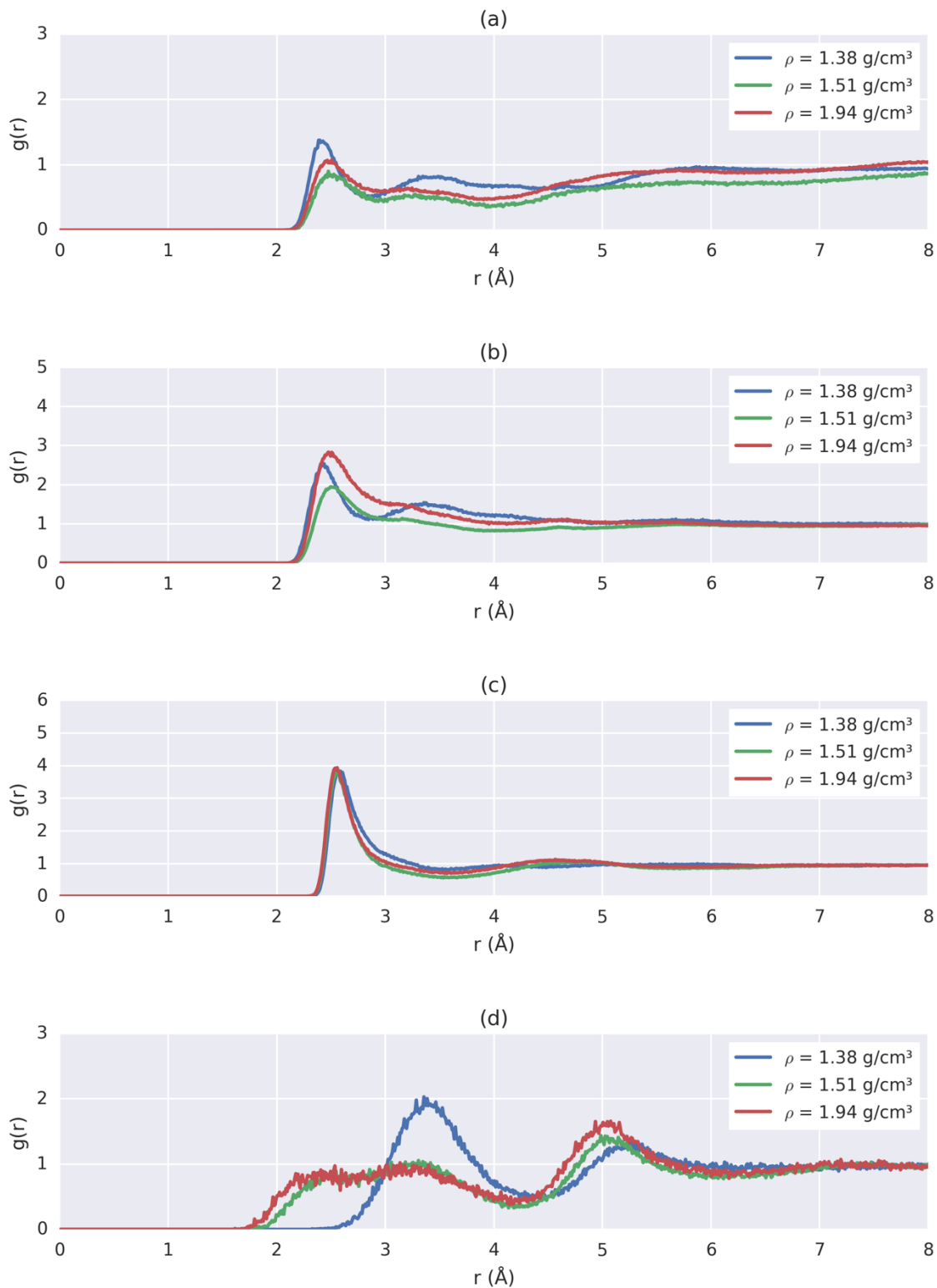


Figure 5.13. PDFs for (a) Li-C, (b) Li-A, (c) Li-H, and (d) Li-Li. Density varies across the three systems, while crystallite radius ($r = 7$ Å), crystalline volume fraction ($\Phi_c = 0.5$), and charge ($q = 147.8 \text{ mAh g}^{-1}$) are held constant.

The local atomic environments for systems with increasing composite density are shown in **Figure 5.14** and **Figure 5.15**. From **Figure 5.14**, it is evident that neighboring Li-ions tend to localize in a clean pattern about the surrounding hydrogen atoms for systems with low density. As the density increases, the Li-ions tend to distance themselves from the central Li-ion, and adopt a more asymmetrical configuration.

5.3.1.3 Effect of crystallite radius

The effect of crystallite radius on Li-ion localization is shown in **Figure 5.16** and **Figure 5.17**. From **Figure 5.16**, a change in crystallite radius from 5 Å to 7 Å seems to have little effect on Li-ion localization, indicating that these crystallite sizes are too similar. In **Figure 5.17**, the crystallite radius is changed from 7 Å to 17 Å, and a rather large difference between the PDFs of the two systems is evident in all but the Li-H PDF.

From **Figure 5.17(b)**, it is evident that a significantly larger crystallite radius brings the first Li-C and Li-A peaks closer and lowers their magnitude. From **Figure 5.17(d)**, the Li-Li peak changes significantly, with a low crystallite radius corresponding to a barely perceptible first peak, and a high crystallite radius corresponding to a well-defined peak at around 3.2 Å.

The local atomic environments shown in **Figure 5.18** and **Figure 5.19** show strong symmetry in the hydrogen localization. As crystallite radius becomes larger, it is clear that the nearest Li-ion neighbors move closer to the central ion.

5.3.1.4 Effect of crystalline volume fraction

The volume fraction of crystallite carbon in a material exhibits a more pronounced effect on ion localization than crystallite radius. **Figure 5.20(a)** indicates that highly amorphous carbon has more highly localized ions than crystalline material. For both the Li-C and Li-A pair distribution functions, a higher primary peak occurs when the volume fraction of crystalline material is low. The Li-H PDFs, however, show little difference, indicating that the Li-H bond is not significantly influenced by the type of carbon present in the system. The Li-Li peaks differ significantly, with the low crystalline volume fraction corresponding to a close but very broad peak. The medium volume fraction exhibits a sharper first peak, but one that is further away, and the high crystalline volume fraction exhibits a higher peak at the same location as the medium volume fraction.

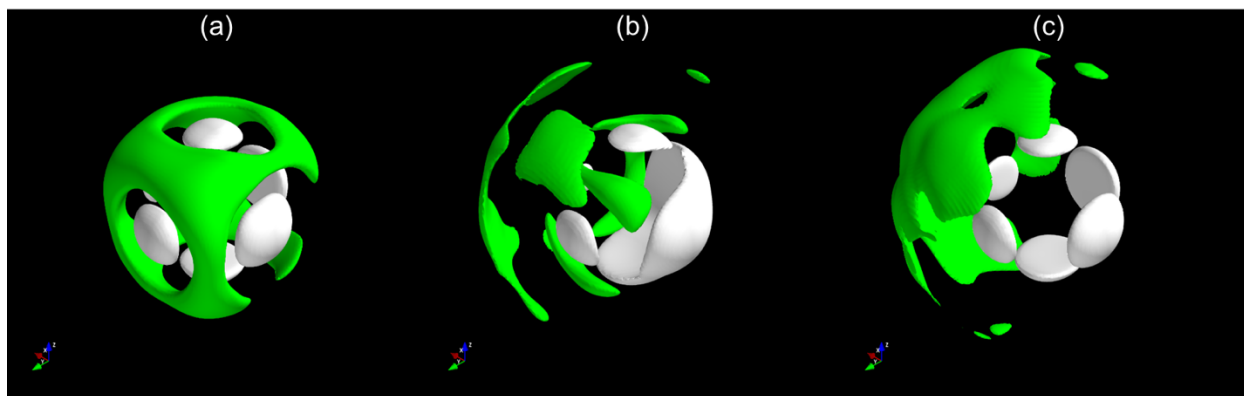


Figure 5.14. 3D density distributions for composite densities of (a) $\rho = 1.38 \text{ g/cm}^3$, (b) $\rho = 1.51 \text{ g/cm}^3$, and (c) $\rho = 1.94 \text{ g/cm}^3$. Crystallite radius ($r = 7 \text{ \AA}$), crystalline volume fraction ($\Phi_c = 0.5$), and charge ($q = 147.8 \text{ mAh g}^{-1}$) are held constant. Li ions are green and H atoms are white. Each distribution is centered around a Li ion, which is not shown.

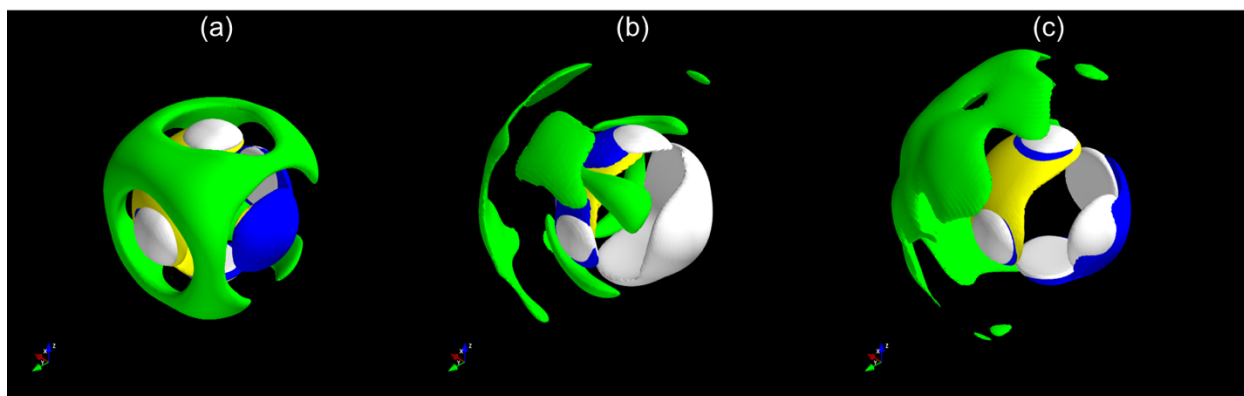


Figure 5.15. 3D density distributions for composite densities of (a) $\rho = 1.38 \text{ g/cm}^3$, (b) $\rho = 1.51 \text{ g/cm}^3$, and (c) $\rho = 1.94 \text{ g/cm}^3$. Crystallite radius ($r = 7 \text{ \AA}$), crystalline volume fraction ($\Phi_c = 0.5$), and charge ($q = 147.8 \text{ mAh g}^{-1}$) are held constant. Li ions are green, H atoms are white, C atoms are blue, and A atoms are yellow. Each distribution is centered around a Li ion, which is not shown.

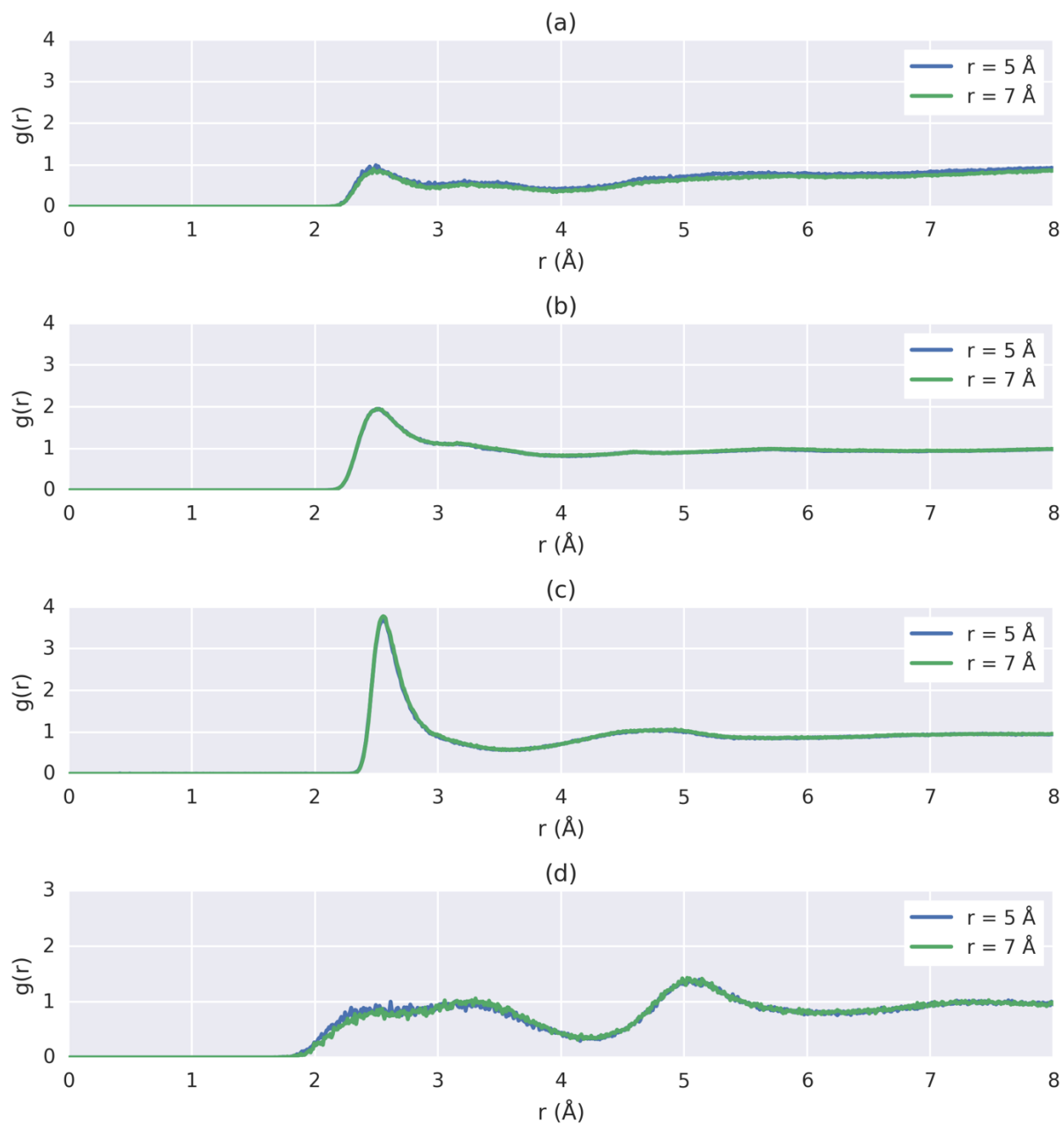


Figure 5.16. PDFs for (a) Li-C, (b) Li-A, (c) Li-H, and (d) Li-Li. Crystallite radius varies across the two systems, while density ($\rho = 1.94 \text{ g/cm}^3$), crystalline volume fraction ($\Phi_c = 0.5$), and charge ($q = 147.8 \text{ mAh g}^{-1}$) are held constant.

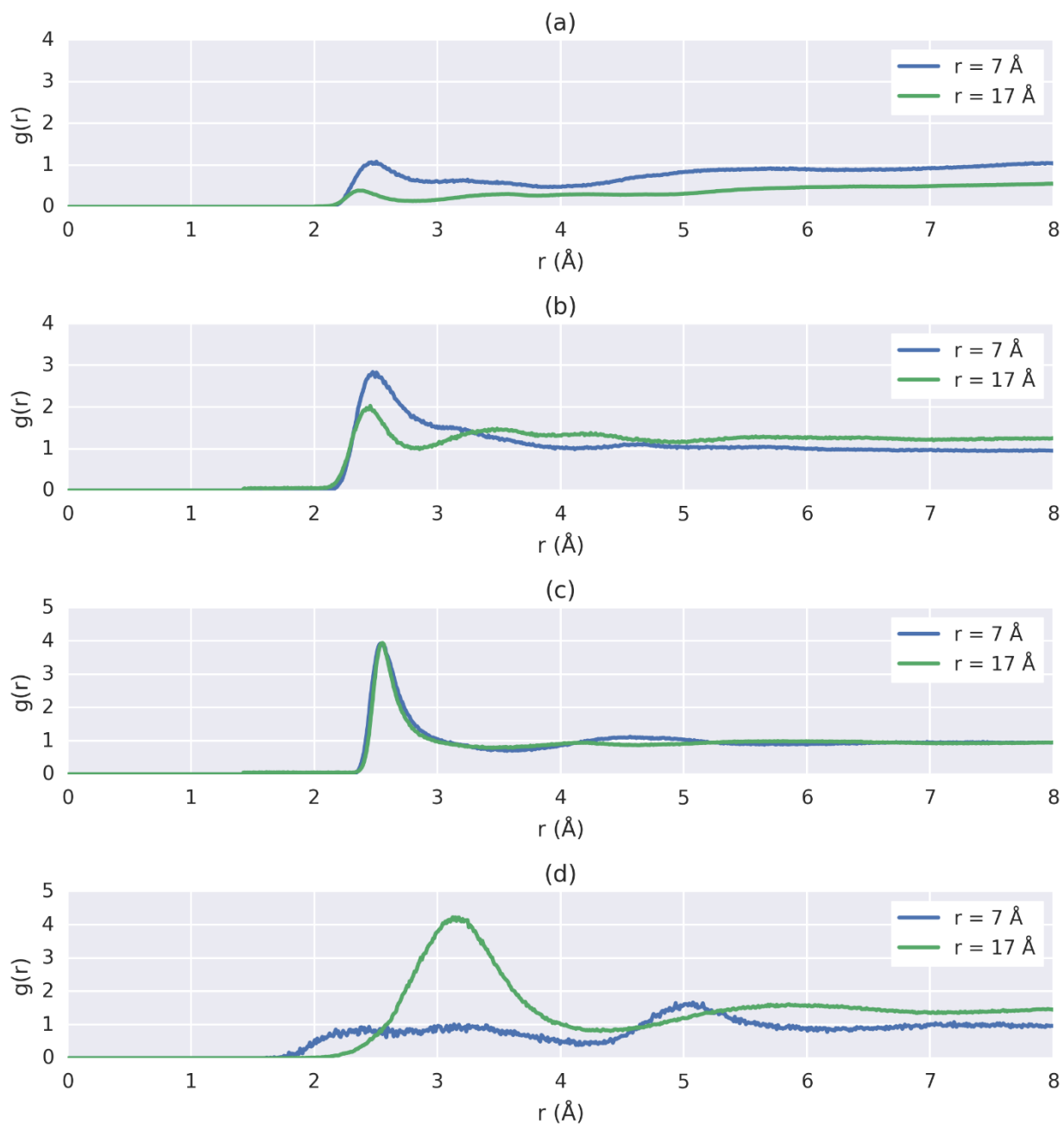


Figure 5.17. PDFs for (a) Li-C, (b) Li-A, (c) Li-H, and (d) Li-Li. Crystallite radius varies across the two systems, while density ($\rho = 1.38 \text{ g/cm}^3$), crystalline volume fraction ($\Phi_c = 0.5$), and charge ($q = 147.8 \text{ mAh g}^{-1}$) are held constant.

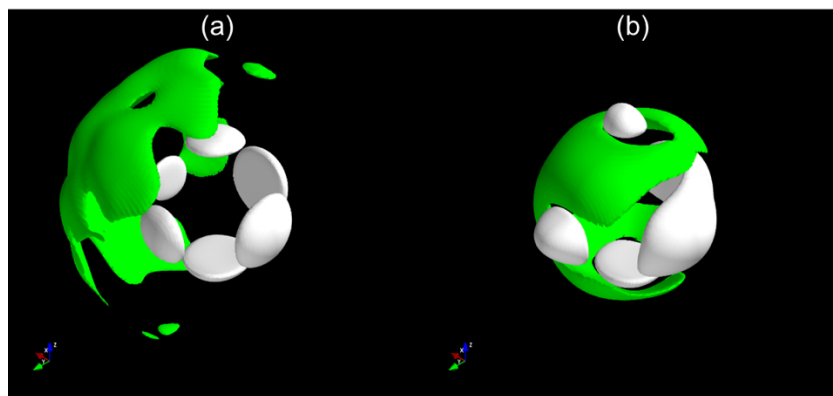


Figure 5.18. 3D density distributions for crystallite radii of (a) $r = 7 \text{ \AA}$ and (b) $r = 17 \text{ \AA}$. Composite density ($\rho = 1.38 \text{ g/cm}^3$), crystalline volume fraction ($\Phi_c = 0.5$), and charge ($q = 147.8 \text{ mAh g}^{-1}$) are held constant. Li ions are green and H atoms are white. Each distribution is centered around a Li ion, which is not shown.

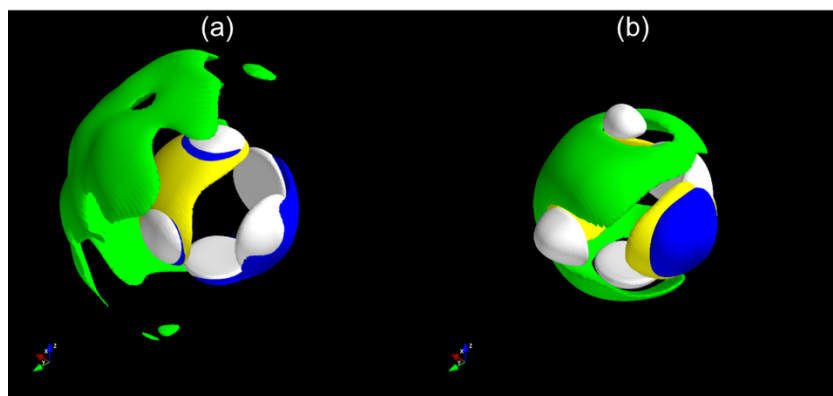


Figure 5.19. 3D density distributions for crystallite radii of (a) $r = 7 \text{ \AA}$ and (b) $r = 17 \text{ \AA}$. Composite density ($\rho = 1.38 \text{ g/cm}^3$), crystalline volume fraction ($\Phi_c = 0.5$), and charge ($q = 147.8 \text{ mAh g}^{-1}$) are held constant. Li ions are green, H atoms are white, C atoms are blue, and A atoms are yellow. Each distribution is centered around a Li ion, which is not shown.

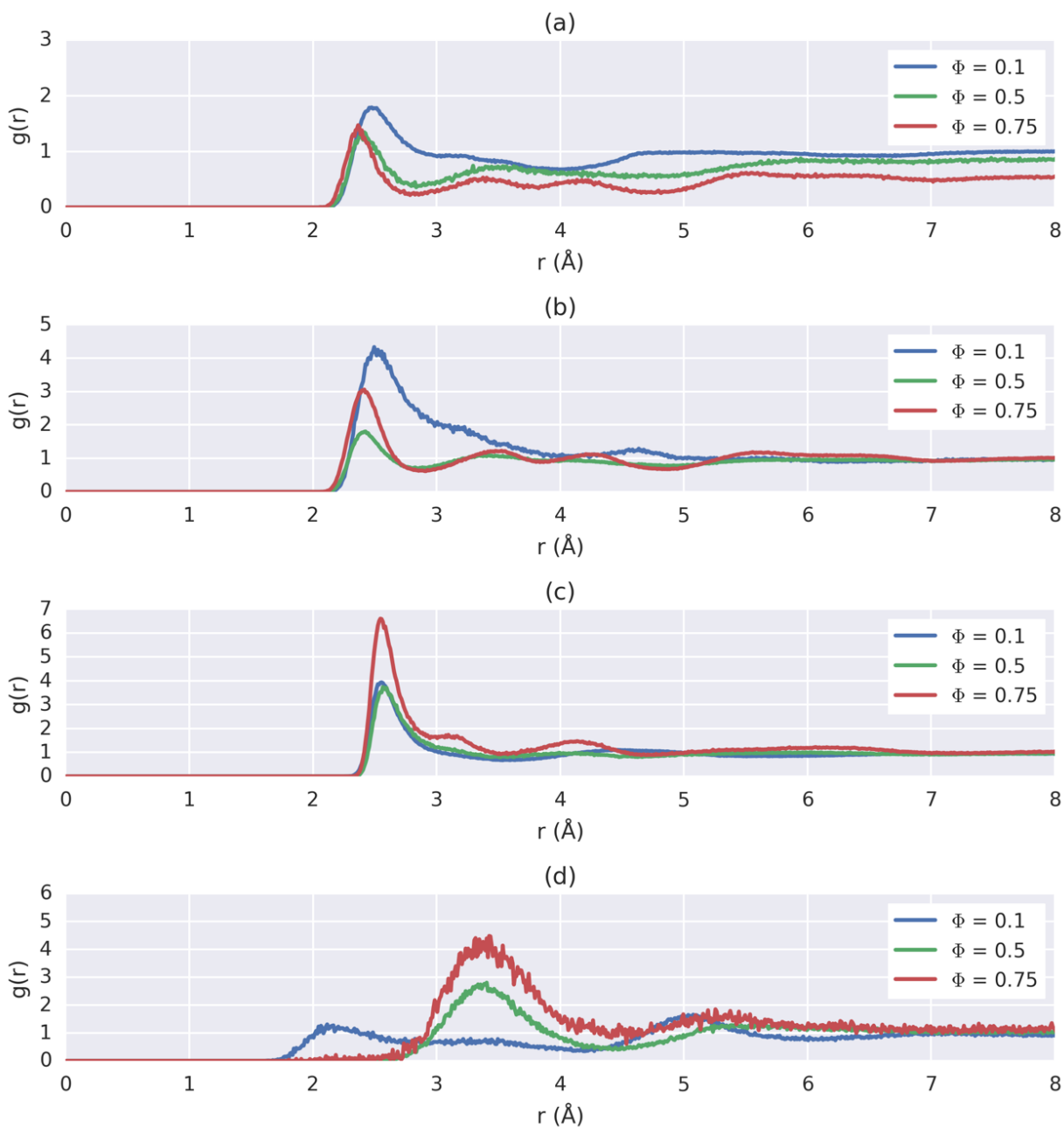


Figure 5.20. PDFs for (a) Li-C, (b) Li-A, (c) Li-H, and (d) Li-Li. Crystalline volume fraction varies across the three systems, while density ($\rho = 1.51 \text{ g/cm}^3$), crystallite radius ($r = 7 \text{ Å}$), and charge ($q = 147.8 \text{ mAh g}^{-1}$) are held constant.

From the local atomic environments in **Figure 5.21** and **Figure 5.22**, it is evident that a lower crystalline volume fraction leads to greater symmetry in the hydrogen localization and a further localization of Li from the central Li-ion. As volume fraction increases, the hydrogen tends to distribute to one side of the central Li-ion, and the neighboring Li-ions fill the void on the opposite side.

5.3.1.5 Effect of specific charge capacity

While specific charge capacity is an unknown function (and thus an effect) of pyrolysis temperature, it is still useful to observe the relationship between structure and storage capacity. **Figure 5.23** reveals that for higher charge capacities, the Li-C peaks become less sharp within the 2 – 4 Å region. This trend also occurs for the Li-A peaks, where for lower charge capacities there seem to “waves” that in the PDFs (blue and green curves), indicating that ion placement alternates between favorable and unfavorable locations as a function of distance from the surrounding carbon atoms. Interestingly, the Li-H PDF exhibits little change as a function of charge capacity. Previous research [74] suggests that the H/C ratio is directly correlated with ion storage capacity; however, Rothlisberger and Klein [75] posit that the environment surrounding the Li-H pair is more important. **Figure 5.23(c)** suggests that the H/C ratio is probably the more significant factor. **Figure 5.23(d)** highlights the fact that a higher specific charge capacity correlates with a closer, albeit broader, Li-Li first neighbor peak. It is also interesting to note that the *second* Li-Li peak occurs at roughly the same distance for all specific charge capacities.

The local atomic environments are shown in **Figure 5.24** and **Figure 5.25**. A high level of structural symmetry is evident from these atomic density distributions, and it is seen that a higher specific charge capacity correlates with a closer packing of the neighboring Li-ions to the central Li-ion, as would be expected. The hydrogen distribution is symmetric and very similar for all specific charge capacities; however, the hydrogen distribution for the lowest charge capacity is not as symmetric as the higher specific charge capacities.

5.3.2 ENERGETICS AND CHARGE

In addition to understanding the localization of Li-ions, understanding the ion energetics provides valuable insight into these systems as well. The binding energy controls the difficulty with which Li-ions move and diffuse about the system. A lower (more negative) value means that it is likely that an ion may become trapped in a particular location.

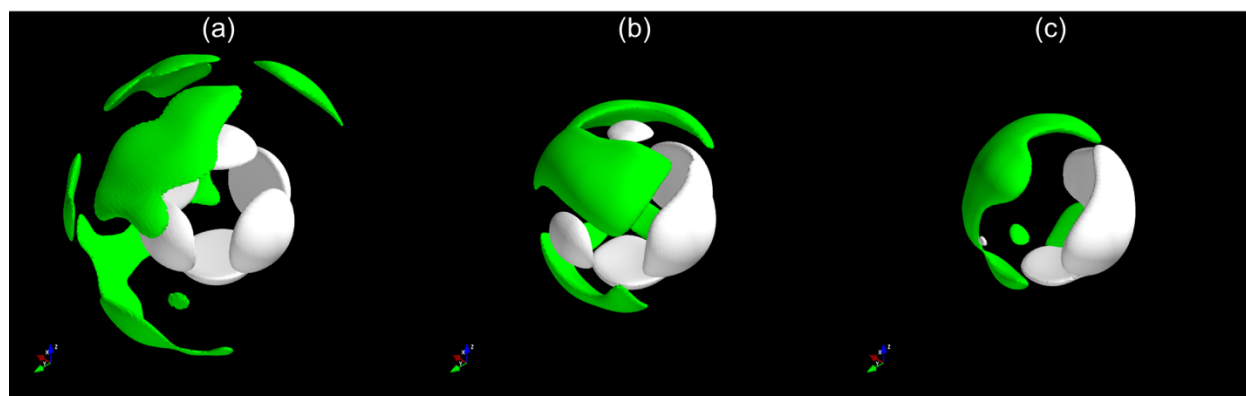


Figure 5.21. 3D density distributions for crystalline volume fractions of (a) $\Phi_c = 0.1$, (b) $\Phi_c = 0.5$, and (c) $\Phi_c = 0.75$. Crystallite radius ($r = 7 \text{ \AA}$), composite density ($\rho = 1.51 \text{ g/cm}^3$), and charge ($q = 147.8 \text{ mAh g}^{-1}$) are held constant. Li ions are green and H atoms are white. Each distribution is centered around a Li ion, which is not shown.

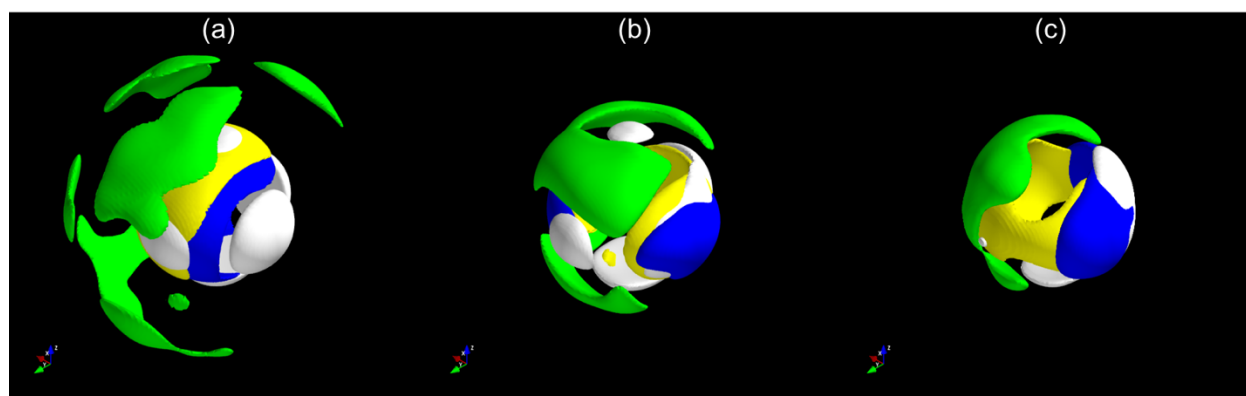


Figure 5.22. 3D density distributions for crystalline volume fractions of (a) $\Phi_c = 0.1$, (b) $\Phi_c = 0.5$, and (c) $\Phi_c = 0.75$. Crystallite radius ($r = 7 \text{ \AA}$), composite density ($\rho = 1.51 \text{ g/cm}^3$), and charge ($q = 147.8 \text{ mAh g}^{-1}$) are held constant. Li ions are green, H atoms are white, C atoms are blue, and A atoms are yellow. Each distribution is centered around a Li ion, which is not shown.

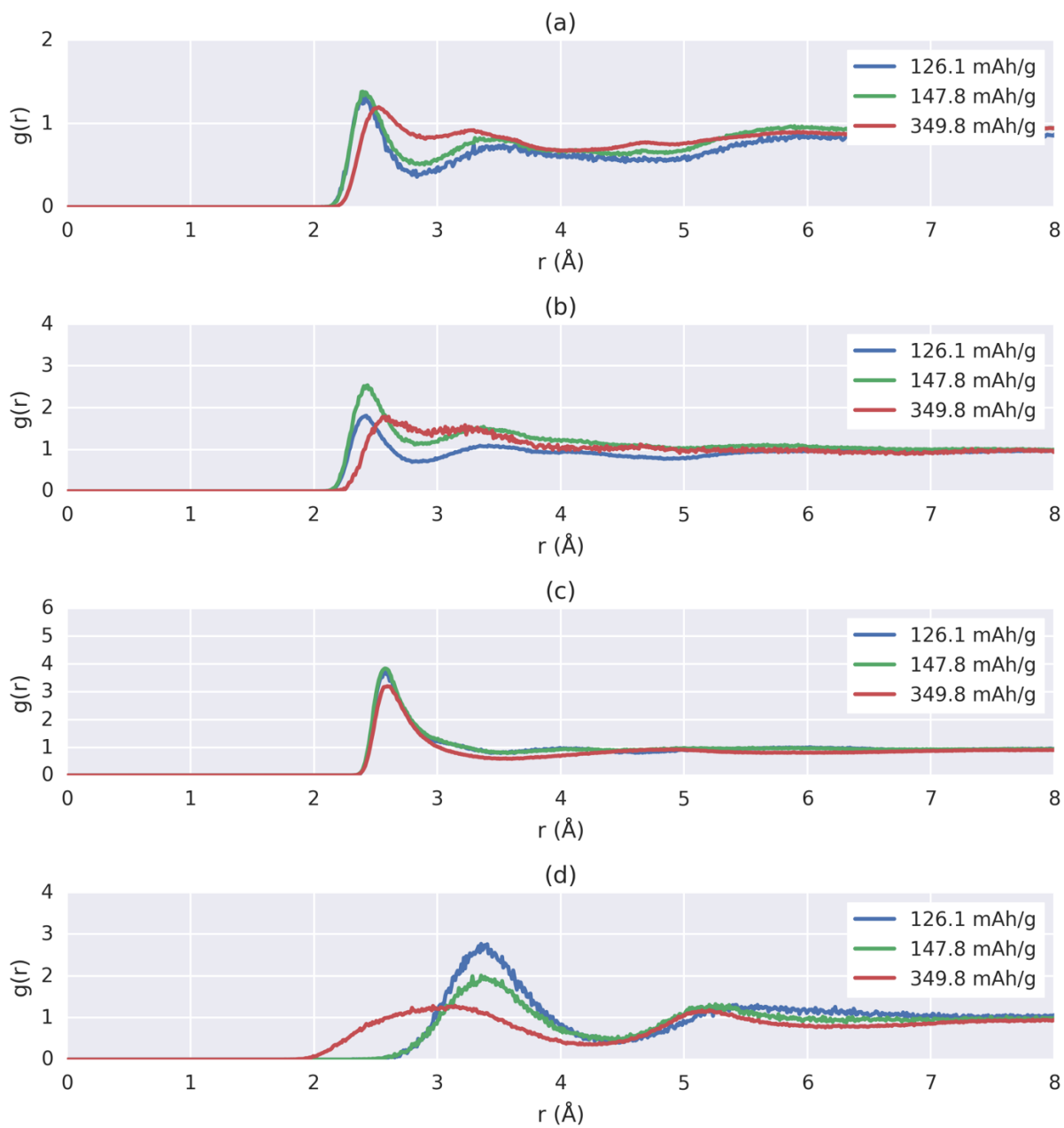


Figure 5.23. PDFs for (a) Li-C, (b) Li-A, (c) Li-H, and (d) Li-Li. Specific charge capacity varies across the three systems, while density ($\rho = 1.51 \text{ g/cm}^3$), crystalline volume fraction ($\Phi_c = 0.5$), and crystallite radius ($r = 7 \text{ Å}$) are held constant.

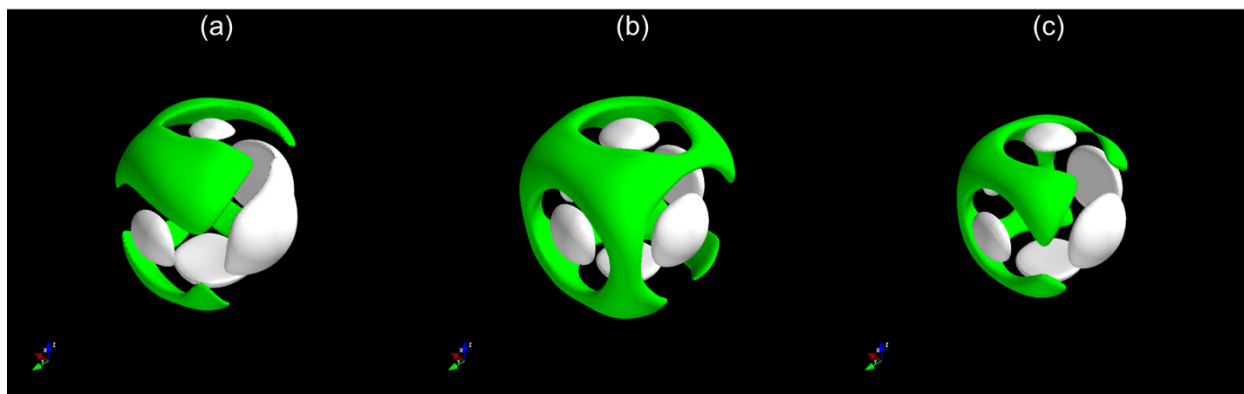


Figure 5.24. 3D density distributions for specific charge capacities of (a) $q = 126.1$ mAh/g, (b) $q = 147.8$ mAh/g, and (c) $q = 349.8$ mAh/g. Crystallite radius ($r = 7$ Å), composite density ($\rho = 1.51$ g/cm³), and crystalline volume fraction ($\Phi_c = 0.5$) are held constant. Li ions are green and H atoms are white. Each distribution is centered around a Li ion, which is not shown.

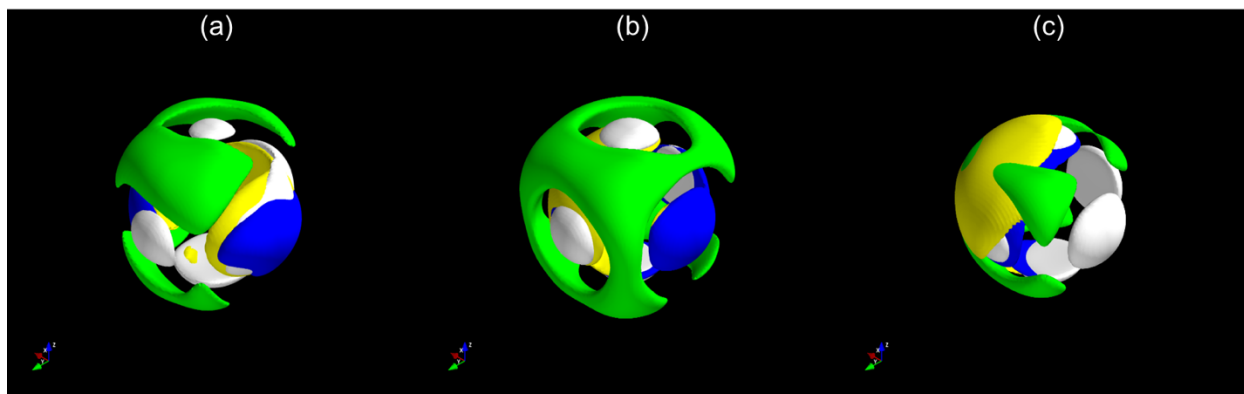


Figure 5.25. 3D density distributions for specific charge capacities of (a) $q = 126.1$ mAh/g, (b) $q = 147.8$ mAh/g, and (c) $q = 349.8$ mAh/g. Crystallite radius ($r = 7$ Å), composite density ($\rho = 1.51$ g/cm³), and crystalline volume fraction ($\Phi_c = 0.5$) are held constant. Li ions are green, H atoms are white, C atoms are blue, and A atoms are yellow. Each distribution is centered around a Li ion, which is not shown.

5.3.2.1 Effect of density

The effect of density on the energetics and charge is shown in **Figure 5.26**. With all other factors held constant, Li-ions become more strongly bound as the density of the systems decreases. This implies that the composite materials pyrolyzed at 2000 °C hold on to the ions more strongly, perhaps to the point of inducing irreversible capacity loss in the first charge cycle. **Figure 5.26(b)** shows that the more strongly bound Li-ions have a lower partial charge, indicating a bond that is less ionic in character.

5.3.2.2 Effect of crystallite radius

It is apparent from **Figure 5.27** that the effect of changing crystallite size from 5 to 7 Å appears to have little effect on either the binding energy or the charge of the Li-ions. However, **Figure 5.28** reveals that a larger change in crystallite size has a significant effect on both the binding energy and charge distributions. From **Figure 5.28**, it is clear that a larger crystallite radius corresponds to a significantly stronger binding energy. This suggests that as the crystallites become more graphitic in nature, the Li-ions in the composite tend to exclusively favor chemisorption. The charge distribution is significantly lower as well, indicating that the Li in the $r = 17$ Å system are closer to an atomic state than an ionic one.

5.3.2.3 Effect of crystalline volume fraction

Much in the way that this property affected Li-ion localization, it also strongly affects the energy and charge distributions of the ions. **Figure 5.29(a)** shows that a lower crystalline volume fraction begets more tightly bound Li-ions (well into the domain of chemisorption), whereas a high crystalline volume fraction seems to split the ion distribution across the chemi-/physisorption boundary. This is compelling evidence that the Li-ions reach a “sticking point”, where they either become trapped in deep energy wells or remain relatively loosely bound. **Figure 5.29** also exhibits a double peak in the charge distribution for the highly crystalline materials.

5.3.2.4 Effect of specific charge capacity

Again, it is prudent to examine the relationship between charge capacity and energy/charge distribution. From **Figure 5.30**, it is seen that the anodes with overall lower charge capacities actually store most of their ions in the chemisorbed region of the energy spectrum. It is likely that this binding is chemical in nature, and thus irreversible. The charge distribution exhibits a similar trend.

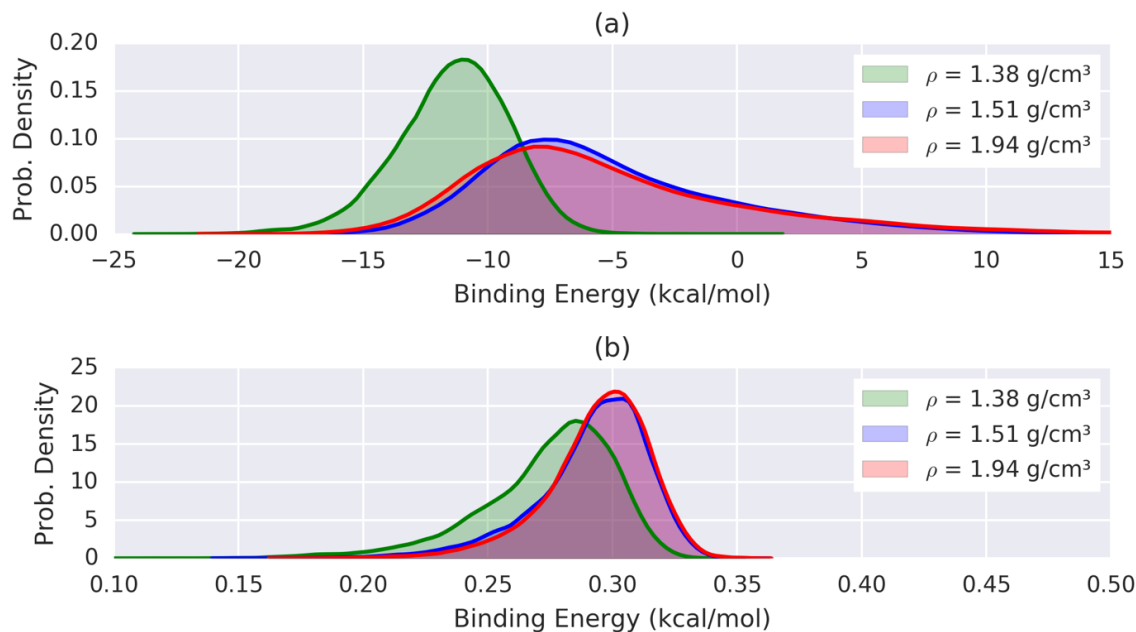


Figure 5.26. The energy distribution (a) and charge distribution (b) of three systems. Density varies across the systems, while crystallite radius ($r = 7 \text{ \AA}$), crystalline volume fraction ($\Phi_c = 0.5$), and charge ($q = 147.8 \text{ mAh g}^{-1}$) are held constant.

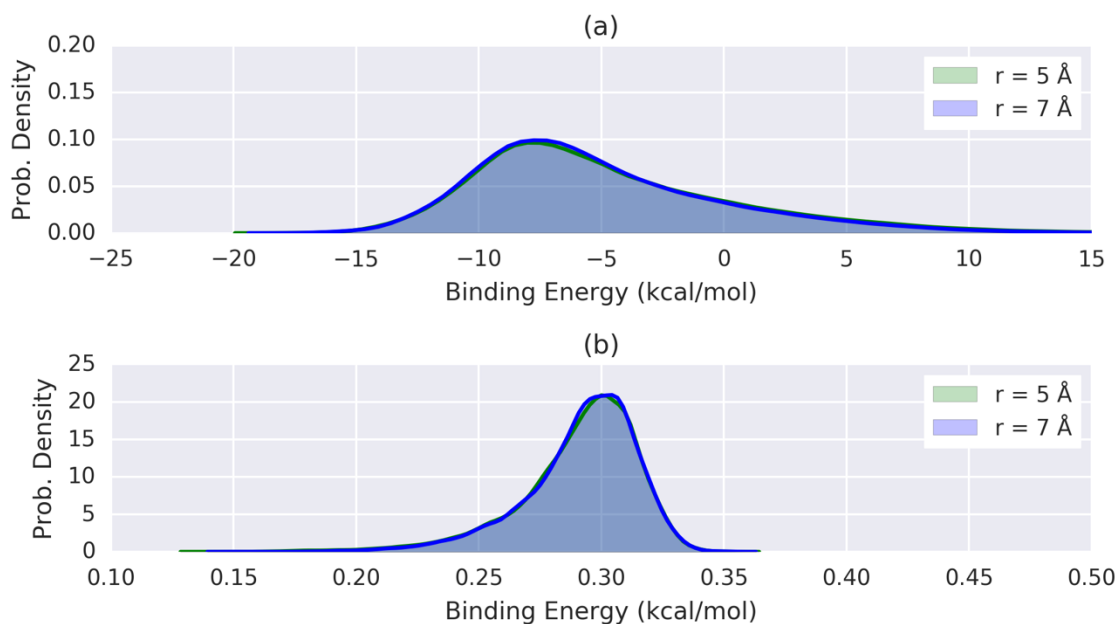


Figure 5.27. The energy distribution (a) and charge distribution (b) of two systems. Crystallite radius varies across the two systems, while density ($\rho = 1.94 \text{ g/cm}^3$), crystalline volume fraction ($\Phi_c = 0.5$), and charge ($q = 147.8 \text{ mAh g}^{-1}$) are held constant.

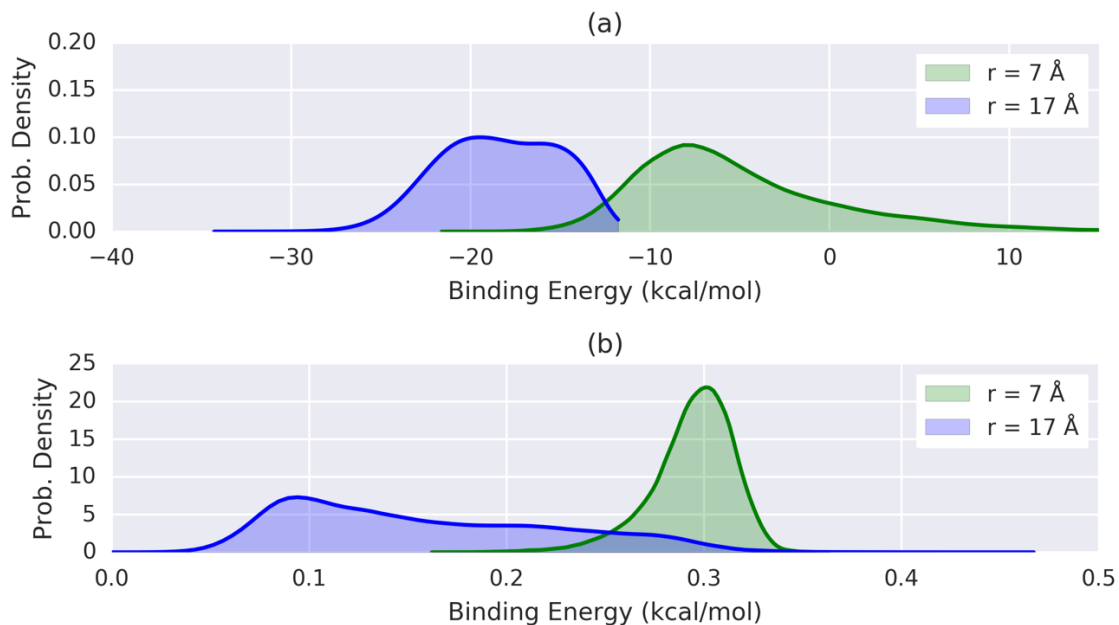


Figure 5.28. The energy distribution (a) and charge distribution (b) of two systems. Crystallite radius varies across the two systems, while density ($\rho = 1.38 \text{ g/cm}^3$), crystalline volume fraction ($\Phi_c = 0.5$), and charge ($q = 147.8 \text{ mAh g}^{-1}$) are held constant.

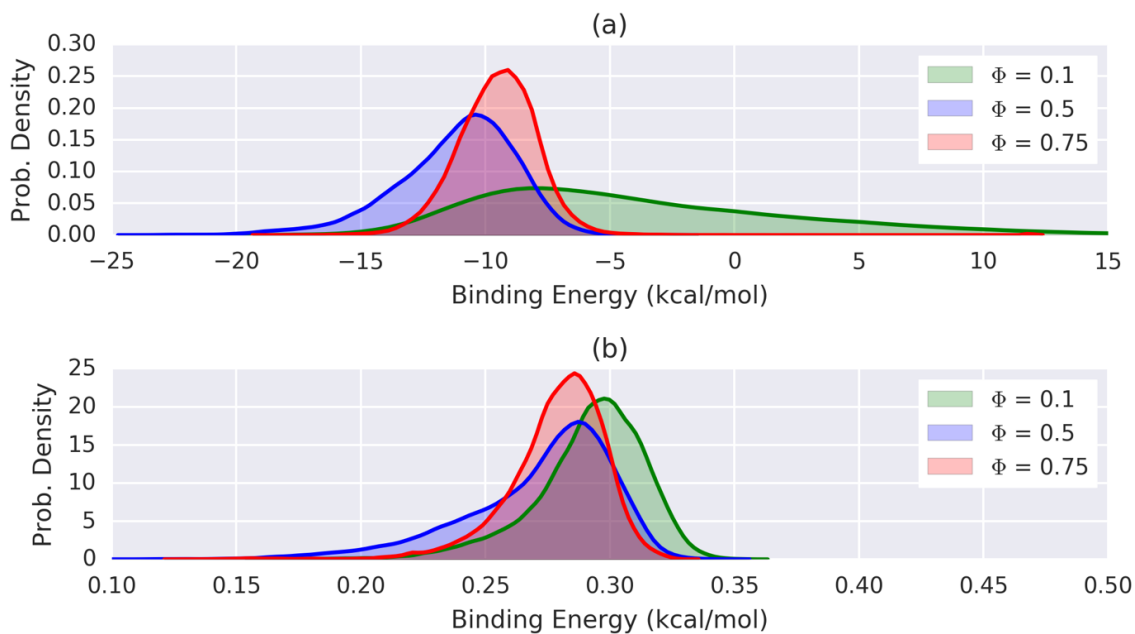


Figure 5.29. The energy distribution (a) and charge distribution (b) of three systems. Crystalline volume fraction varies across the three systems, while density ($\rho = 1.51 \text{ g/cm}^3$), crystallite radius ($r = 7 \text{ \AA}$), and charge ($q = 147.8 \text{ mAh g}^{-1}$) are held constant.

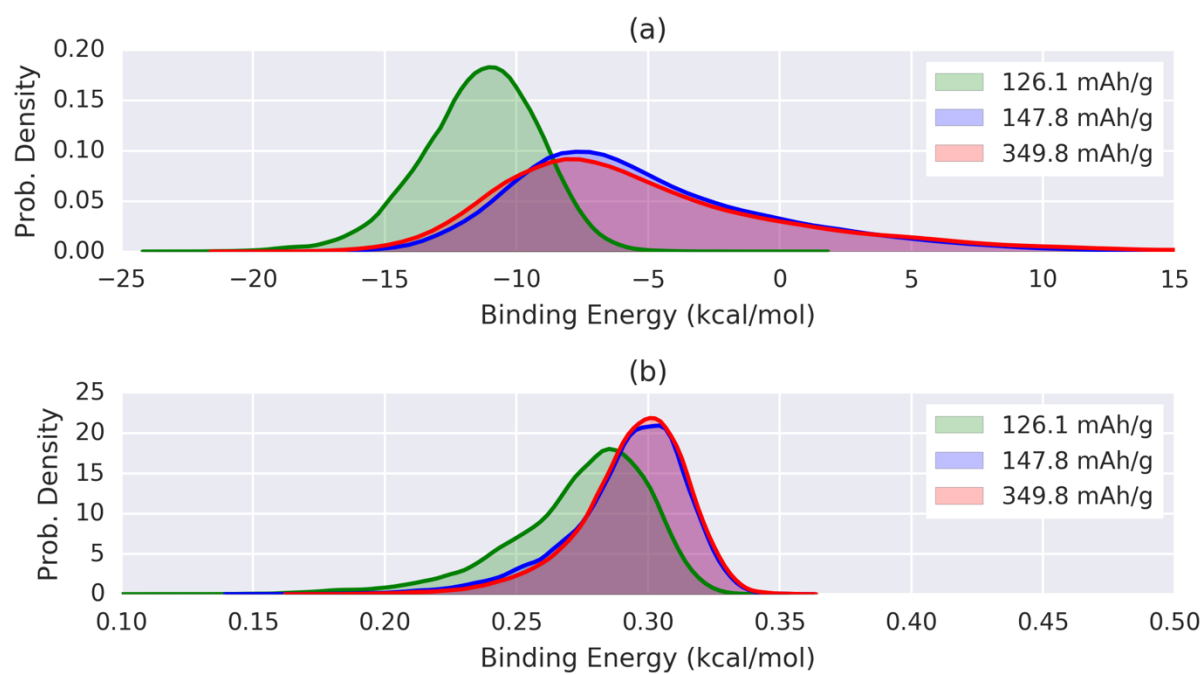


Figure 5.30. The energy distribution (a) and charge distribution (b) of three systems. Specific charge capacity varies across the three systems, while density ($\rho = 1.51 \text{ g/cm}^3$), crystalline volume fraction ($\Phi_c = 0.5$), and crystallite radius ($r = 7 \text{ \AA}$) are held constant.

5.4 CONCLUSIONS

From this work, a few important things become clear. Most significantly, the volume fraction of crystalline material appears to have a high impact on both the localization and energetics of Li-ions. This would suggest that, with regard to designing high performance carbon anodes, the *nature* of the structure of the carbon is a primary factor in the performance of the battery. On the other hand, the size of the crystalline domains had little effect on energetics or localization, suggesting that this property has little bearing on anode performance, at least until the crystalline domains become very large. The overall density of the composite material seems to have a small, but not insignificant effect. Lower densities lead to more tightly localized regions in space that the ions tend to gravitate toward, and the lower densities are also associated with lower binding energies that further contribute to the effect of keeping the Li-ions “in-place”. Lastly, the nature between storage capacity and localization is such that lower capacities lead to increased localization, and these locations tend to be more energetically favorable.

5.5 ACKNOWLEDGMENTS

N.M. was supported by a grant from the Oak Ridge Associated Universities High Performance Computing Program, by a grant from the Sustainable Energy Education and Research Center of the University of Tennessee, by a grant from the National Science Foundation (DGE-0801470), and by the STAIR program at the University of Tennessee. This research project used resources of the National Institute for Computational Sciences (NICS) supported by NSF under agreement number: OCI 07-11134.5. This research was also sponsored in part by the Laboratory Directed Research and Development Program of Oak Ridge National Laboratory, managed by UT-Battelle, LLC, for the U.S. Department of Energy. This research at Oak Ridge National Laboratory's Spallation Neutron Source was sponsored by the U.S. Department of Energy, Office of Basic Energy Sciences.

6 CONCLUSIONS

6.1 PER CHAPTER CONCLUSIONS

6.1.1 *ENTROPY-DRIVEN STRUCTURE AND DYNAMICS IN CARBON NANOCRYSTALLITES*

The thermodynamic, structural, and dynamic properties of carbon nanocrystallites have been studied through molecular dynamics simulations. The results show that the d-spacing increases with decreasing nanocrystallite size, in agreement with experimental observations from composite materials containing carbon nanocrystallites of different sizes. It is found that the increase in d-spacing is due to entropic effects. The binding energy between planes commensurately weakens with decreasing nanocrystallite size. The bonded potential energy (stretching, bending, and torsion) and in-plane nonbonded potential energy become less favorable with nanocrystallite size. The heat capacities of the nanocrystallites are in the range of 0.0057 to 0.0061 kcal/mole/K, significantly higher than bulk graphite. Three types of layer motion (breathing, sliding, and rocking angle) are observed for all three nanocrystallites at different temperatures. The Fourier transforms were conducted for all three types of motions and center of mass motion. The results show that there is a major frequency for sliding motion at 0.4 THz, which is close to the literature-reported value for graphite using the same potential. There are two major frequencies for breathing motion, with one at 1.45 THz and the other at 1.95 THz. These frequencies show little apparent variation with temperature over the range studied here. The study provides fundamental understanding of the physical properties of these layered carbon nanocrystallites. This work can aid in the understanding of Li-ion intercalation in composite anodes, which have shown strong dependence of ion capacity on crystallite size and a strong inverse relationship between electric charge capacity and crystalline d-spacing width.

6.1.2 *STRUCTURAL ANALYSIS OF LIGNIN-DERIVED CARBON COMPOSITE ANODES*

Novel anodes for use in lithium-ion batteries have been produced from the pyrolysis of low-cost lignin materials. These anodes consist of carbon composites with nanoscale structure in the form of nanocrystalline domains dispersed throughout an amorphous carbon matrix. The neutron spectra of these materials have been obtained, and the understanding of these spectra has been realized through the generation of a suite of simulated composite systems that replicate the measurable properties of the experimental systems.

The correct reproduction of the experimental neutron spectra from the simulated systems confirms the accuracy of the model and allows its use in relating unique characteristics of the pair distribution functions to structural properties of the system. In particular, a correspondence between a region of the

experimental pair distribution functions and the d-spacing within crystalline domains has been identified, potentially enabling the prediction of microstructural features in composite systems. This information provides insight useful in the design of advanced energy storage materials and manufacturing methods. Therefore, it is important to develop computational tools for analysis, potentially without reliance on computationally-intensive molecular dynamics simulations, that allow for an estimation of the decomposition based on structural factors such as composite density, crystallite size, and crystalline volume fraction. Extraction of d-spacing for example from the decomposition is then straight-forward.

Finally, as d-spacing has a direct influence on both the storage and rate of diffusion of lithium ions within the composite anodes, this capability will allow the understanding of lithium-ion diffusion within charged and uncharged lithiated composites from the pair distribution function alone.

6.1.3 INTERFACIAL LI-ION LOCALIZATION IN HIERARCHICAL CARBON ANODES

By inspecting the data in a variety of ways, a clear trend emerges for the nature of Li-ion localization in these hierarchical carbon materials. Most notably — and counter to the nature of ion storage in graphitic carbons — Li-ions do not intercalate between the layers of $r = 7 \text{ \AA}$ carbon nanocrystallites. The most energetically favorable positions for Li-ion storage are located near the hydrogen atoms located at the interface between the crystalline and amorphous domains of carbon. Because hydrogen content scales with interface size, Li-ion storage capacity (and thus charge capacity) is proportional to the surface area of the interfacial boundary.

The binding energies of lithium are highly variable, ranging from chemisorption to physisorption. This heterogeneity in binding energy can be partially captured in the PDFs, which show Li^+ aggregation for strongly bound Li^+ . For these composites, we have identified an archetypal structure of Li and H. Observed deviations from this structure reflect structural and thermal disorder.

6.1.4 LI-ION LOCALIZATION AND ENERGETICS AS A FUNCTION OF ANODE STRUCTURE

From this work, a few important things become clear. Most significantly, the volume fraction of crystalline material appears to have a high impact on both the localization and energetics of Li-ions. This would suggest that, with regard to designing high performance carbon anodes, the *nature* of the structure of the carbon is a primary factor in the performance of the battery. On the other hand, the size of the crystalline domains had little effect on energetics or localization, suggesting that this property has little bearing on anode performance, at least until the crystalline domains become very large. The overall density of the composite material seems to have a small, but not insignificant effect. Lower densities lead to more tightly

localized regions in space that the ions tend to gravitate toward, and the lower densities are also associated with lower binding energies that further contribute to the effect of keeping the Li-ions “in-place”. Lastly, the nature between storage capacity and localization is such that lower capacities lead to increased localization, and these locations tend to be more energetically favorable.

6.2 IMPACT AND SIGNIFICANCE

The impact of the results obtained from this work are possibly far reaching. While many exotic battery anodes have been developed that significantly outperform traditional carbon anodes, these designs have proven extremely difficult to scale up from the lab to an industrial environment. The demand for Li-ion batteries is currently at an all-time high as companies race to develop ever larger battery manufacturing plants. The electric car industry in particular requires batteries that outperform gasoline engines, and at a cost that is attainable for the average car owner. In this sense, these lignin-based anodes are optimally poised to be of immediate practical use in a society that is rapidly transitioning to all-electric vehicles.

By understanding the properties that correspond to high performing anodes, this work guides the development of low-cost batteries with high storage capacities. The connection between anode interfacial surface area and the temperature of lignin pyrolysis is highly general in its applicability, and a variety of manufacturing processes could be developed to maximize this surface area.

6.3 FUTURE WORK

In order to obtain accurate simulation results, this work required the use of a novel molecular dynamics potential (ReaxFF) that accounts for the chemical reactivity between Li-ions and the surrounding carbon and hydrogen atoms. While this potential delivers good accuracy, it also comes with a high computational cost. This means that, while the composite systems were able to be equilibrated, they were unable to be simulated for a long enough time to study the nature of Li-ion diffusion. With recent developments aimed at porting the ReaxFF code to run on GPUs, it would be particularly insightful to perform a microsecond simulation of these materials on a high performance computing system equipped with GPUs in order to better understand the mechanism behind Li-ions diffusion. This process is well understood for graphite anodes; however, the hierarchical nature of the lignin-derived anodes requires three orders of magnitude more atoms in order to study computational systems that closely match their physical analogues.

REFERENCES

1. Daniel, C., *Materials and processing for lithium-ion batteries*. Jom, 2008. **60**(9): p. 43-48.
2. Hossain, S., Y. Saleh, and R. Loutfy, *Carbon-carbon composite as anodes for lithium-ion battery systems*. Journal of Power Sources, 2001. **96**(1): p. 5-13.
3. Tenhaeff, W.E., et al., *Highly robust lithium ion battery anodes from lignin: An abundant, renewable, and low-cost material*. Advanced Functional Materials, 2014. **24**(1): p. 86-94.
4. Chatterjee, S., et al., *Synthesis and characterization of lignin-based carbon materials with tunable microstructure*. RSC Advances, 2014. **4**(9): p. 4743-4743.
5. Sharma, R.K., et al., *Characterization of chars from pyrolysis of lignin*. Fuel, 2004. **83**(11-12): p. 1469-1482.
6. Iijima, T., K. Suzuki, and Y. Matsuda, *Electrode characteristics of various carbon materials for lithium rechargeable batteries*. Synthetic Metals, 1995. **73**(1): p. 9-20.
7. Marsh, H. and J. Griffiths. *A high resolution electron microscopy study of graphitization of graphitizable carbon*. in *International symposium on carbon*. Carbon society of Japan. Annual meeting. 9. 1982.
8. Nimz, H., *Beech lignin—proposal of a constitutional scheme*. Angewandte Chemie International Edition in English, 1974. **13**(5): p. 313-321.
9. Balandin, A.A., et al., *Superior thermal conductivity of single-layer graphene*. Nano Letters, 2008. **8**(3): p. 902-907.
10. Geim, A.K. and K.S. Novoselov, *The rise of graphene*. Nature Mater., 2007. **6**(3): p. 183-191.
11. Yoo, E.J., et al., *Large reversible Li storage of graphene nanosheet families for use in rechargeable lithium ion batteries*. Nano Letters, 2008. **8**(8): p. 2277-2282.
12. Qi, W.H., et al., *Molecular dynamic simulation of the size- and shape-dependent lattice parameter of small Platinum nanoparticles*. Journal of Nanoparticle Research, 2009. **11**(3): p. 575-580.
13. Leontyev, I.N., et al., *Catalytic activity of Carbon-supported pt nanoelectrocatalysts. Why reducing the size of pt nanoparticles is not always beneficial*. Journal of Physical Chemistry C, 2011. **115**(13): p. 5429-5434.
14. Dmowski, W., et al., *Local Atomic Density of Microporous Carbons*. The Journal of Physical Chemistry C, 2012. **116**(4): p. 2946-2951.
15. Baker, F.S. *Low cost carbon fiber from renewable resources*. in *DOE Hydrogen Program and Vehicle Technologies Program Annual Merit Review and Peer Evaluation Meeting*. 2010. Washington, D.C.

16. Noel, M. and V. Suryanarayanan, *Role of carbon host lattices in Li-ion intercalation/de-intercalation processes*. Journal of Power Sources, 2002. **111**(2): p. 193-209.
17. Winter, M., et al., *Insertion Electrode Materials for Rechargeable Lithium Batteries*. Advanced Materials, 1998. **10**(10): p. 725-763.
18. Liu, Y., et al., *Mechanism of lithium insertion in hard carbons prepared by pyrolysis of epoxy resins*. Carbon, 1996. **34**(2): p. 193-200.
19. Rai, A., M. Warriar, and R. Schneider, *A hierarchical multi-scale method to simulate reactive-diffusive transport in porous media*. Computational Materials Science, 2009. **46**(2): p. 469-478.
20. Warriar, M., et al., *Multi-scale modeling of hydrogen isotope transport in porous graphite*. Journal of Nuclear Materials, 2005. **337**: p. 580-584.
21. Hasegawa, M., K. Nishidate, and H. Iyetomi, *Energetics of interlayer binding in graphite: The semiempirical approach revisited*. Physical Review B, 2007. **76**(11): p. 115424-115424.
22. Lebedeva, I.V., et al., *Interlayer interaction and relative vibrations of bilayer graphene*. Phys Chem Chem Phys, 2011. **13**(13): p. 5687-95.
23. Wang, Y., K. Scheerschmidt, and U. Gösele, *Theoretical investigations of bond properties in graphite and graphitic silicon*. Physical Review B, 2000. **61**(19): p. 12864-12870.
24. Dion, M., et al., *Van der Waals density functional for general geometries*. Physical Review Letters, 2004. **92**(24): p. 246401-1.
25. Tsai, J.-L. and J.-F. Tu, *Characterizing mechanical properties of graphite using molecular dynamics simulation*. Materials & Design, 2010. **31**(1): p. 194-199.
26. Shimizu, A. and H. Tachikawa, *Molecular dynamics simulation for sodium atom in and on the two layers of C150H 30 graphite plane*. Journal of Physics and Chemistry of Solids, 2003. **64**(12): p. 2397-2402.
27. Márquez, A., *Molecular dynamics studies of combined carbon/electrolyte/lithium-metal oxide interfaces*. Materials Chemistry and Physics, 2007. **104**(1): p. 199-209.
28. Marquez, A. and P.B. Balbuena, *Molecular Dynamics Study of Graphite/Eleetrolyte Interfaces*. Journal of the Electrochemical Society, 2001. **148**(6): p. 624-635.
29. Márquez, A.s., A. Vargas, and P.B. Balbuena, *Computational Studies of Lithium Intercalation in Model Graphite in the Presence of Tetrahydrofuran*. Journal of The Electrochemical Society, 1998. **145**(10): p. 3328-3328.
30. Aga, R.S., et al., *Theoretical investigation of the effect of graphite interlayer spacing on hydrogen absorption*. Physical Review B - Condensed Matter and Materials Physics, 2007. **76**(16).

31. Popov, A.M., et al., *Molecular dynamics simulation of the self-retracting motion of a graphene flake*. Physical Review B - Condensed Matter and Materials Physics, 2011. **536**(24): p. 245437-245437.
32. Popov, A.M., et al., *Barriers to motion and rotation of graphene layers based on measurements of shear mode frequencies*. Chemical Physics Letters, 2012. **536**: p. 82-86.
33. Dienwiebel, M., et al., *Superlubricity of graphite*. Physical Review Letters, 2004. **92**(12): p. 126101-126101.
34. Filippov, A.E., et al., *Torque and twist against superlubricity*. Physical Review Letters, 2008. **100**(4): p. 046102-046102.
35. Phillips, J.M. and N. Shrimpton, *Molecular-dynamics study of interlayer incommensurability in adsorbed multilayers*. Physical Review B, 1992. **45**(7): p. 3730-3734.
36. Hirano, M. and K. Shinjo, *Atomistic locking and friction*. Physical Review B, 1990. **41**(17): p. 11837-11851.
37. Sasaki, N., K. Kobayashi, and M. Tsukada, *Atomic-scale friction image of graphite in atomic-force microscopy*. Physical Review B, 1996. **54**(3): p. 2138-2149.
38. Verhoeven, G.S. and J.W.M. Frenken, *Superlubricity of Graphite part II : Model Calculations*. Physical Review B, 2003: p. 1-26.
39. Baker, D.A., N.C. Gallego, and F.S. Baker, *On the characterization and spinning of an organic-purified lignin toward the manufacture of low-cost carbon fiber*. Journal of Applied Polymer Science, 2012. **124**(1): p. 227-234.
40. McNutt, N.W., et al., *Carbon Nanocrystallites and Composite Materials*. 2014.
41. Langford, J.I. and A.J.C. Wilson, *Scherrer after sixty years: A survey and some new results in the determination of crystallite size*. Journal of Applied Crystallography, 1978. **11**(2): p. 102-113.
42. Plimpton, S., *Fast Parallel Algorithms for Short – Range Molecular Dynamics*. Journal of Computational Physics, 1995. **117**(June 1994): p. 1-19.
43. Jorgensen, W.L., D.S. Maxwell, and J. Tirado-Rives, *Development and testing of the OPLS all-atom force field on conformational energetics and properties of organic liquids*. Journal of the American Chemical Society, 1996. **118**(45): p. 11225-11236.
44. Fileti, E.E., G.M. Dalpian, and R. Rivelino, *Liquid separation by a graphene membrane Molecular dynamics simulations of transport and separation of carbon dioxide–alkane mixtures in carbon nanopores Liquid separation by a graphene membrane*. Journal of Applied Physics Appl. Phys. Lett. J. Appl. Phys. J. Chem. Phys, 2010. **108**(71): p. 113527-141906.

45. Stuart, S.J., A.B. Tutein, and J.A. Harrison, *A reactive potential for hydrocarbons with intermolecular interactions*. The Journal of Chemical Physics, 2000. **112**(2000): p. 6472-6486.
46. Tuckerman, M., et al., *Reversible multiple time scale molecular dynamics*. J. Chem. Phys., 1992. **97**(3): p. 1990-2001.
47. Zacharia, R., H. Ulbricht, and T. Hertel, *Interlayer cohesive energy of graphite from thermal desorption of polyaromatic hydrocarbons*. Physical Review B - Condensed Matter and Materials Physics, 2004. **69**(15).
48. Wang, Q., et al., *Molecular Dynamics Simulation of Poly(ethylene terephthalate) Oligomers*. J. Phys. Chem. B, 2009.
49. Savchenko, D.V. and S.G. Ionov, *Physical properties of carbon composite materials with low percolation threshold*. Journal of Physics and Chemistry of Solids, 2010. **71**(4): p. 548-550.
50. Meyer, J.C., et al., *On the roughness of single- and bi-layer graphene membranes*. Solid State Communications, 2007. **143**(1-2): p. 101-109.
51. Hawaldar, R., et al., *Large-area high-throughput synthesis of monolayer graphene sheet by Hot Filament Thermal Chemical Vapor Deposition*. Scientific Reports, 2012. **2**: p. 682-682.
52. Press, W.H., et al., *Numerical Recipes 3rd Edition: The Art of Scientific Computing*. 2007.
53. Nicklow, R., N. Wakabayashi, and H.G. Smith, *Lattice dynamics of pyrolytic graphite*. Physical Review B, 1972. **5**(12): p. 4951-4962.
54. Neufeind, J., et al., *The Nanoscale Ordered Materials Diffractometer NOMAD at the Spallation Neutron Source SNS*. Nuclear Instruments and Methods in Physics Research, Section B: Beam Interactions with Materials and Atoms, 2012. **287**: p. 68-75.
55. Neder, R.B. and T. Proffen, *Diffuse Scattering and Defect Structure Simulations: a Cookbook Using the Program DISCUS*. Vol. 1. 2008. 223-223.
56. Egami, T. and S.J.L. Billinge, *Underneath the Bragg peaks: structural analysis of complex materials*. 2012.
57. Hoover, W.G., *Canonical dynamics: Equilibrium phase-space distributions*. Physical Review A, 1985. **31**(3): p. 1695-1697.
58. McNutt, N.W., et al., *Entropy-driven structure and dynamics in carbon nanocrystallites*. Journal of Nanoparticle Research, 2014. **16**(4): p. 2365-2365.
59. Kobayashi N.a b c Saito, H.a.b.d.e., *Halftoning technique using genetic algorithms*. Systems and Computers in Japan, 1996. **27**(10): p. 89-97.

60. Song, C., P. Wang, and H.A. Makse, *A phase diagram for jammed matter*. Nature, 2008. **453**(7195): p. 629-632.
61. Willems, T.F., et al., *Algorithms and tools for high-throughput geometry-based analysis of crystalline porous materials*. Microporous and Mesoporous Materials, 2012. **149**(1): p. 134-141.
62. Shinoda, W., M. Shiga, and M. Mikami, *Rapid estimation of elastic constants by molecular dynamics simulation under constant stress*. Physical Review B - Condensed Matter and Materials Physics, 2004. **69**(13): p. 16-18.
63. Nosé, S., *A unified formulation of the constant temperature molecular dynamics methods*. Journal of Chemical Physics, 1984. **81**(1): p. 511-519.
64. Allen, M.P. and D.J. Tildesley, *Computer Simulation of Liquids*. Journal of Molecular Liquids, 1988. **38**(3): p. 267-267.
65. Chimowitz, E.H., *Introduction To Critical Phenomena in Fluids*. 2005.
66. Howell, R.C., T. Proffen, and S.D. Conradson, *Pair distribution function and structure factor of spherical particles*. Physical Review B - Condensed Matter and Materials Physics, 2006. **73**(9): p. 1-7.
67. Proffen, T., et al., *Structural analysis of complex materials using the atomic pair distribution function — a practical guide*. Zeitschrift für Kristallographie, 2003. **218**(2-2003): p. 132-143.
68. Qiu, X., et al., *Reciprocal-space instrumental effects on the real-space neutron atomic pair distribution function*. Journal of Applied Crystallography, 2004. **37**(1): p. 110-116.
69. Jeong, I.K., et al., *Measuring correlated atomic motion using X-ray diffraction*. Journal of Physical Chemistry A, 1999. **103**: p. 921-924.
70. Jeong, I.K.I., et al., *Lattice dynamics and correlated atomic motion from the atomic pair distribution function*. Physical Review B, 2003. **67**(10): p. 104301-104301.
71. Billinge, S.J.L., *Nanostructure studied using the atomic pair distribution function*. East, 2007. **26**(suppl_26): p. 17-26.
72. Dahn, J.R., et al., *Mechanisms for Lithium Insertion in Carbonaceous Materials*. Science, 1995. **270**(5236): p. 590-593.
73. Zheng, T., et al., *Lithium Insertion in High Capacity Carbonaceous Materials*. Journal of the Electrochemical Society, 1995. **142**(8): p. 2581-2590.
74. Papanek, P., M. Radosavljevic, and J.E. Fischer, *Lithium insertion in disordered carbon-hydrogen alloys: Intercalation vs covalent binding*. Chemistry of Materials, 1996. **8**(7): p. 1519-1526.

75. Rothlisberger, U. and M.L. Klein, *Ab Initio Molecular Dynamics Investigation of Singlet C₂H₂Li₂: Determination of the Ground State Structure and Observation of LiH Intermediates*. Journal of the American Chemical Society, 1995. **117**(10): p. 42-48.
76. McNutt, N.W., et al., *Structural analysis of lignin-derived carbon composite anodes*. Journal of Applied Crystallography, 2014. **47**(5): p. 1577-1584.
77. Van Duin, A.C.T., et al., *ReaxFF: A reactive force field for hydrocarbons*. Journal of Physical Chemistry A, 2001. **105**(41): p. 9396-9409.
78. van Duin, A.C.T., K. Chenoweth, and W.A. Goddard III, *ReaxFF force fields*. Potentials, 2008(July).
79. Aktulga, H.M., et al., *Reactive Molecular Dynamics: Numerical Methods and Algorithmic Techniques*. SIAM Journal on Scientific Computing, 2012. **34**(1): p. C1-C23.
80. Raju, M., et al., *Reactive force field study of Li/C systems for electrical energy storage*. Journal of Chemical Theory and Computation, 2015. **11**(5): p. 2156-2166.
81. Ganesh, P., et al., *Binding and Diffusion of Lithium in Graphite : Quantum Monte Carlo Benchmarks and Validation of van der Waals Density Functional Methods*. Journal of Chemical Theory and Computation, 2014. **10**: p. 5318-5323-5318-5323.
82. Yang, H., et al., *Self-weakening in lithiated graphene electrodes*. Chemical Physics Letters, 2013. **563**: p. 58-62.
83. Burns, G., *Solid State Physics*. 1985: Academic Press.
84. Gross, A., *Theoretical Surface Science*. 2014.
85. Venables, J., *Introduction to surface and thin film processes*. 2000.
86. Sacci, R.L., et al., *Operando NMR and XRD study of chemically synthesized LiC_x oxidation in a dry room environment*. Journal of Power Sources, 2015. **287**: p. 253-260.
87. McNutt, N.W., et al., *Interfacial Li-ion Localization in Hierarchical Carbon Anodes*.
88. Oyedele, A., et al., *Hierarchical Model for the Analysis of Scattering Data of Complex Materials*. JOM, 2016: p. 1-6.

VITA

Nicholas McNutt was born in Newton, NC, to parents Christopher and Susan McNutt. He has a younger sister, Emily. Growing up, he lived in Saint-Germain-en-Laye, France, and Hickory, NC, before moving to Woodstock, GA to attend Etowah High School. After graduation, he enrolled in the Georgia Institute of Technology and received a Bachelor's Degree in Chemical and Biomolecular Engineering in 2012. He then accepted a graduate research assistantship as part of the Ph.D. program in Chemical and Biomolecular Engineering at the University of Tennessee, Knoxville.